VILNIUS UNIVERSITY

CENTER FOR PHYSICAL SCIENCES AND TECHNOLOGY

AUDRIUS TEKORIUS

COMBINED METHODS AND INSTRUMENTATION FOR DOSIMETRIC MONITORING OF THE LARGE FLUENCE HADRON IRRADIATIONS

Doctoral dissertation

Physical sciences, Physics (02P)

Vilnius, 2015

Doctoral dissertation was prepared during period of 2011 – 2015 years at Vilnius University Faculty of Physics.

Supervisor – Dr. Sc. Eugenijus Gaubas (Vilnius University, Physical Sciences, Physics – 02P).

VILNIAUS UNIVERSITETAS

FIZINIŲ IR TECHNOLOGIJOS MOKSLŲ CENTRAS

AUDRIUS TEKORIUS

DIDELIŲ ĮTĖKIŲ HADRONŲ APŠVITŲ DOZIMETRIJOS KOMBINUOTI METODAI IR ĮRANGA

Daktaro disertacija

Fiziniai mokslai, fizika (02P)

Vilnius, 2015

Disertacija rengta 2011 – 2015 metais Vilniaus universiteto Fizikos fakultete.

Mokslinis vadovas – habil. dr. Eugenijus Gaubas (Vilniaus universitetas, fiziniai mokslai, fizika – 02P).

Contents

I. Introduction

Research problem. Dosimetry in the routine sense is the measurement of the absorbed dose in biological tissues and matter delivered by ionizing radiation or particle beams. Dosimetry is widely applied in the field of medical physics where it is inevitable for assessment of the radiation dose received by personnel and patients. Then radiation dose refers to the amount of energy deposited in matter and biological effects of radiation. The dose measurement unit is the gray (Gy) which defines the unit radiation energy deposited per mass unit (J/kg). This kind of dosimetry is used extensively for radiation protection. As various radiation types lead to different biological effects for the same deposited energy, a corrective radiation weighting factors are applied to convert the absorbed dose measured in the unit gray, into the equivalent dose measured in the unit sievert (Sv). The dose equivalent is the product of the absorbed dose of ionizing radiation and the dimensionless quality factor, defined as a function of linear energy transfer. The sievert represents the equivalent biological effect of a joule of radiation energy in a kilogram of human tissue related to a gray using quality factor.

The physical impact of different type irradiations is evaluated using measure of kinetic energy released per unit mass (Kerma), defined as the sum of the initial kinetic energies of all the charged particles liberated by uncharged ionizing radiation in a sample of matter, divided by the mass of the sample. The Kerma dose unit is the gray coinciding with the unit of absorbed dose. However, Kerma dose is different from absorbed dose, according to the energies involved, however, not accounted ionization energy. The Kerma dose is much higher than absorbed dose in the range of high energy irradiations, because some energy escapes from the absorbing volume in the form of X-rays or relativistic electrons. Atmospheric air Kerma is fundamental for the practical calibration of radiation protection instruments.

Another field of medical dosimetry is addressed to optimization of dose delivery in radiation therapy where three-dimensional dose distributions are often evaluated using different dosimetry techniques. Calculations are there performed to convert the physical quantity absorbed dose into equivalent and effective doses, the details of which depend on the radiation type and biological tissues. The assessment of optimized irradiations is performed by using anthropomorphic phantoms. These are 3D computational models of the human body which take into account a number of complex effects such as body self-shielding and internal scattering of radiation. The phantoms for experimental calibrations are commonly made of water or plastics (as PMMA). Dosimeters in radiotherapy within technology of linear particle accelerators for external beam therapy are routinely calibrated using ionization chambers, semiconductor sensors, and gel dosimetry means.

For accelerator environments, evaluation of the possible damage or reliable functionality of auxiliary instruments and electronic devices installed is necessary. Then the radiation activity or the strength of the radiation fields (fluence), attributed to the particle/radiation sources, is important. Exposure to a source of radiation determines a dose which is dependent on many factors, such as the activity, duration of exposure, energy of the radiation emitted, distance from the source and of shielding arrangements. Radiation fluence is the number of radiation particles crossing a unit area per unit time. For particle sources fluence is measured in units of cm^{-2} when the flux of particles is constant, while, Kerma is the ionizing effect of the radiation field, and the absorbed dose is the amount of radiation energy deposited per unit mass. The calibration of individual and of area dosimetry instruments is performed by measuring the collision “air Kerma” under conditions of secondary electron equilibrium. Then the appropriate operational quantity is derived applying a conversion coefficient that relates the air Kerma to the appropriate operational quantity. In high energy physics experiments, the essential problem is the operation duration of the expensive detector systems. There, fluence is the most appropriate parameter in design of event recording instruments. There the main damage of detectors appears due to accumulated dose through ionization processes and described by linear energy loss model and non-ionizing energy loss (NIEL) processes [1, 2]. The latter processes are responsible for creation of extended defects in matter and these are the prevailing reason of detector and electronic system damage. The NIEL interactions depend on energy of particles, especially hadrons, and are evaluated by interaction cross-section parameter. In fluence dosimetry it was found that for energies above 1 MeV the radiation induced damage is very similar for different type particles, namely electrons, pions, protons and neutrons. Therefore, the damage has been calibrated to equivalent fluence of 1 MeV neutrons, - 1 MeV neq in comparative dosimetry of high energy irradiation fluences. Thus, in particle accelerator infrastructure, the fluence dosimetry covers the range of fluences from 10^9 to 10^{17} cm^{-2} in 1 MeV neq. This field of dosimetry is therefore very different from that of common, bio-medicine and health safety dosimetry.

Traditional dosimeters are specifically designed as personal devices exploited in radiological protection of personnel to record and indicate the absorbed radiation. The electronic devices known as electronic personal dosimeters have come into general use based on semiconductor sensors which can give an indication of instantaneous dose rate or a total integrated dose. Also the stand-alone dosimeters are important for real-time monitoring of dose where a high dose rate is expected. Generally, operation of dosimeters is grounded on radiation energy loss in matter due to energy transfer to charged particles in the medium through various interactions ascribed to photoelectric effect, Compton scattering, pair production, or photodisintegration. Actually, registration of the secondary charged particles result in electrical, optical and thermal signals generated through atomic excitations and ionizations. The chemical, mainly organic material sensors such as alanine, sucrose or polymeric gel dosimeters are based on creation of free radicals or polymerization reactions under collected irradiation doses. There reading operations are performed by imaging implemented through the optical scanning, the spectroscopy of spin resonance attributed to nuclear or unpaired electrons, by ultrasound reading of radiation impacted materials. In traditional radiation protection and even in the radiotherapy dosimetry the rather narrow range of doses from the tens of mGy to 10-20 Gy (lethal for human body) is controlled. Even in this range of doses, the linearity of the response of dosimeters is an issue. To reach high sensitivity and measurement precision, the dose is ranged into small diapasons of dose evaluation with relevant instrumentation and test materials for calibration to overcome the response non-linearity problem, - for instance, the wide-spread alanine based Bruker dosimeters contain several inserts with EPR signal Mn^{+2} markers and alanine calibration dosimeters, every of which covers only a decade of dose value changes [3]. Therefore, search of the dosimeters with the bigger range of linearity, especially for high energy and large fluence irradiations, is a challenge in sensor physics. Therefore, in high energy radiation dosimetry, the new type radiation sensors are designed and tested, - as the nuclear transmutation based metal (Al) foils, sensors based on semiconductor diode leakage current control, chemical organic (alanine and gel dosimetry) sensors. The reviews of problems arising in design and implementation of such kind of sensors and dosimeters are reported in to date literature [4, 5, 6, 7]. However, rapid development of high brightness accelerator and spallator type radiation sources raises the new challenges in monitoring of the environment of big area instrumentation, where different kind of irradiations (as synchrotron radiation, radioactive elements appeared under nuclear transmutations) should be permanently controlled. Thus, specific requirements for the high energy irradiation dosimetry and sensors appear, - these sensors should be linear over a wide range of fluences, rather tolerant to radiations controlled, should be spatially and spectrally selective, the means of fluence reading on sensor should be fast, sensors should be cheap to produce. Additionally, the remote reading of sensor signals with relevant sensitivity, spatial and temporal selectivity is desirable in order to monitor the rate characteristics of fluence accumulation. The dual-type sensors would be also significant in reliable and remote registration of sensor signals, - as optical and electrical responses detected simultaneously. This would enable ones to control functionality of particle detector and electronic systems in harsh, close to particle beam areas.

This work was thereby addressed to solve several nowadays problems, mentioned above of dosimetry and fluence measuring under high energy hadron irradiations. There additional problems in radiation defect physics for recognition and characterization of dominant defects, in charge carrier recombination and transport physics for rapid and reliable interpretation of sensor signals, in surface modification physics and surface recombination evaluation methodology appear in design of dosimetry sensors and measurement technologies.

Objectives of research. The aim of this work was the development of measurement principles as well as combined methods and their implementation in fabrication of dosimeters for the monitoring of the particle beams. This goal is addressed to monitoring of moderate and large fluences within the environment of hadron accelerators and development of sensor instrumentation, including consideration of the problems of materials science and defect engineering. The purpose covers creation of the novel techniques for fluence measurements and remote signal recording, the creation of models capable to reveal peculiarities of the variations of optical and electrical signals related to technological and radiation defects in sensor materials, the development of measurement techniques for evaluation of surface passivation quality, evaluation of carrier transport, generation/recombination parameters important in design of wide-gap semiconductor sensors for detecting of large fluences.

The main tasks were concentrated on:

- optimization of the regimes and instrumentation of the contactless measurement of carrier lifetime in Si wafer sensors by microwave probed photoconductivity transient technique for the selective evaluation of fluence dependent changes of density of the extended and point radiation defects;
- characterization of the technological and radiation defects in polycrystalline layers of CdS and Cu_2S heterostructures in search of possibility to create the dual-purpose sensors by detecting optical and electrical signals;

- characterization of the technological and radiation defects in crystalline epi-layers of GaN grown by MOCVD technology and evaluation of the changes of carrier transport and recombination parameters as well as carrier pair production by hadrons in search of possibility to create means for simultaneous detection the optical and electrical signals in order to design fast and radiation tolerant sensors;
- development of contactless techniques for the *in situ* and remote control of the sensor electrical and optical signals, based on wide-bandgap semiconductor materials, during material modification by proton beams;
- design of the principles and combined techniques for spectroscopy of technological and radiation induced carrier traps;
- evaluation of surface passivation technologies and surface recombination parameters in Si edge-less strip detectors in order to optimize spatial resolution of strip detectors.

Relevance and scientific novelty. The detail analysis of the hadron fluence and anneal regimes dependent changes of the carrier recombination and trapping lifetimes in large resistivity and surface passivated Si wafers makes a principle for selective evaluation of the parameters of the hadron irradiation created point and extended defects. The direct measurements of carrier density relaxation rates and of photoconductivity changes performed by the microwave probed photoconductivity transient analysis enable to develop a wide fluence range of 10^{10} - 3×10^{16} cm^{-2} fluence meter with a linear response characteristic. The rapid monitoring of accelerator environment can then be implemented by placing the large resistivity and surface passivated Si wafer fragments, enveloped in plastic bags, over a large area of accelerator infrastructure and by consequent fast recording of the carrier lifetime using an instrument VUTEG-5-AIDA. The measurement technology and analysis of the carrier decay comprise a novelty in this work. Comprehensive and combined techniques of deep level spectroscopy, of barrier capacitance in Cu_2S heterostructures, of luminescence spectroscopy as well as microscopy and modelling of carrier transport characteristics in polycrystalline CdS materials is a reliable methodology for wide-bandgap material evaluation relative to its relevance for particle sensor fabrication. The newly evaluated parameters of pair production and of radiation defect introduction rate in Cu_2S heterostructures and CdS layers are important for estimation of the operational characteristics of the polycrystalline type, cheap sensors in detection of hadron irradiations. The combined technique and instrumentation for the contactless as well as remote and simultaneous recording of the temporal carrier decay parameters and of scintillation spectral characteristics in Cu_2S heterostructures and GaN epi-structures comprise a novelty in measurement technology. The parameters of pair production and of radiation defect introduction rate in MOCVD grown GaN epi-layers and their relation with structure disorder characteristics dependent on irradiation fluence are important for design of radiation tolerant sensors. The models for relation of the fluence dependent changes of the optical and electrical characteristics in disordered layers of MOCVD grown GaN epi-layers comprise a scientific novelty. The combined parallel and perpendicular (to the Si strip detector plane) scan of the excitation depth dependent amplitude of the photoconductivity is a novel method in evaluation of the parameters of surface recombination in the thin structures passivated using different technologies of thermal oxidation, atomic layer deposition and formation of silicon nitride layers.

Practical importance. The designed and fabricated dosimeter VUTEG-5-AIDA has been installed and approved for particle detector as well as facility monitoring in CERN. This instrument and measurement principles have been applied for material and radiation characterization using neutron spallator at Louvain la Neuve and Tandem accelerators at Institute of Physics (PTSC, Vilnius) and University of Helsinki facilities during implementation of the FP7 project AIDA.

The fast monitoring of harsh radiation environment, implemented by VUTEG-5-AIDA instrumentation, is promising for applications in nuclear power plants and in nuclear waste storage facilities. It would be a potential tool for evaluation of "electronic brain" functionality in rescue robots where radiation is unexpected and extremely intensive, such as in the aftermath of the Three Mile Island, Chernobyl or Fukushima radiological release incidents.

The combined techniques and instrumentations for the contactless as well as remote and simultaneous recording of the temporal carrier decay parameters and of scintillation spectral characteristics in Cu_2S heterostructures and GaN epi-structures can be approved for characterisation of new solid state materials promising in high energy radiation detection.

It has been proved that the developed methodology of evaluation of the parameters of pair production and of radiation defect introduction rate in disordered and crystalline structures and their relation with particle detector operational characteristics can be applied in search of the alternative and potential scintillators based on A_2B_6 and A_3B_5 compounds.

The developed techniques and instrumentation for the contactless as well as the remote measurements by using simultaneous recording of the electrical parameters and of scintillation characteristics can be employed in design and testing of the double signalling sensors and their systems.

The combined parallel and perpendicular scan technique using the measurement regimes by varying the excitation depth at several discrete light wavelengths has been approved for evaluation of the parameters of surface recombination in the thin structures passivated by different means in development of edgeless strip detector technology of enhanced spatial resolution for the future S/HL-LHC experiments at CERN.

Statements in defence. The main statements in defence of this thesis are as follows:

1. The proposed methodology of the experimental measurements and modelling, addressed to evaluation of carrier recombination and transport parameters within spatially inhomogeneous structures using combined analysis of the temporal and spectral changes of electrical and optical signals ascribed

to the same test excitation impact, enable inspection of the disorder and of the radiation induced changes of material parameters in micro-crystallites containing structures of wide bandgap semiconductors. The proposed methodology is implemented by simultaneous measurements of carrier non-radiative decay, performed by microwave probed photoconductivity transient, and radiative dissipation of excess carriers, controlled by transient luminescence spectroscopy, which are carried out to simultaneously collect the electrical and optical signals from the same excited local area.

2. The designed technique based on control of the carrier recombination and trapping components in heavily irradiated and thermally treated high purity, surface passivated Si wafer fragments enables the radiation and defect type selective fluence dosimetry in wide fluence range from 10^{11} to 10^{16} cm^{-2}, keeping the linearity of calibration characteristic. The combined parallel and perpendicular scan technique using the measurement regimes by varying the excitation depth at several discrete light wavelengths should be applied for the reliable evaluation of the parameters of surface recombination in thin structures passivated by different means in edgeless detector technology of enhanced spatial resolution.
3. The designed and fabricated instrument VUTEG-5-AIDA and methodology of plastic bag enveloped fluence accumulating Si sensors enable the wide area monitoring of harsh radiation environment and particle accelerating as well as spallating instrumentation, with option of profiling of the particle beam contours and irradiation distributions.
4. The developed techniques and instrumentation for the contactless and remote measurements by simultaneous recording of the changes of the electrical and of scintillation characteristics is a tool for extraction of carrier pair production and radiation defect introduction rate parameters in different materials impacted by various radiation types.

Author’s contribution. Over this study author performed measurements on capacitance-voltage characteristics, part of DLTS, BELIV and luminescence spectroscopy and participated in the in situ (during proton irradiations) measurements of microwave probed photoconductivity transients and scintillation spectra in various materials. Author developed the algorithms and software for the control of carrier recombination lifetime. Author contributed within improvements of the instrument VUTEG-5-AIDA. The main results were presented at a number of international (IWORID14, “Radiation Interaction with Material and Its Use in Technologies 2012 and 2014”) and national (LNFK39 and LNFK40) conferences and several drafts of results for manuscripts and presentations were prepared by the author.

Measurements of recombination characteristics were performed in collaboration with PHD students J. Pavlov, D. Shevchenko and D. Meskauskaite as well as Dr. T. Ceponis and Dr. A. Uleckas. Most of in situ measurements at accelerators State Research Institute Centre for Physical Sciences and Technology, Vilnius and at CERN were performed by a group and under supervision of Dr. Sc. E. Gaubas. All the investigations, data analysis and writing of manuscripts were made by Dr. Sc. E. Gaubas or under supervision of Dr. Sc. E. Gaubas.

In situ experiments on study of carrier lifetime and scintillation characteristics during protons implantation were performed by ion accelerator installed at State Research Institute Centre for Physical Sciences and Technology, Vilnius.

Publications. The main results of this study are published within 11 scientific articles [A1 – A11] and the research results have been approved within 13 oral and poster presentations [P1 – P13] at conferences.

Articles:

A1. E. Gaubas, V. Borschak, I. Brytavskyi, T. Ceponis, V. Kalendra, V. Smyntyna, **A. Tekorius**, *Spectroscopy of deep traps in* $CdS\text{-}Cu_2S$ *junction structures*, Materials Science and Engineering B (2012), **5(12)**, 2597-2608.

A2. **A. Tekorius**, E. Gaubas, T. Čeponis, A. Jasiūnas, A. Uleckas, J. Vaitkus, A. Velička, *Dosimetry of background irradiations of accelerators based on hadrons fluence dependent carrier lifetime measurement,* Proceedings of the 4th International conference "Radiation interaction with material and its use in technologies 2012, Program and materials (2012), pp. 282-285.

A3. E. Gaubas, V. Kalendra, T. Ceponis, A. Uleckas, **A. Tekorius**, J. Vaitkus, A. Velička, *Study of deep level characteristics in the neutrons irradiated Si structures by combining pulsed and steady-state spectroscopy techniques,* Journal of Instrumentation (2012), JINST **7** C11006.

A4. E. Gaubas, V. Kovalevskij, A. Kadys, M. Gaspariūnas, J. Mickevicius, A. Jasiūnas, V. Remeikis, A. Uleckas, **A. Tekorius**, J. Vaitkus, A. Velička, *In situ variations of recombination characteristics in MOCVD grown GaN epi-layers during 1.7 MeV protons irradiation,* Nucl. Instrum. Meth. Phys. Res. B **307** (2013) 370–372.

A5. E. Gaubas, V. Borschak, I. Brytavskyi, T. Čeponis, D. Dobrovolskas, S. Juršėnas, J. Kusakovskij, V. Smyntyna, G. Tamulaitis, **A. Tekorius**, *Nonradiative and Radiative Recombination in CdS Polycrystalline Structures*, Advances in Condensed Matter Physics, 2013 (2013) ID917543.

A6. E. Gaubas, T. Ceponis, A. Jasiūnas, E. Jelmakas, S. Juršėnas, A. Kadys, T. Malinauskas, **A. Tekorius**, P. Vitta, *Study of carrier recombination transient characteristics in MOCVD grown GaN dependent on layer thickness*, AIP Advances **3**, (2013), 112-128.

A7. E. Gaubas, T. Ceponis, A. Jasiunas, V. Kovalevskij, D. Meskauskaite, J. Pavlov, V. Remeikis, **A. Tekorius**, J. Vaitkus, *Correlative analysis of the in situ changes of carrier decay and proton induced photoluminescence characteristics in chemical vapor deposition grown GaN*, Appl. Phys. Lett. **104**, 062104 (2014).

A8. E. Gaubas, D. Meskauskaite, I. Brytavskyi, T. Ceponis, J. Pavlov, A. Jasiunas, V. Remeikis, V. Kalesinskas, G. Tamulaitis, V. Kovalevskij, **A. Tekorius**, *In situ variations of carrier decay and proton induced luminescence* *characteristics in polycrystalline CdS,* Journal of Applied Physics **115** (2014) 243507.

A9. **A. Tekorius**, E. Gaubas, T. Čeponis, A. Jasiūnas, V. Kovalevskij, D. Meškauskaitė, J. Pavlov, V. Remeikis, J. Vaitkus, *In situ and ex situ study of variations of recombination characteristics in MOCVD grown GaN under hadron irradiations,* 5th International conference „Radiation interaction with materials: fundamentals and applications 2014“, Kaunas, 2014, Program and materials (2014), P3-25, pp. 436-439.

A10. **A. Tekorius**, E. Gaubas, T. Čeponis, J. Pavlov, J. Vaitkus, M. Glaser, M. Moll, *Fluence and anneal dependent variations of recombination parameters in Si irradiated by 26 GeV protons,* 5th International conference „Radiation interaction with materials: fundamentals and applications 2014“, Kaunas, 2014, Program and materials (2014), P3-24, pp. 432-435.

A11. T. Ceponis, E. Gaubas, V. Balevicius, S. Galkin, A. Jasiunas, K. Katrunov, V. Kovalevskij, J. Pavlov, V. Remeikis, D. Shevchenko, G. Tamulaitis , **A. Tekorius**, *Comparative Study of Scintillation Characteristics of CdS and ZnSe Varied during 1.6 MeV Proton Irradiation,* 5th International conference „Radiation interaction with materials: fundamentals and applications 2014“, Kaunas, 2014, Program and materials (2014), P3-17, pp. 405-408.

Presentations at conferences:

P1. A. Uleckas, E. Gaubas, T. Čeponis, **A. Tekorius**, V. Kovalevskij, V. Remeikis, *Barjerinės talpos elektrinimo srovių kaitos tyrimas Si detektoriuose apšvitinimo 1.5 MeV energijos protonais metu,* 39-oji Lietuvos nacionalinė fizikos konferencija, Vilnius, 2011.

P2. A. Velička, T. Čeponis, E. Gaubas, A. Uleckas, **A. Tekorius**, *Technologinių defektų iškaitinimo tyrimai Si tiristoriniuose dariniuose talpiniais ir giliųjų lygmenų spektroskopijos metodais,* 39-oji Lietuvos nacionalinė fizikos konferencija, Vilnius, 2011.

P3. **A. Tekorius**, E. Gaubas, T. Čeponis, A. Jasiūnas, A. Uleckas, J. Vaitkus, A. Velička, *Dosimetry of background irradiations of accelerators based on hadrons fluencee dependent carrier lifetime measurement,* 4th International conference “Radiation interaction with material and its use in technologies“ 2012.

P4. V. Kalendra, E. Gaubas, T. Čeponis, J. Vaitkus, A. Uleckas, **A. Tekorius**, *Study of deep level characteristics in the hadrons irrdiated Si detectors by combining pulsed and steady-state spectroscopy techniques,* 14th International workshop on radiation imaging detectors, Figueira da Foz, Coimbra, Portugal, 2012.

P5. **A. Tekorius,** E. Gaubas, T. Čeponis, V. Kovalevskij, V. Remeikis, I. Brytavskyi, *In situ modification of* CdS-Cu_2S *structures during irradiation by protons,* 40-oji Lietuvos nacionalinė fizikos konferencija, Vilnius, 2013.

P6. **A. Tekorius**, E. Gaubas, J. Vaitkus, M. Glaser, M. Moll, *Variations of recombination parameters under anneals in Si structures irradiated by hadrons,* 40-oji Lietuvos nacionalinė fizikos konferencija, Vilnius, 2013.

P7. **A. Tekorius**, E. Gaubas, T. Čeponis, J. Vaitkus, *Hadronų greitintuvų foninių apšvitų dozimetrija,* 3-oji jaunųjų mokslininkų konferencija „Fizinių ir technologijos mokslų tarpdalykiniai tyrimai“, Vilnius, 2013.

P8. E. Gaubas, T. Čeponis, **A. Tekorius**, J. Vaitkus, *Silicon single crystals for radiation monitoring imaging by the free carriers lifetime measurement,* 15th International Workshop on Radiation Imaging Detectors, Paris, 2013.

P9. E. Gaubas, T. Čeponis, **A. Tekorius**, J. Vaitkus, V. Fadeyev, H.Sadrozinski, *Preliminary results on measurements of surface recombination velocity on slim-edge passivated Si structures,* 23rd RD50 Workshop on Radiation hard semiconductor devices for very high luminosity colliders, Geneva, 2013.

P10. E. Gaubas, T. Ceponis, A. Uleckas, **A. Tekorius**, J. Vaitkus, M. Glaser, M. Moll, *Hadrons fluence measurements based on carrier lifetime control,* 2nd AIDA Annual Meeting, Frascati, 2013.

P11. **A. Tekorius**, E. Gaubas, T. Čeponis, A. Jasiūnas, v. Kovalevskij, D. Meškauskaitė, J. Pavlov, V. Remeikis, J. Vaitkus, *In situ and ex situ study of variations of recombination characteristics in MOCVD grown GaN under hadron irradiations*, 5th International conference "Radiation interaction with materials: fundamentals and applications 2014", Kaunas, 2014.

P12. **A. Tekorius**, E. Gaubas, T. Čeponis, J. Pavlov, J. Vaitkus, M. Glaser, M. Moll, *Fluence and anneal dependent variations of recombination parameters in Si irradiated by 26 GeV protons,* 5th International conference "Radiation interaction with materials: fundamentals and applications 2014", Kaunas, 2014.

P13. T. Ceponis, E. Gaubas, V. Balevicius, S. Galkin, A. Jasiunas, K. Katrunov, V. Kovalevskij, J. Pavlov, V. Remeikis, D. Shevchenko, G. Tamulaitis, **A. Tekorius**, *Comparative Study of Scintillation Characteristics of CdS and ZnSe Varied During 1.6 MeV Proton Irradiation,* 5th International conference "Radiation interaction with materials: fundamentals and applications 2014", Kaunas, 2014.

Structure of dissertation. The research problems, scientific relevance and novelty, objectives of the research and practical importance are discussed within Introduction section. The statements to defence as well as author contribution are there determined in the Introduction section. In Chapter 2, the large fluence dosimetry methods are briefly reviewed to ground motivation of this research. In Chapter 3 there are discussed the materials and samples investigated as well as the research techniques applied. The surface passivation of slim edge Si detectors evaluations, the fluence dependent carrier recombination lifetime characteristics and spectral parameters ascribed to radiation induced point-like defects are discussed in Chapter 4. The results of the research of the initial material and of junctions made of Cu_2S-CdS are presented in Chapter 5. The parameters of carrier pair production and of radiation defect introduction rate in CdS polycrystalline layers are presented and methods for their extraction are also discussed in Chapter 5. Evaluations of the parameters of the technological and of the radiation defects in MOCVD grown GaN epi-layers are discussed in Chapter 6. The designed and fabricated large fluence dosimeter based on contactless measurements of the carrier recombination lifetime in Si wafer fragments is described in Chapter 7. The general conclusions are presented at the end of dissertation.

II. Brief survey on techniques of hadrons irradiation dosimetry

2.1. Methods based on nuclear reactions

Radioactivity of materials can be induced by interaction of the sensor material with radiation of energy exceeding the threshold value for initiation of nuclear reactions. This process is called activation and it is used in production of radioactive sources and activation detectors. Radiation that is emitted by such material is referred to as residual radiation. Activated materials emit mostly γ- and β- particles. Nevertheless, the heavy particle emitting materials can be activated too.

The nuclear decay starts just after the beginning of irradiation, which means that both processes, namely, activation and decay, take place at the same time. The rate of decay is evaluated by the half-time of the newly activated material.

A thin foils of a relevant material, placed in the large fluence radiation field for a time longer compared to the half-life of the activated material, is used as activation sensor. After irradiation the decaying particles in the sensor foil are detected by the decay counters. The activation rate and radiation field is determined by the count of decaying particles. The exponential increase in the activity reaches an asymptotic value equal to the activation rate since the decay rate depends on the number of activated atoms, the number of which increases with time [6, 8]. Thus, the fluence measurement based on the foil radiative activation can be exploited for evaluation of high energy (over the threshold value for definite material) particle fluence. These nuclear reactions based techniques are exceptionally suitable for evaluation of large fluences. However, application of these techniques can be exploited in relatively narrow range of fluences and impinging particle energies.

2.2. Techniques based on EPR spectroscopy of radiation induced free radicals

The action of ionizing radiation on matter primary yields charged particles and excited molecules. In solid inorganic materials the liberated free electrons may be trapped by the crystal lattice whereas in solutions the solvent is also under irradiation and thus plays an important role in the overall process. In solid organic compounds the primary active particles are transformed into free radicals and some final products of radiolysis.

EPR (electron paramagnetic resonance) spectrometry is a possible “reading” technique based on measurement of the unpaired spin ascribed to concentration of free radicals in organic materials. Unpaired electrons absorb microwave energy as they reverse their magnetic moments affected by an intense magnetic field [9]. By scanning absorbed microwaves in a variable magnetic induction field the EPR spectra are recorded. Spectrometers use combination of magnetic field modulation and phase sensitive microwave absorption detection that improves reduction of noise in spectrum recording. The spin attributed resonances are given as the first derivative of the absorbed microwaves with respect to the magnetic induction field and represents a specific structure. Concentration of free radicals is proportional to signals peak-to-peak amplitude. Thereby, EPR spectroscopy of irradiated sensors can be employed for dosimetric evaluation of absorbed dose. It is done by measuring the concentration of stable radicals created in material by radiation. X-band (10 GHz) microwaves are routinely used for such measurements. It is applied for dosimetry in radiation processing by measuring radicals of the amino acid alanine [10, 11].

Free radicals are produced not only by ionizing radiation. UV light and mechanical impacts usually produce radicals of different kind that are responsible for the background EPR signal in some materials. This determines limitations for precision of low dose measurements. Another limitation is attributed to stability of the radiation induced radicals. Radical recombination in solids still persists, even though it is much slower than in liquids. The average lifetime of radicals can vary from a few hours to a few years. Recombination rate depends not only on sample material, but also it is sensitive to the ambient temperature and humidity. Sample freezing can greatly prolong the recombination process.

Alanine can be used either as a reference or as a routine dosimeter, - it just has to be calibrated accordingly. The radiation chemical yield of the alanine dosimeter is additionally influenced by temperature during irradiation. Fortunately, it is independent of radiation type and energy for the range of MeV energy photon and electron beams. At lower energies, dosimeters have to be calibrated accordingly to the type and energy of radiation in which they are going to be used.

2.3. Electrical methods grounded on radiation damage of particle detectors

The ionizing radiations, such as electrons, protons, α-particles, or not directly ionizing particles like photons or neutrons, interact with semiconductor material, and a number of electron-hole pairs that can be registered as electric signals, are created. For charged particles, ionization occurs along the flight path by many collisions with electrons. Photons interact with matter through a photoionization or Compton effect (by interacting with a target electrons), or interacts with a nucleus of material. In both cases absorbed energy is transformed into electron-hole pair creation and lattice vibrations (phonons) and finally into thermal energy.

Energy conversion to electron-hole pairs is a property of semiconductor materials. It almost does not depend on radiation type and its energy [4, 12]. The increase or decrease of the density of free carrier pairs in the depletion region causes the change in reverse bias current, a profound effect which is caused by radiation induced defects acting as carrier generation centres. During initial irradiation, the increase in leakage current is observed due to production of charge traps in the forbidden energy gap. The probability of carrier pair production increases after prolonged irradiation, as the deep energy levels are introduced in the forbidden gap and leakage current is significantly increased. The unwanted changes of detector performance such as noise increase and worsening of signal to noise ratio are caused by increase of this leakage current. For detectors used in hostile radiation environments where radiation induced damage is very high, the strong dependence of the thermal emission energy on temperature allows the compensation of leakage current by decreasing the sensors operation temperature.

The effect of the leakage current can thereby be employed for dosimetry. It had been established [1, 13, 14] that a rather linear increase of leakage current with irradiation fluence exists in Si pin diodes. However, this leakage current strongly depends on the applied reverse voltage. Such type dosimetry sensors can be stabilized by fixing reverse voltage and temperature parameters. However, the leakage current control based sensors are operational only if diode survives under irradiations and bulk thermal generation current prevails. In other cases, the sufficiently high voltages should be kept to reach the sufficient charge collection efficiency. On the other hand, the leakage current sensitive dosimeters are rather expensive, as it requires an electronic grade technology to fabricate these dosimeters.

By integrating many small detectors together, the position sensitive detectors of large area are built. The rather complicated structures such as arrays of silicon strip detectors or pad detectors can serve as the large area position sensitive dosimeters and imagers. Such devices are widely used in medical tomography. However, such instruments are functional only in the range of low fluences. On the other hand, aging of the imagers-dosimeters that operate in harsh areas of irradiations is a serious issue. In this case the strips are segmented down to a pixel structure, the read-out electronics is adapted to small capacitances and is designed to handle DC coupling to the pixel implants. Each pixel of the detector is individually connected to its own electronics. This is the so-called hybrid pixel detector, hybrid because both sensor and electronics chips are fabricated separately and then joined [15-21]. The dosimetry parameters can then be evaluated by I-V and C-V measurements. From C-V measurements one can obtain the full depletion voltage which is related to the collected dose.

Alternatively to leakage current measurements, the quantitatively more precise technique is the deep level transient spectroscopy (DLTS) in junction structures it is based on measurements of variations of capacitance transients with temperature when depletion width of a diode is harmonically modulated by external test voltage [22]. There the radiation induced density of carrier traps can be attributed to definite type of radiation defects. Thus, DLTS probe dosimetry can be suitable in special cases of rather small dose measurements. However, it is not a rapid dosimetry technique which application for in situ operation is rather complicated. The supplementary techniques, such as recombination and generation lifetime control in *p-n* structures can be involved by combining measurements of current-voltage (I-V) characteristics with capacitance-voltage (C-V) characteristics [13, 23, 24]. More efficient technique for rapid dosimetric readings of radiation damage of junction structure can be the pulsed capacitance measurement method. Components of barrier capacitance charging current and of generation current can there be separated by analyzing the pulsed transients obtained under linearly increasing voltage (BELIV) biasing [14]. Unfortunately, in applications of these last techniques, the expensive, electronic grade sensors are required.

2.4. Scintillation techniques

Scintillators are commonly the insulators based on wide-bandgap materials that exhibit the luminescence and phosphorescent features. The optical range of luminescence light is usually determined through deep centres. Usually, the luminescence centre is a composition of two energy levels separated by electronic transitions energy gap which is equal to the energy of photons in and around the visible region of electromagnetic spectrum. Typical luminescence efficiency of scintillation materials is about 10-15%. This implies that scintillation itself is not a very efficient process. However, the scintillator used together with a photon detector of high photon collection and counting efficiency turns to be an efficient radiation sensor, if radiation defects are efficient scintillation centres.

The scintillator may consist of a crystal, plastic or organic liquid. When a charged particle strikes the scintillating material, atoms are excited and photons are emitted. By using photomultiplier tube, a photocurrent amplification effect can be realized. For each photon detected, ones get an output signal in the form of a measurable pulse which is passed to the data-processing electronics. This pulse carries the information about the energy of original incident radiation so the rate of irradiation can be measured.

Nowadays, the photomultiplier tubes based on semiconductor technology with internal high voltage sources are produced. Its efficiency can reach almost 80% that makes it ideal for measurements in low level radiation environments. One more sensitive photodiode detector type for low radiation detecting is the avalanche photodetector. It is analogical to electron multiplication in photomultiplier tube except that it does not have mechanical parts that make the system more resistive to mechanical shocks.

Different scintillating materials are exploited for detection of definite type of radiations. For example, CsI in crystalline form detects efficiently the protons and α–particles, while ZnS is used more widely for detection of α-particles. NaI compound containing thallium is the most relevant for detection of gamma rays, and LiI is mostly exploited for detection of neutrons.

Scintillation light pulse rises very quickly with a typical rise time of less than a nanosecond. The decay time may vary from a few nanoseconds up to several milliseconds, and this is the biggest problem for scintillator sensors use in high rate and large fluence radiation dosimetry [25, 26].

2.5. Several dosimetry problems to solve

Methods based on nuclear reactions using foils are limited by a measurement applied to a single exposure. They have to be taken out and read after each use. It makes such method not suitable for devices with hard to reach (assembly/disassembly) target. Other downside of foils is determination of nuclear transmutation types.

The junction based collected dose readers using DLTS, I-V, C-V and other techniques allow evaluation only of the integral parameters of the electrically active traps. The EPR based dosimetry can be used in wide range of fluences, however, it is limited by necessity to exploit a big set of reference dosimeters. Then the controlled radiation spectrum has to be split into many smaller ranges in order to measure fluences of several orders of magnitude. This also requires the usage of a set of dosimeters in monitoring of wide fluence range of irradiations.

The luminescence efficiency of most scintillators can vary from a few to about thirty percent. Such low efficiency indicates that most of the incident radiation delivered energy is lost by non-radiative transitions and thermal excitation of the scintillator material. In sensors of low radiation efficiencies, the need of usage of the photomultiplier tubes arises.

Plastic scintillators are highly sensitive to radiation damage compared to least sensitive liquid type scintillators, however all the types of scintillators are not tolerant to radiation damage. Thereby, research of degradation of the sensor responses is essential in applications for dosimetry of high radiation fields.

III. Test structures and characterization techniques

3.1. Investigated materials and samples

3.1.1. Slim edge passivated Si strip detectors

Devices with “slim edges” have been fabricated to reduce the inactive area of a large area strip detectors. The standard devices have wide inactive areas at the periphery, ~1 mm wide with large hermeticity gaps. It is possible to use sensor overlaps or more tracking layers, but this complicates construction of large-area trackers in HEP and in some medical applications. To make the slim edge structures the method scribe–cleave–passivate (SCP) is rather effective. Scribing and cleaving steps result in high surface quality on the side wall. Another method to remove the inactive peripheral region is a sidewall doping [27, 28]. The advantage of the SCP is that SCP method is applicable to both n- and p-type bulk silicon sensors, overcoming special processing procedures as side wall implantation.

Devices with “slim edges” enable better construction and tracker performance. The cutting (especially cleaving) and proper passivation (oxide/nitride for n-type and alumina for p-type) makes it possible to put the edge close to the active area and still have low leakage current and high breakdown voltage. However, the electrical passivation of cleaved side walls is then inevitable. The passivation with proper interface charge repels the carriers from the side wall boundary similarly to the voltage drop along the top surface in the guard ring region of sensors or corona charging surface passivation technique [29, 30].

The samples were prepared by the through-cut done by a laser and passivation was a “nanostack” of SiO_2 and Al_2O_3 deposited by the atomic layer deposition (ALD) method [31, 32, 33] in the n-type Si wafers. The p-type conductivity Si wafer structures were prepared by the through-cut by a conventional saw and the consequent passivation by the plasma enhanced chemical vapour deposition (PECVD) of Si_3N_4 layers. The leakage current for both sample sets was the order of magnitude of a few μA at full depletion condition. This is about an order of magnitude higher level than what was in the case of scribing and cleaving.

The other issue in fabrication of such an edge-less large area sensor is radiation hardness and possible sidewall passivation failing under irradiations [34]. Due to the slim edge configuration, this may lead to a higher level of leakage current than expected from the bulk contribution. The n- and p-type devices should be assessed separately due to the difference of the required techniques of passivation. The n-type devices can be passivated by PECVD, while only ALD deposition of Al_2O_3 is relevant for the p-type sensors due to its almost unique feature of having a negative interface charge on the silicon surface.

Table 3.1. Parameters of samples and irradiations of slim edge Si strip detectors

Non-irradiated			
p-type detector, p-Si, non-passivated	p-type (N-on-P) detector, p-Si, passivated with ALD alumina	n-type detector, n-Si, non-passivated	n-type detector (P-on-N), n-Si, passivated with PECVD nitride
Sample notification Wafer, No.	Sample notification Wafer, No.	Sample notification Wafer, No.	Sample notification Wafer, No.
W18, No. 3	8	2	5
W16, No. 2	9	2a	6
W16, No. 3	10	3	7
ATLAS Φ7 No.3	11	3a	-
ATLAS Φ7 No.5	12	-	-
Irradiated			
Sample notification Wafer, No.	Fluence (neq, cm^{-2})		
B1P6	0.95×10^{13}		
B2P10	5.78×10^{13}		
B2P8	4.82×10^{14}		
B2P3	3.98×10^{15}		

Additionally it was unveiled that performance of sidewalls of the p-type devices after large fluence 8×10^{14} neq/cm^2 and 4.0×10^{15} neq/cm^2 proton irradiations was sufficient relative to suppressed leakage currents, while the insufficient sidewall passivation issues appeared at lower fluences. Due to the decreased contribution of the edge current in the heavier irradiated material, the edge became more resistive, and the effect of increased breakdown voltage after irradiating saw-cut non-passivated devices appeared [34]. Therefore, both oxide and nitride types of p-type Si sidewall passivated samples were involved into study of modifications of the surface recombination. In case of alumina passivation of the silicon surface there is always a presence of a thin layer of silicon oxide between the alumina and the silicon. And, in fact, it is the tetrahedral structure of the oxide that causes the alumina to be tetrahedral coordinated near the surface. Dominance of tetrahedral units of AlO_4 over octahedral Al^{3+} results in proximity of negative charge near the boundary. The oxide layer would gain more positive charge during first few Mrad of ionizing dose, counteracting the negative charge from alumina. Therefore, the non-irradiated and irradiated samples were taken in comparative consideration of surface recombination changes. The sets of samples for investigation and the parameters of irradiations are denoted in Table 3.1.

3.1.2. Si wafer fragment test structures

The aim of these measurements was to perform the tentative calibration measurements for fast and non-invasive dosimetry of irradiation fluence, based on excess carrier lifetime in Si dependence on collected hadron irradiation fluence. The main calibration measurements were performed using a set of n-type Czochralski with applied magnetic field (MCZ) grown Si wafer fragments of dimensions of 10×10 mm^2. This material was produced and supplied by Okmetic vendor. Wafers of 300 μm thickness were passivated with thermal oxide. Then these wafer fragment samples were neutron irradiated at nuclear reactor facilities at Ljubljana. Sets of these samples were prepared by neutron irradiations with fluences of 10^{11}, 10^{12}, 10^{13}, 10^{14}, 3×10^{14}, 10^{15}, 3×10^{15}, 10^{16} and 3×10^{16}cm^{-2} neq. Additionally, a set of pin diode structures, made of n- and p-type CZ Si material as well as epi-Si, irradiated by reactor neutrons and 50 MeV protons were involved into calibration measurements.

Further measurements were performed using a tentative instrument VUTEG-5-AIDA fabricated at Vilnius University within 8.3 work-package of the FP7 project AIDA, in order to identify necessity of future modifications of the VUTEG-5-AIDA dosimeter. This study was made on the as-irradiated FZ and CZ Si wafer fragments of n- and p-type conductivity material. Two sets of ~300 μm thick Si wafer pieces of dimensions 10×10 mm were investigated to clarify whether radiation defect production by proton beam depends on material conductivity type and growth technology. Parameters/signatures of samples are listed in Table 3.2. One batch of nine samples was composed of n-type FZ Si grown wafer pieces, irradiated with 26 GeV proton fluences varied in the range from 10^{12} to 10^{16} cm^{-2} neq. Another set of nine samples was composed of p-type CZ Si grown wafer pieces, irradiated within the same range of fluences. These samples (kept in de-activation storage area) just after irradiation with 26 GeV protons, to avoid transformations of the radiation defects, were additionally rapidly annealed after primary measurements on the just irradiated material. After the primary carrier lifetime measurements had been completed on the as-irradiated samples, samples were isothermally annealed at 80 C in oven while varying heat treatment duration. The lifetime measurements had been performed on all the samples under study after each anneal step. Anneal duration was changed in steps by nearly doubling the exposure time ($t_{exp,\ n}$), leading to the total exposure time for each step as $t_{exp,n}=t_{exp,\ n-1}+2t_{exp,\ n-1}$ and $t_{exp,\ n+1}=t_{exp,\ n}+2t_{exp,\ n}$. Thereby, the last heat treatment exposure stretch was 30 min, comprising the nearly 1 h total heating duration.

Table 3.2. Parameters of irradiations of the investigated FZ n-type and CZ p-type Si samples.

Set	$\Phi_{\text{requested}}$ (p/cm^2)	Φ_{achieved} (p/cm^2)
1824	10^{16}	8.47×10^{15}
1825	5×10^{15}	5.04×10^{15}
1826	10^{12}	1.13×10^{12}
1827	5×10^{12}	6.01×10^{12}
1828	10^{13}	1.4×10^{13}
1829	5×10^{13}	6.01×10^{13}
1830	10^{14}	9.08×10^{13}
1831	5×10^{14}	5.46×10^{14}
1832	10^{15}	9.77×10^{14}

Carrier lifetime measurements were performed in the centre of regular tetragon keeping the precision of location of scan position not worse than 2 mm. The acquired data led to the conclusion, that a proton beam diameter had been less than the largest dimension of a wafer piece. The additional tests confirmed the lateral variation of carrier lifetime values of about 2-3 times, being the shortest in the central area, while lifetime increases going to periphery areas. Scanning precision is determined by a width of slit antenna for probing microwaves (MW) and excitation laser beam spot, and is about 100 μm in direction perpendicular to MW antenna slit.

The tentative dosimetry measurements were performed using a special sample compartment where the Si sample in plastic bag under test is placed for measurements, as shown in Fig. 3.1.

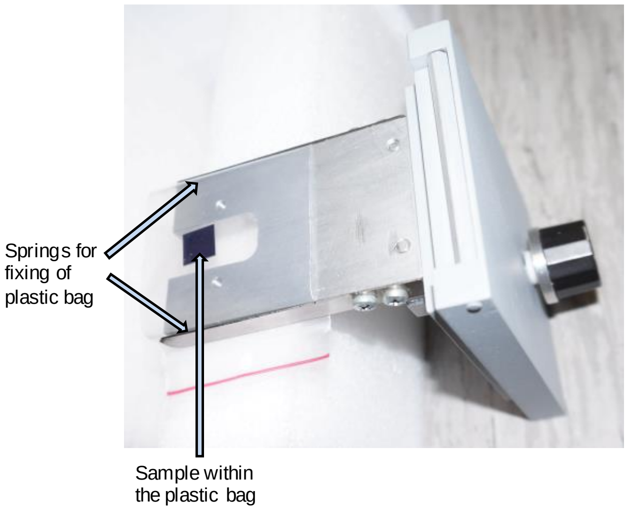

Fig. 3.1 Sample compartment and samples in plastic bag placed for dosimetry measurements.

3.1.3. GaN epi-layered structures

A set of wafer pieces of 2.4–25.5 μm thickness n-GaN un-intentionally doped epi-layers grown by the metal-organic chemical vapour deposition (MOCVD) on sapphire substrates was investigated. For comparison, a few samples (2.4 μm thick) grown by Tokushima University (TU) MOCVD reactor and the different thickness GaN epi-layers grown by MOCVD reactor at Vilnius University (VU) were simultaneously investigated. The thick layers (VU) were grown by using the technique of several step re-growths. The sample parameters evaluated by Hall and high resolution X-ray diffraction (HRXRD) measurements are listed in Table 3.3.

Table 3.3. Parameters of the MOCVD GaN samples extracted by Hall effect and HRXRD measurements.

Sample number made by/under regime	Layer thickness (μm)	Carrier density (cm^{-3})	Carrier mobility (cm^2/Vs)	Threading dislocation density (cm^{-2})
1047 TU/1047^{0}C	2.4	n/a	n/a	$>10^{10}$
950 TU/ 950^{0}C	2.4	n/a	n/a	$>10^{10}$
925 TU/ 925^{0}C	2.4	n/a	n/a	$>10^{10}$
53 VU/1070^{0}C	2.5	4.5×10^{17}	199±3	1.3×10^{9}
38 VU/1070^{0}C	5.6	4.2×10^{17}	191±3	8.6×10^{8}
181 VU/1070^{0}C	13.1	8.7×10^{16}	210±6	6.2×10^{8}
184 VU/1070^{0}C	19.5	4.0×10^{16}	214±6	5.1×10^{8}
185 VU/1070^{0}C	25.5	2.9×10^{16}	190±6	4.8×10^{8}

As can be deduced from the Table 3.3, the density of free carriers varies reciprocally relative to an epi-layer thickness. This implies that the effective density of the rather shallow donor-type traps decreases with enhancement of a crystal volume. Such behaviour requires a clarification whether these traps are localized at the layer surfaces, which role is reduced with enhancement of a layer thickness, i.e. the ratio of the surface area to the crystal bulk. The measured values of carrier mobility can be assumed to be invariable in the range of experimental errors of 10%. This hints that the grown-in defects make a rather weak impact on carrier scattering, while being the efficient recombination centres responsible for the luminescence. The total threading dislocation density (TDD), estimated by HRXRD and verified by EBIC measurements, is also presented in Table 3.3. It can be noticed that the highest TD density is inherent for the TU made GaN layers, while this TD density decreases reciprocally to the layer thickness in VU grown GaN epi-layers. TDD, in the VU made samples, changes more than two times over the entire range of the examined layer thicknesses. Overall, the described sample set, especially the TU grown epi-layers, should be considered as a rather dislocation-rich with TDD>5×10^{8} cm^{-2}.

3.1.4. CdS polycrystalline layered and Cu_2S hetero-junction structures

Copper sulphides attract considerable attention due to their various stoichiometric compositions, unique structures, and potential applications in numerous fields [35, 36]. Copper sulfide has several stable and metastable phases, with at least five of them being stable at room temperature [37]. Variations in stoichiometry and valence state affect the structural, optical, and electrical properties of copper sulphides. Thin layers of copper chalcogenide compounds have a number of applications in solar cells, super-ionic conductors, photo-detectors, photothermal converters, conductive electrodes, and microwave shielding coatings [38, 39]. Chalcocite type copper sulfide Cu_2S is a promising p-type semiconductor for solar cells, optical filters, nanoswitches, thermoelectric and photoelectric transformers, and gas sensors [40-42]. Cadmium sulphide is an extensively studied semiconductor with possible applications in fabrication of various optoelectronic devices [43] based on CdS polycrystalline films obtained by vacuum deposition [44], thermal evaporation, sputtering, chemical spraying, silk screen printing, sintering, chemical printing and electrophoretic deposition [45-49]. Cu_2S-CdS heterojunction structures are usually formed by wet dipping of a pre-etched vacuum evaporated CdS film into hot solution of CuCl [45]. Solid state reactions (dry processing) [46], vacuum evaporation [47], sputtering [48], spray pyrolysis [49], and sulphurisation of Cu films [50] have also been applied for the production of Cu_2S films on CdS substrate.

The polycrystalline films containing Cu_2S-CdS heterostructures formed at Odessa I. Mechnikov University by dry deposition method [51] have been investigated. The heterostructures were formed by employing a substitution technique when a layer of copper sulphide is formed directly on the substrate layer of CdS during heat treatment using a pre-printed copper chloride film, formed by vacuum evaporation. However, such a heterojunction consisting of p-type Cu_2S and n-type CdS is a rather complicated heterostructure because of the interface between two materials with different electron affinities, band gaps, and polycrystalline structures. The lattice mismatch and inter-diffusion of components might cause defects at or near the interface that strongly affect the junction properties. In particular, it is shown that copper diffusion into the adjacent CdS layer changes stoichiometry of the Cu_xS layer and might form shunting channels within the CdS layer [52]. Due to polycrystalline structure and lattice mismatch between the adjacent layers, a large density of trapping and recombination centres occurs. These disordered material areas cause the effect of photo-induced modulation of junction potential barrier. Thereby an issue of junction stability is also unsettled. To evaluate the impact of traps on parameters and stability of heterojunctions, the barrier capacitance characteristics have been studied.

Substrate temperature and layer deposition duration were the main parameters varied during the heterojunction formation process. The thickness of the base layer defines its resistivity and the size of the formed microcrystals. Samples with the thicker base CdS layer were ascribed as the type-I samples. The separated types of samples can be sorted by an extent of formed hexagonal $Cu_{1.92}S$ by correlation with Cu_xS layer thickness. The longer is the CuCl film deposition time, the higher partial fractions of the hexagonal $Cu_{1.92}S$ and of the monoclinic Cu_7S_4 can be detected in the type-II samples, as determined from X-ray diffractometry (XRD) patterning (Fig. 3.2).

The phase composition of the layers was examined by an X-ray diffractometer (D8 Advance Bruker AXS with Cu K_α radiation). The symmetrical Θ/2Θ configuration and grazing incidence (GIXRD) regimes were employed in the X-ray diffraction (XRD) measurements. In the case of GIXRD, the incidence angle Θ was equal to 0.5°. The XRD patterns were measured in 2Θ range from 20 to 70° using a step scan mode, where the step size (Δ2Θ) was of 0.04° keeping a counting duration of 5 s.

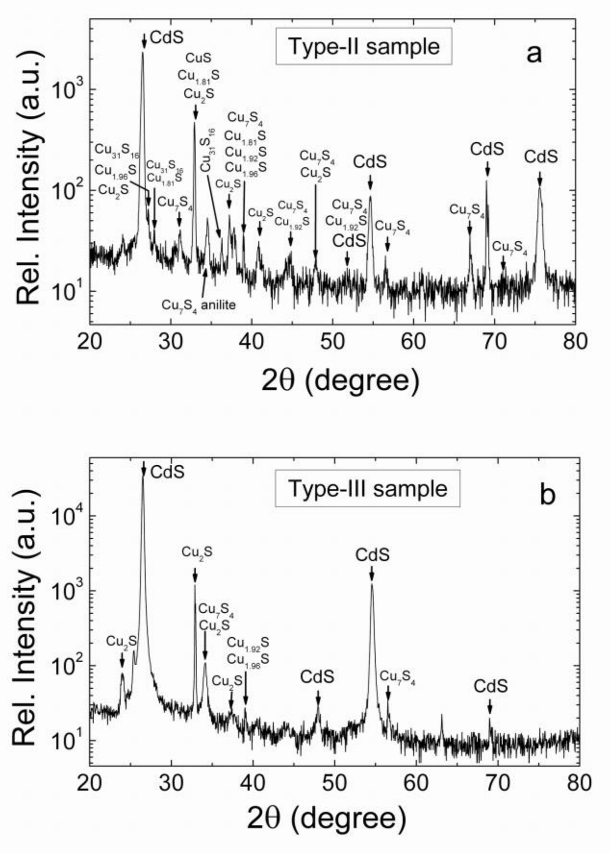

Fig. 3.3. XRD patterns measured in Cu_2S-CdS heterojunctions of type-II (t_{dep}=8 min, T_{sb}=220 ºC) and type-III (t_{dep}=6 min, T_{sb}=190 ºC).

Table 3.4. Number of the XRD peaks associated with different Cu_xS_y compounds revealed within diffractographs measured in type -I, -II, and -III samples.

Cu_xS_y compound	Sample type		
	Type-I	Type-II	Type-III
monoclinic Cu_2S (chalcocite)	4	5	5
tetragonal $Cu_{1.96}S$	1	2	4
monoclinic $Cu_{31}S_{16}$ (djurleite)	0	3	0
hexagonal $Cu_{1.92}S$	1	3	4
tetragonal $Cu_{1.81}S$	2	3	2
hexagonal Cu_9S_5 (digenite)	0	0	0
monoclinic Cu_7S_4 (roxbyite)	1	10	5-6
orthorhombic Cu_7S_4 (anilite)	0	1	0
hexagonal CuS (covellite)	0-1	0-1	0-1

The stoichiometry changes within copper sulphide layer have been resolved within XRD patterns. The observed diffraction angles and relative intensities of the XRD peaks of the CdS-Cu_xS layers are illustrated in Fig. 3.2 (a) and (b) for type-II and type-III samples, respectively. The peaks corresponding to different Cu_xS_y compounds were identified by the diffraction angles taken from JCPDS cards and are indicated by arrows in Fig.3.2. The $Cu_{1.96}S$, $Cu_{1.92}S$, $Cu_{1.81}S$ and other modifications together with Cu_2S were detected by XRD characterization and are listed in Table 3.4. This implies that copper atoms diffuse from the Cu_2S layer into the base CdS layer during the layered structure fabrication process. The copper in-diffusion probably proceeds, though at a lower rate, also after the heterojunction formation is completed. Thus, aging of the structure might be expected. The impurities diffused into CdS layer can serve for formation of acceptor centres that compensate or even over compensate the donors initially existing in the CdS layer [52]. The conditions for Cu diffusion are directly determined by the deposition time t_{dep} and the substrate temperature $T_{sb},$ thereby resulting in variations of the electrical characteristics of junction structures. This primary thermal treatment defines the intensity and depth of the Cu in-diffusion. The XRD study indicates that type-II samples contain a larger amount of Cu_xS

phase precipitates (Fig. 3.2a) than type-III samples. Type-II samples were fabricated at the longest deposition time t_{dep} and the highest temperature T_{sb}.

3.2. Characterization techniques

A set of techniques was employed for characterization of the initial materials and irradiated structures. Arrangement of the measurement instrumentation and measurement principles are discussed below.

3.2.1. Current-voltage and capacitance-voltage techniques

The standard dc current-voltage and small harmonic test signal capacitance–voltage measurement techniques were employed to verify existence of a junction and to investigate the basic characteristics. These measurements were carried out by using Keithley 6430 source-electrometer and either Fluke or QuadTech 7600B LRC-meters. Samples were investigated under dc bias voltage ranging from 0.3 to 3 V and using harmonic test signal in the frequency range from 50 Hz to 100 kHz. To examine the influence of traps, capacitance characteristics were measured by employing the serial and parallel connection circuits for the junctions under test. A photograph of the exploited instrumentation arrangement for I-V and C-V measurements is illustrated in Fig. 3.3.

Fig. 3.3. Instrumentation for I-V and C-V characterization.

3.2.2. Barrier evaluation pulsed technique

The pulsed barrier evaluation by linearly increasing voltage (BELIV) technique [53-55] was applied to determine the temporal characteristics of barrier charging and carrier generation currents within the CdS junction base region. The experimental circuitry (Fig. 3.4a) and arrangement of instrumentation (Fig. 3.4b) for implementation of the BELIV measurements consists of a generator with an adjustable output of linearly increasing voltage (LIV), a junction structure under investigation, and a load resistor connected in series. Current transients were registered using a 50 Ω external resistor or load input of the Agilent Technologies DSO6102A oscilloscope. LIV pulses with peak amplitude U_P in the range of 0.5 – 2.5 V and pulse duration of 30 – 1000 μs were applied using reverse biasing.

The BELIV technique for a reverse biased diode is based on the analysis of the changes of barrier capacitance (C_b) with linearly increasing voltage $U_{LIV}(t)=At$ pulse. The $C_b(t)$ dependence on voltage $U_{LIV}(t)$ for an abrupt junction can be described by a simple relation

$$C_b = C_{b0}(1+\frac{U_p}{U_{bi}})^{-\frac{1}{2}}, \tag{3.1}$$

where the barrier capacitance is

$$C_{b0} = \frac{\varepsilon\varepsilon_0 S}{w_0} = \left(\frac{\varepsilon\varepsilon_0 S^2 e N_D}{2U_{bi}}\right)^{\frac{1}{2}} \tag{3.2}$$

for a non-biased junction of an area S. Here ε_0, ε and e are vacuum permittivity, material dielectric permittivity, and elementary charge, respectively, U_{bi} is the built-in potential barrier,

$$w_0 = \left(\frac{2\varepsilon\varepsilon_0 U_{bi}}{e N_D}\right)^{\frac{1}{2}} \tag{3.3}$$

is the width of depletion region for the non-biased junction, and $A=U_P/\tau_{PL}$ is the ramp of the LIV pulse with peak amplitude U_P and duration τ_{PL}.

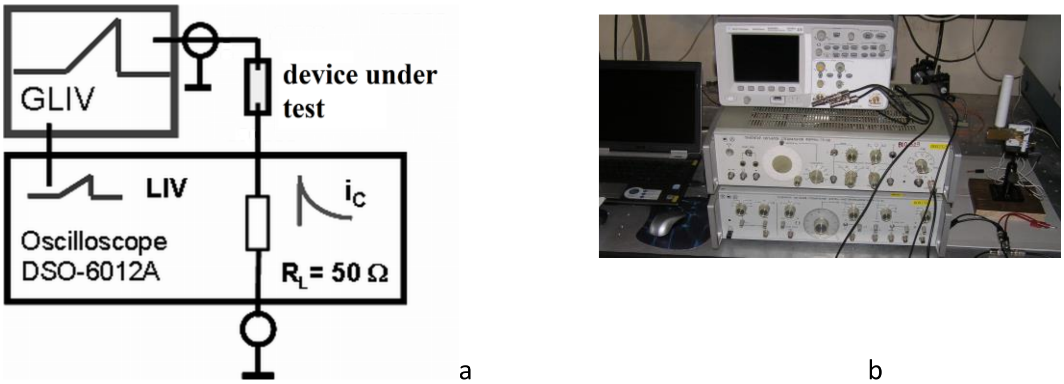

a b

Fig. 3.4. a - Sketch of the measurement circuitry for implementation of the BELIV technique. GLIV- generator of linearly increasing voltage. b - Photo of the BELIV instrumentation.

The time dependent changes of charge $q=C_bU$ within junction structure determine the current transient $i_C(t)$ in the external circuit. This transient for a rather small peak voltage U_P contains an initial (t=0) step AC_{b0} due to the displacement current and a descending component governed by charge extraction. For insulating or strongly compensated materials, this transient contains only the displacement current step [53, 55]. The descending component due to charge extraction gives an additional relation to evaluate the built-in barrier U_{bi}. Subsequently, the value of N_D is extracted by substituting the evaluated U_{bi} in the initial current expression $i_C(0)=AC_{b0}$. Carrier generation centres can be observed in BELIV current response either by the modification of the depletion width (by changing the applied electric field distribution) during the LIV pulse or by collected charge, when the increment of depletion width (bulk) highlights an impact of the generation current. For charge collection BELIV regime, the generation current is included by the increase of volume from which carriers are collected due to increased depletion width during the LIV pulse evolution. The generation current

$$i_g(t) = en_i Sw_0 \frac{(1+\frac{U_C(t)}{U_{bi}})^{1/2}}{\tau_g} \tag{3.4}$$

increases with voltage $U_C(t)$ and can exceed the barrier charging current in the rearward phase of the transient. The descending charge extraction component and the ascending generation current component imply existence of a current minimum at the time instant t_e that can be determined by using the condition $\mathrm{d}i_{R\Sigma}/\mathrm{d}t|_{te}=0$. Thus, the initial component of the composite current ($i_{R\Sigma}(t)\approx i_C(t)+i_{diff}(t)>>i_g(0)$ for $t<<t_e$) can be exploited for the evaluation of the barrier height U_{bi}.

The junction interface is clearly manifested within the BELIV transient shape and pulse amplitude. The BELIV current transient provides also additional characteristics for the evaluation of series resistance R_S of the non-depleted neutral base region and for revealing the influence of the deep centres within the high-resistivity layer. The influence of the deep traps can be deduced using either i) the appearance of a recess in the vicinity of the barrier capacitance charging peak when the trap filling process at depletion boundary ceases moving of this boundary (due to carrier extraction); or ii) the current pulse delay relatively to the LIV pulse; or iii) a BELIV current transient with a current increment within the ulterior component of the transient due to an enhancement of generation current. The increased R_S determines a significant delay (R_SC_{b0}) of the initial BELIV current peak. The impact of generation current can be controlled by monitoring the changes in the transient shape through varied pulse duration τ_{PL}. The carrier capture characteristics can be examined by using additional steady-state bias illumination to vary the filling of traps, in the case when the current peak appears to be deformed. Therefore, a broad-spectrum continuous-wave light source was exploited to perform BELIV measurements under varied intensity and spectral range of the bias illumination.

3.2.3. Deep level transient spectroscopy technique

The spectral measurements have been performed for different types of junction structures to identify specific deep traps according to their published signatures. The traditional capacitance deep level transient spectroscopy (C-DLTS) measurements were performed by using a commercial spectrometer SemiTrap DLS-82E manufactured by SemiLab, Hungary (Fig. 3.5).

Fig. 3.5. Instrumentation arrangement for DLT spectroscopy using commercial spectrometer DLS-82E.

The sample was mounted within liquid nitrogen immersion cryo-chamber. The correctness of mounting circuit and a state of electrodes was controlled by C-V measurements. Also, the C-V characteristics obtained in dark and with bias illumination are routinely employed for evaluation of the barrier capacitance and of densities of traps. Most of the Cu_2S-CdS junction structures, examined by C-DLTS, exhibited a full depletion condition even at the smallest reverse voltages. Then, a routine C-DLTS instrument and measurement regimes are non-applicable. Therefore, a steady-state bias illumination using white light LED with the emission wavelength in the range of 400-700 nm, mounted inside the cryo-chamber, has been employed. Thereby the capacitance deep level transient technique was modified by using optically induced conductivity regime [56], i.e. the C-DLTS-WL technique was implemented. Measurements of deep trap spectra have been implemented by this C-DLTS-WL regime by using the probing frequency range of 0.1-2.5 kHz. The base region of the junction (i.e. CdS layer) was then examined in Cu_2S-CdS heterojunctions. For separation of the overlapping DLTS peaks, the approximation of mono-exponential peaks close to Gaussian shape has been used, like the one included within commercial software of the DLS-82E spectrometer. The shift of simulated overlapping peaks by varying probing frequency was reproduced with sufficient accuracy in order to identify traps, published in literature. This approach had been verified on the irradiated Si junctions when DLTS spectra are complicated due to simultaneous action of several known traps.

3.2.4. Photo-ionization spectroscopy technique

To verify spectral structure of deep traps and to search peculiarities of thermally (C-DLTS-WL) and optically induced carrier transitions, the single layer (CdS) and samples with junction structures were investigated by using photo-ionization spectroscopy (PIS) technique, where either dc photo-current or barrier capacitance charging (BELIV) current is probed. The photo-ionization spectra are recorded by using the 150 W halogen lamp light source, and the spectrum is dispersed by double-way monochromator (Fig. 3.6). A sample is usually mounted in liquid nitrogen cryostat, to reduce a leakage current.

Fig. 3.6. Instrumentation arrangement for photo-ionization spectroscopy.

The photo-ionization spectra have been analyzed by using a δ - potential deep centre approach, known as Lucovsky model [57]. The red-threshold of the photo-activation energy E_{Mo}, ascribed to a deep centre M, and values of the photo-ionization cross-section σ_p have been extracted by using the Lucovsky approach, expressed as

$$\sigma_p = A_{MC}\frac{E_{Mo}{}^{1/2}(h\nu - E_{Mo})^{3/2}}{(h\nu)^3}. \tag{3.5}$$

Here, $h\nu$ is the photon energy, A_{MC} is a multiplicative factor dependent on parameters of the initial (M) and final (C) states. Excess carrier density n_{ex} generated by photo-ionization is determined by absorption coefficient $\alpha(h\nu)=\sigma_p(h\nu)n_M$, which is proportional to a density of filled traps n_M, and by surface density of the incident photons F_ν, as

$$n_{ex}(h\nu) = \alpha(h\nu)F_V = \sigma_p(h\nu)n_M F_V \tag{3.6}$$

[55, 57, 58, 59]. In a depleted diode base, the photo-generated excess carriers induce a current *i*, which is determined by carrier drift time $\tau_{dr}=d^2/\mu U_R$ and, consequently, by parameters of the elementary charge *e*, of carrier mobility μ, of junction area *S*, of base thickness *d*, and expressed as

$$i(h\nu)=\frac{en_{ex}(h\nu)S\mu U_R}{d}\,. \tag{3.7}$$

Thereby, measured values of photo-induced current represent a step-like spectrum of carriers (and of $\sigma_p(h\nu)$) photo-excited from/to definite deep levels, as F_ν is kept constant. The spectral steps are simulated and assumed to be resolvable when amplitudes of the photoresponse signals differ about two times, like in the Rayleigh’s criterion for spectral lines.

3.2.5. Microwave probed photoconductivity transient technique

Measurements of the excess carrier decay characteristics are performed by well-known pulse excitation – microwave (MW) cw probe technique. Actually, the microwave probed photoconductivity transients (MW-PCT) are examined. Light induced excess (non-equilibrium) carriers modulate reflected by semiconductor wafer MW radiation, which probes the excited region. The response *U* of MW absorption by free carriers may be presented as follows: $U=k[I_p\Delta K-I_n]$, where I_p is the intensity of the probe radiation, I_n is the intensity of noises, coefficient *k* is the transfer function of MW/electrical signal of the detector, and *K* is MW transmission function of the system: transducer-air-wafer-air-receiver, which can be described in the approach of plane waves [60, 61]. Generally, module of MW power transmission function *K* is expressed through the dielectric and magnetic permeability of the vacuum, the relative material dielectric constant including frequency dependence of the conductivity σ, where $\omega=2\pi f$ is a cyclic frequency of MW. It also depends on wafer thickness *d* and factors of the phase and amplitude modulation. The steady state transmission *K* is governed by the conductivity of material and the wafer thickness for fixed probe frequency. Its dependence on MW frequency $K(\omega)$ is a resonance-like curve similar to that of $K(\sigma_0)$. Also, the dependence of

MW response on the conductivity may be expressed via a quality factor (Q) of the waveguide system. The dependence of the factor Q on the frequency f is a characteristic of each measurement instrument. The local resonance must be achieved by slide short adjustment of the system for fixed d and σ_0 values to perform measurements in the highest sensitivity regime. A transient response of the light induced photoconductivity ($\Delta\sigma$) is determined by difference between the transmissions of the dark $\sigma=\sigma_0$ and photo-excited $\sigma=\sigma_0+\Delta\sigma$ material: $\Delta K=K(\sigma_0)-K(\sigma_0+\Delta\sigma)$. The modulation of the transmission ΔK in the range of low frequencies $\sigma>>\omega\varepsilon_r^*\varepsilon_0$ and of low phase modulation can be described in approach of plane waves [60, 61].

An important characteristic of the instrument is the linearity of the response, i.e. $U\propto\Delta\sigma\propto\Delta n$ where Δn is the excess carrier density. This condition is satisfied when $\Delta\sigma/\sigma_0<<1$ and $\Delta K/K<<1$. The decay curve is distorted (especially in the initial part of the decay) when the latter condition is invalid. The amplitude characteristic deviates from the linear one, when $\Delta\sigma$ increases with the excitation and the ratio $\Delta\sigma/\sigma_0\rightarrow 1$. The modulated transmission is expressed as

$$\Delta K=(\Delta\alpha d)^2\frac{(\mu/\varepsilon_0)}{(1+(\sqrt{}\mu_0/2\sqrt{}\varepsilon_0)\sigma_0 d)^2(1+(\sqrt{}\mu_0/2\sqrt{}\varepsilon_0)\Delta\sigma d)^2}. \qquad (3.8)$$

Due to the phase relations, the transient response may acquire either positive or negative pulse shape. It depends on both dark and light induced conductivity of the sample and relaxation time scale. To avoid stretch and other distortion effects due to the mismatch from the local resonance the arrangements for adjustment of the waveguide frequency are necessary, especially, when the surface recombination is significant. To enhance the dynamic range of the instrument the intensity of the MW probe I_p is desired to be large. The data pre-selection and statistical data processing are applied to minimize the noises I_n.

A schematic diagram of the experimental setup is presented in Fig. 3.7. Microwaves, of frequency of 21 GHz with power of 50 mW, generated by

Gunn oscillator serve as a probe source. Microwaves are radiated on the sample through the slit-shape resonant antenna. The MW detector is mounted in the receiver waveguide chamber. The generator and receiver are disjoined by the circulator.

The pulsed radiation of the microchip solid-state Nd:YAG laser (STA-01) with discrete wavelength λ of 1062 nm is used for excess carrier generation. Pulse duration is τ_L=500 ps to satisfy the approximation of δ-pulse. The diameter of the excitation spot on the wafer sample is as usually about of 100 μm. The absolute values of excess carrier concentration are controlled by the calibrated measurements of the light energy density per pulse for consideration of the nonlinear recombination processes. The errors of these measurements may exceed 10% due to the experimental uncertainties. On the other hand, the recombination parameters should be known for more precise determination of light induced carrier concentration (Δn). Thus, the absolute values of the excess carrier density Δn are obtained by the iteration procedure or by calibration measurements, if necessary. For monitoring of carrier recombination lifetimes, the relative values of this density are sufficient or even unimportant.

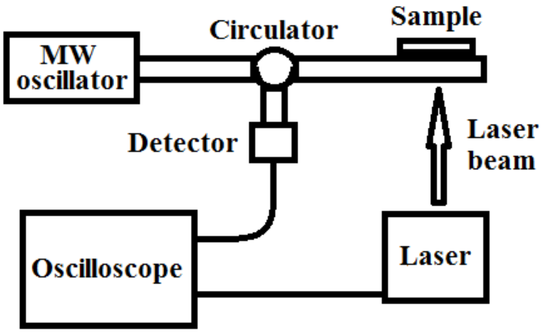

Fig. 3.7. Sketch of the MW-PCT experimental setup.

The transients of the reflected MW radiation and absolute MW-PC signal U values are recorded by a digital oscilloscope for the time-resolved MW photoconductivity measurements. The MW response is proportional to the excess carrier concentration and includes also the changes of carrier mobility via function $K(\varepsilon_r^*)$. The latter changes are usually small. The relaxation curve of MW reflection signal modulation usually has two characteristic parts: transitional non-exponential part and quasi-exponential asymptotic part, if surface recombination prevails. For irradiated samples, the recombination lifetime is significantly shorter than characteristic time of transitional component in surface recombination governed carrier decay. Therefore, the initial component is exponential in radiation defect containing samples, and it can be definitely attributed to radiation induced recombination centres. The transitional and asymptotic decay curve components may be significantly modified by the carrier trapping effects. This trapping component is characterised by instantaneous or effective lifetime (τ_{eff}) in the asymptotic part. The amplitude of this trapping component considerably depends on excitation intensity or additional bias illumination. Usually, a broad spectral band source is exploited for bias illumination in order to cover the rather wide range of the activation energies attributed to shallow trapping levels, if the dominant trapping levels are not revealed.

The simultaneous determination of the set of recombination parameters is based on the adjustment of the experimental and calculated characteristics by the least squares method using models, approximations and varying measurement regimes. The adjustment procedure is cancelled, when the absolute minimum of the functional or boundary values of the parameters are achieved. In the latter case the result (set of parameters) is used as the start data for the next iteration, and/or algorithm is extended by including an additional recombination models.

It is very important to select consistent measurement regimes and to define well the experimental conditions for the reliable carrier lifetime measurements. This includes a strict definition of the excitation level and proper adjustment of the measurement system into the local resonance. The linearity of the response U_m is found to be maintained within more than 3 orders of magnitude of laser pulse energy. The MW-PC signal might be saturated if the material nonlinear MW transfer function appears for large modulation of material conductivity at definite MW frequency. This function is always controlled. The distortion due to two-dimensional carrier diffusion may either increase or shorten the instantaneous time. The changes of carrier lifetime versus excitation intensity are often accompanied by the variation of decay curve shape even when the adjustment of the waveguide system is carefully controlled.

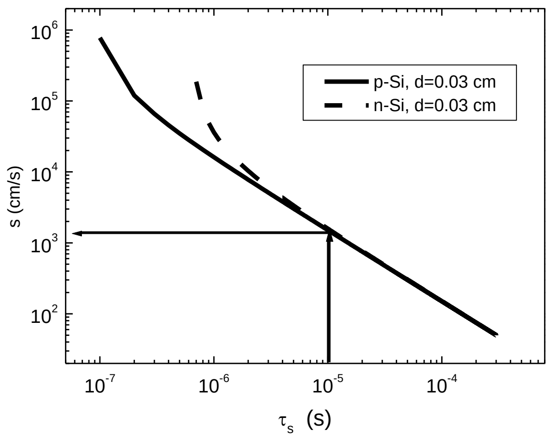

Fig. 3.8. The simulated relation between the surface recombination velocity *s* and the surface recombination time τ_S in the n- and p- Si wafer samples of thickness $d\approx300$ μm. Difference appears due to different values of carrier diffusion coefficient *D*.

In Fig. 3.8, the relation between surface recombination velocity and surface recombination time τ_S is illustrated when applied to Si material wafers. In thin non-passivated samples, the effective decay lifetime τ_{eff} ascribed to the main decay mode (for the rather thin $d<(D\tau_b)^{1/2}$ samples, where τ_b is the bulk recombination lifetime) can be approximately equated to the surface recombination component, i.e. $\tau_{eff}\approx\tau_{S}$. In this approximation, the surface recombination time τ_S is expressed through spatial frequency of the main decay mode η_1 as $\tau_S=D\eta_1^2$. The spatial frequency is obtained by solving the well-known (in semiconductor physics text-books [62]) transcendental equation for symmetric surface recombination on wafer surfaces $(s_1=s_2=s)$: $\eta_1 tg\,\eta_1 d/2=s/D$. Then, surface recombination velocity can be extracted by using equation

$$s=\frac{\sqrt{D}}{\tau_s tg(d/2\sqrt{D\tau_s})}. \tag{3.9}$$

However, the discussed approximation is only valid if $d/\sqrt{D\tau_S}\leq\pi$. Additionally, this method of *s* estimation also needs independently determined or assumed value of carrier diffusion coefficient *D*.

3.2.6. Techniques for examination of luminescence transients and spectra

The simultaneous control of the photoconductivity (ascribed to integrated over excitation beam spot area) and spectrum as well as the time resolved photoluminescence (PL) signals (associated with micro-crystalline volumes) have been chosen as a tool to resolve an impact of different layer micro-volumes on carrier decay, if electrical, spectral and temporal characteristics are ascribed to lateral inhomogeneity. The simultaneous record of MW-PC and PL responses ensures the same sampling area on the layer under investigation, as both (MW-PC and PL) signals are generated by the same UV laser excitation beam. The time resolved MW-PC and PL (also spectrally dispersed) measurements were combined with confocal microscopy imaging (CMI) to relate micro-crystallite size (from CMI) and PL efficiency (spectral) local variations.

A sketch of experimental arrangement, applied in this work for simultaneous MW-PC and spectrum as well as time resolved PL measurements is shown in Fig. 3.9.

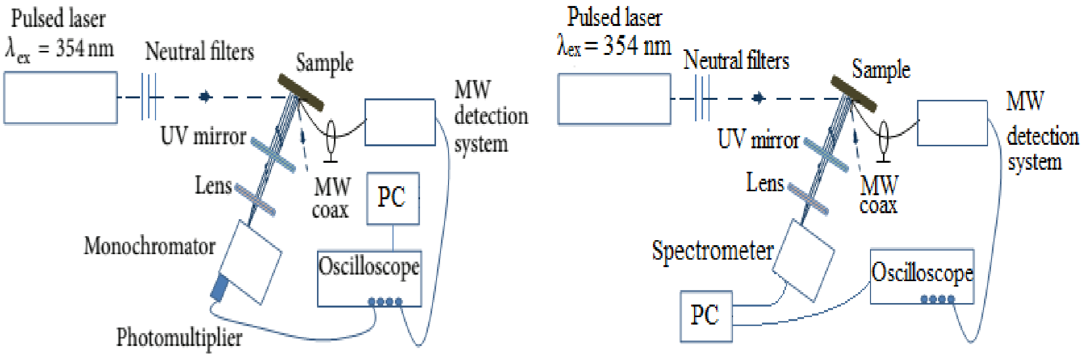

a b

Fig. 3.9. Setup of instrumentation for the simultaneous measurements of the MW-PC and PL spectrum resolved transients (a), and for *in situ* measurements of time integrated PL spectrum and MW-PC transients during proton irradiation (b).

Transient signals of the MW-PC and of PL have been synchronously collected and integrated over the same UV (354 nm) excitation beam spot. A micro-chip laser STA-1-TH was employed for pulsed (500 ps) ultraviolet (UV) light generation of the excess carriers. Intensity of excitation is varied by spectrally neutral optical filters. The MW-PC response has been detected by using a coaxial needle-tip probe [63]. The registered MW-PC signal is transferred from a microwave detector to a digital 1 GHz oscilloscope TDS-5104, equipped with computer, where MW-PC transient is displayed and processed. The PL light is collected from the area within a bisector between the incident and reflected UV light beams. The UV filtered PL beam is focused onto a slit of grating monochromator where it is dispersed. The PL pulsed signal is detected by a Hamamatsu H10721 photomultiplier. This detected PL signal is also transferred to another channel of the digital oscilloscope TDS-5104, where PL transient is displayed and processed together with MW-PC transient.

The confocal microscopy imaging has been implemented by using UV continuous-wave laser and microscope *Alpha* 300 - *WITec.* The spatial distribution of PL intensity within a fragment of area of the CdS layer was studied on a sub micrometer scale. For spectral resolution, the microscope was coupled by an optical fiber with a UHTS 300 spectrometer followed by a thermoelectrically cooled CCD camera. The excitation beam of a CW He-Cd laser emitting at 442 nm was focused onto the sample using high numerical aperture (NA=0.9) objective. This ensured that in-plane spatial resolution is approximately 220 nm.

In simultaneous measurements of PL and MW-PC transients, an UV laser beam is properly attenuated by neutral filters and directed on the sample surface for excitation of MW-PC and PL signals. The MW-PC signal is collected from the excited area by MW coaxial needle-tip antenna and registered by the MW detection system. The PL light is collected from bisector between the incident and reflected UV laser beams and filtered (by UV 100% mirror for excitation wavelength), and focused by quartz lens onto slit of the grating monochromator. The spectrally dispersed PL light transients are registered by photo-multiplier. Both signals are simultaneously recorded at different channels of digital 1 GHz band oscilloscope.

3.2.7. Instrumentation for the in situ experiments

Instrumentation for the in situ carrier lifetime control during protons irradiation has been installed and tested at facilities of proton accelerator at Division of Materials Physics of Helsinki University and at Tandem accelerator of the State Research Institute Centre for Physical Sciences and Technology, Vilnius. Defect creation processes have been examined through analysis of variations in the MW-PCT by using Vilnius University made instrument VUTEG-3 [64] for remote measurements. A sketch of experimental arrangement is shown in Fig. 3.10.

To maintain the safety requirements, the remote measurement regimes have been applied [65]. Therefore, the instrumentation contains measurement and handling components placed in a remote safe area, the constituents for signal transfer (waveguides and coaxial lines) between the irradiation chamber and the measurement instruments, and the modified irradiation chamber with vacuum inlets for cables and fibers as well as with manipulators for positioning of sample and probes.

The main measurement instrument VUTEG-3 contains a microchip laser STA-01 for pulsed photoconductivity excitation, a microwave system for probing of photoconductivity transients, an oscilloscope for measurement of signals and a computer (PC) for data processing as well as for distant control of measurement regimes and for remote positioning of probes. Excitation system is equipped with a light intensity attenuator, a telescope for laser beam shaping and with a fiber terminal for excitation beam transfer to a sample. MW probe system contains a microwave generator (22 GHz range), a microwave detector with the load matching elements, a circulator for separation of generated and reflected microwave radiation, a microwave bridge for adjustments of the microwave lines and a MW waveguide terminal to transfer the microwaves to a sample and to collect MW probe signal. A photoresponse, as an excess carrier decay transient resulted from pulsed 400 ps excitation at 1062 nm, 531 nm or 354 nm wavelengths and registered by MW detector, has been recorded by a 1 GHz Agilent Technologies DSO6102A or Tektronix TDS-5104 oscilloscope and analyzed by a PC before, during and just after proton irradiation on wafer samples. Transients during irradiation are registered every tenth millisecond. To enhance precision of measurements of the recombination lifetime reduction rates as a function of fluence, a proton beam current has been varied to set small steps in values of the collected fluence. Complementarily, the video camera (VC) was replaced by a monochromator using the same multi-fiber (fiberscope) transfer line, when it is necessary to perform simultaneous spectroscopy measurements.

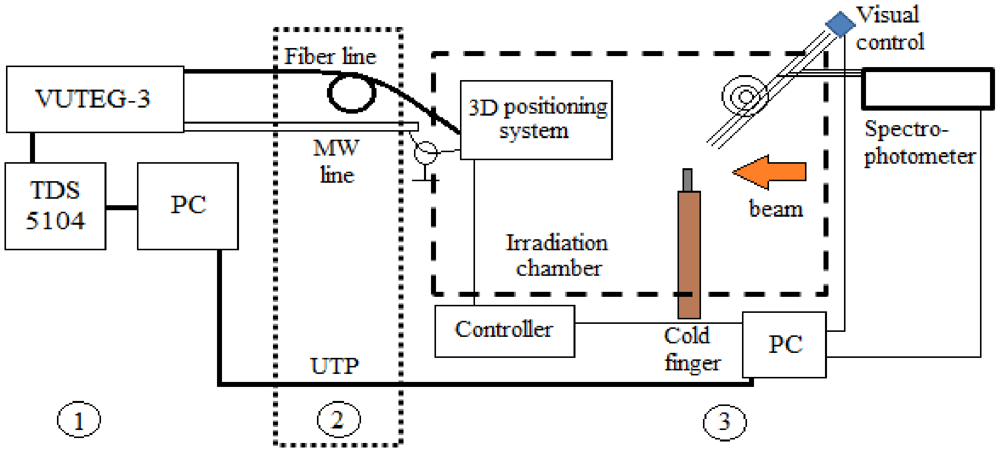

Fig. 3.10. Sketch of the setup for the remote and in situ measurements carrier recombination characteristics during irradiation by protons beam: measurement and remote handling components, constituents for distant transfer of signals, geometry of positioning of probes, of manipulators and of cable inlets for measurement circuitry inside vacuumed irradiation chamber. In the inset *i*, a screen image of probes position control (the fiber-tip and MW needle-tip antennas on wafer boundary).

Components of signal transfer at a distance of about 2 - 15 m between the irradiation chamber and the measurement instruments contain a waveguide line with low attenuation for long-distance transmission of MW radiation, a fiber line for conveyance of excitation light, the coaxial cables for transfer of video signals from VC connected to fiberscope and for electrical signals of a temperature control system (and other circuitry), for distant manipulation of step-motors installed on 3D stage on top-flange of the vacuum irradiation chamber combined with bellow system, and the twisted-pair (UTP) lines for PC aided manipulation of measurement regimes via local area network (LAN).

The excitation fiber line, the multi-fiber trunk of a fiberscope for an in-chamber video control of the positioning of the probes relatively to a sample boundary are installed into irradiation chamber via top-flange of a chamber by using vacuum connectors and are tightly attached to a 3D stage driven by step-motors. A link between a MW waveguide line and a short coaxial cable is arranged nearby the irradiation chamber to get low attenuation in transmission of MW signals. The latter MW coaxial cable is connected to a semi-rigid coaxial needle-tip MW antenna inside the irradiation chamber by using vacuum proof coaxial passage. The MW needle-tip and the excitation fiber-tip probes of dimensions of about ϕ~10 μm intersect nearby the sample boundary within a plane of wafer perpendicular to irradiation beam, while a gap between probe tips and the sample boundary is adjusted by using the probe holders attached to a 3D stage and is controlled visually through a fiberscope system (Fig. 3.10). The irradiation chamber contains two flexible bellows connected with chamber flanges. The bottom of them is designed for vertical positioning of the sample holder which can be combined with a closed cycle He cooler. The top one is combined with 3D stage positioned with precision of 3 μm by step-motors, to locate precisely position of the probes relatively to a sample boundary and proton beam. A sample placed on cold finger is moved into irradiation area of the collimated 5 mm diameter proton beam. Initially, sensitivity of a probe system to irradiation of protons of different energy in the range of 2 - 9 MeV and of beam current in the range of 0.5- 20 nA had been investigated. It was found no significant impact on probes by proton beam and negligible noises induced.

Summary of the chapter

A system of combined techniques and concerted measurements were composed to examine different type materials and samples prospective for radiation dosimetry sensor fabrication. The electrical characteristics were correlated with spectral data of deep traps measured by transient techniques to associate technological and radiation defects with density of dopants and lateral distribution of carrier traps. The non-radiative and radiative carrier decay parameters were simultaneously measured by microwave probed photoconductivity and photoluminescence techniques. A system of instruments has been composed for the remote measurements of the *in situ* variations of MW-PC transients and luminescence spectra dependent on proton irradiation fluence.

IV. Primary and post-irradiation characteristics of Si structures

4.1. Evaluation of surface recombination in SLIM detectors

To control the efficiency of surface passivation (oxide/nitride for n-type and alumina for p-type) of the cleaved sidewalls in order to put the edge of slit detector matrixes close to the active area of particle trackers and to reduce the leakage current and to increase the breakdown voltage, the more specialized technique, dedicated for extraction of surface recombination velocity has been employed. This method is based on simultaneous measurement of the amplitude of the main decay mode, which is only dependent on spatial frequency η_1 in carrier density profile of the limited thickness of sample, and of effective decay lifetime. The initial profile of the initially photo-excited carriers can be manipulated externally by varying excitation depth, dependent on the absorption coefficient α for the excitation light. The methodology of these measurements and extraction of surface recombination velocity had been developed in our laboratory [66-70].

The description of relations between the measured and the extracted parameters is based on thickness averaging of excess carrier density by microwave probe. Then carrier density variation in time t and over wafer depth coordinate x is expressed as

$$n(x,t) = n_0 \sum_{m=1}^{\infty} A_m e^{-(D\eta_m^2+1/\tau)t} \sin(\eta_m x + arctg \tfrac{D\eta_m}{s}) \quad . \qquad (4.1)$$

Here n_0 is a concentration of the light injected excess carrier pairs, A_m is a decay amplitude ascribed to the spatial frequency η_m of a decay mode m, τ is the bulk recombination lifetime, D is the coefficient of ambipolar diffusion of carriers, s is the velocity of surface recombination, for identically passivated surfaces. By averaging this concentration over wafer sample thickness d and by normalizing the photoresponse signal to its peak value, the relative signal changes in time is described as

$$\frac{< n(t) >_d}{< n(0) >_d} = \sum_{m=1}^{\infty} < A_m >_d \; e^{-(D\eta^2+1/\tau)t} \quad . \qquad (4.2)$$

The thickness averaged amplitude is then represented as

$$< A_m >_d = \frac{4\alpha d \sin\frac{\eta_m d}{2} \cos \frac{\eta_m (2x_0 - d)}{2} \{e^{-\alpha d} \sin[\eta_m (d - x_0) - Arctg(\frac{\alpha d}{\eta_m d})] + \sin[\eta_m x_0 + Arctg(\frac{\alpha d}{\eta_m d})\}}{(\eta_m d)\ (1 + e^{-\alpha d})(1 + (\frac{\alpha d}{\eta_m d})^2)(\eta_m d + \sin\ \eta_m d \cos\ \eta_m (2x_0 - d))}. \tag{4.3}$$

The spatial frequencies are obtained by solving the transcendental equations of a type

$$ctg\,\eta\ x_0 = \eta\ d\frac{D}{s_1 d};\cdots ctg\,\eta\ (d - x_0) = \eta\ d\frac{D}{s_2 d}. \tag{4.4}$$

Here, x_0 is a position within sample depth where a peak of concentration depth-distribution appears. For symmetry of surface recombination $s_1=s_2$, the expression for averaged amplitude is simplified as

$$< A_m >_d = < A_m >_{d,\alpha d=0} \frac{\alpha d/2}{1 + (\alpha d/\eta_m d)^2}(cth\frac{\alpha d}{2} + \frac{D\alpha}{s}) \tag{4.5}$$

with

$$< A_m >_{d,\alpha d=0} = \frac{8}{(\eta_m d)^2 (1 + (\frac{D}{sd})^2 (\eta_m d)^2 + 2\frac{D}{sd})}\ . \tag{4.6}$$

The effective decay time, measured in the asymptote of a transient, is then expressed as

$$\tau_{eff}{}^{-1} = \tau^{-1} + \frac{D(\eta_1 d)^2}{d^2} \tag{4.7}$$

Thereby, two equations with two parameters *s* and *D* for determination are obtained. The graphical representation (Fig. 4.1) of these relations can alternatively be employed for extraction of surface recombination velocity, when bulk recombination is a significantly longer process relative to the surface recombination.

For the reliable and separate evaluation of $A_1(\eta_1(s))$ and $\tau_{eff}(\eta_1(s),\tau)$, two excitation wavelengths, at least, are employed ($A_1(\alpha,\eta_1(s))$): for verification whether if A_1 (the main decay mode) is reached. Thereby, τ_{eff} is measured at 1062 nm A_1 is extracted at 531 nm excitation. For the more reliable evaluation of the sidewall passivation, two measurement regimes (sketched in Fig. 4.2) were additionally combined: the case, when single directional excess carrier diffusion model is sufficient to analyze surface recombination (Fig. 4.2b), and when three dimensional process should be included (Fig. 4.2a). For the one-dimensional approach, the partial filling of the slit MW antenna is implemented. Then, the near-surface range of a wafer sample is excited, and decay process (decay curve shape and components, - the amplitude and temporal parameters) is analyzed. This regime is appropriate when metallized slits and guarding rings allow impinging of excitation beams into the sample. The three-dimensional regime appears: diffusion into the sample bulk (semi-infinite geometry) and surface recombination within thickness of wafer, if excitation is performed through the sidewall. In the latter experimental geometry, three surfaces act as the carrier sinks, which can increase the rate of integral surface recombination, included via additional exponential term within expression for carrier density temporal variations.

A comparison of transients recorded on non-passivated and passivated the same material wafer samples at slim boundary are illustrated in Figs. 4.3a and b.

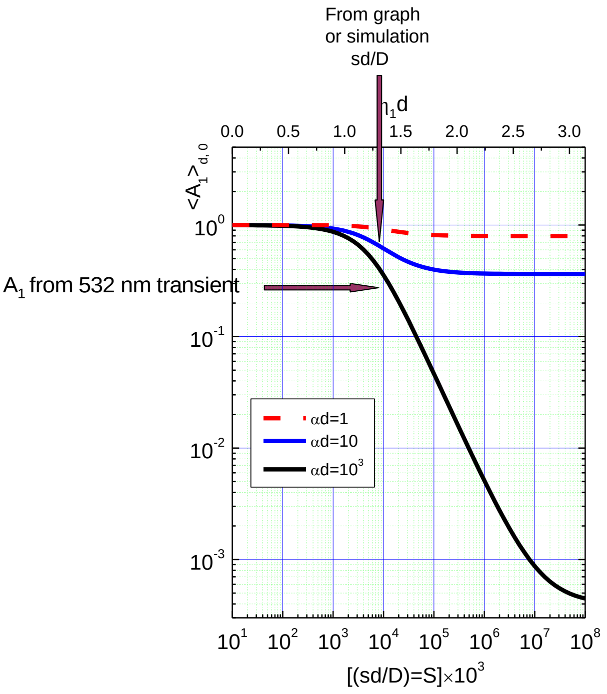

Fig. 4.1. Graph for extraction of surface recombination velocity using the measured amplitude of the main decay mode by varying excitation depth for bulk $\alpha d \leq 1$ and the near surface $\alpha d > 10$ excitation wavelengths.

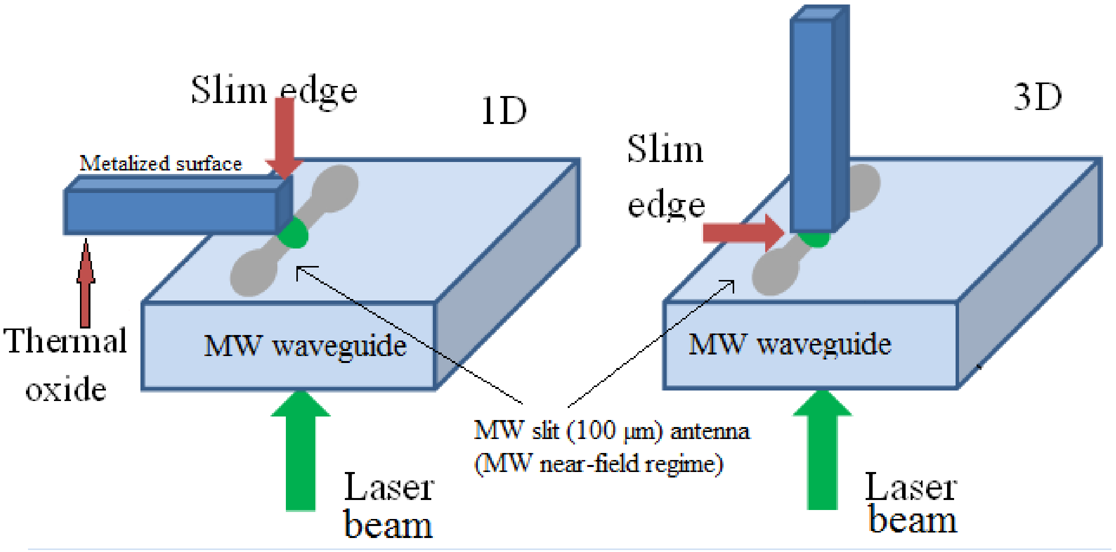

a b

Fig. 4.2. Sketches of the experiments for measurements of surface recombination velocity in situations when three-dimensional diffusion process should be analysed (a) and when one-dimensional approach is sufficient for analysis (b).

In the comparison, the inherent features of the carrier decays under bulk and near surface excitation can be deduced. The first one is an equality of decay rates in the asymptote of a decay of the non-passivated sample, Fig. 4.3a (the parallel decay fragments are observed for both transients in the asymptote at bulk and near surface excitation). The second feature would be a clear decrease of the amplitude ascribed to the main decay mode for the near surface excitation regime relative to the bulk one. This leads to a clear two-componential decay curve for the near surface excitation regime, while for bulk excitation regime a quasi-single–exponential transient is observed. The parallel shift of the asymptotic components (Fig. 4.3a) proves the prevalence of the surface recombination, and the intersection of the slopes of these components with the ordinate axis denotes the amplitudes of the main decay modes $\langle A_1\rangle_d$ ascribed to the bulk $\alpha d=0.03$ and the near surface $\alpha d=2.4\times10^2$ excitation regimes. Then the surface recombination velocity can be evaluated graphically e.g. from the simulated graphs of type shown in Fig. 4.1. In the passivated sample (Fig. 4.3b), reduction of the amplitude $\langle A_1\rangle_d$ attributed to the near-surface (αd=2.4×10^2) regimes is considerably less than that for non-passivated sample. This is a clear indication of sidewall passivation using alumina covering applied to p-type Si material.

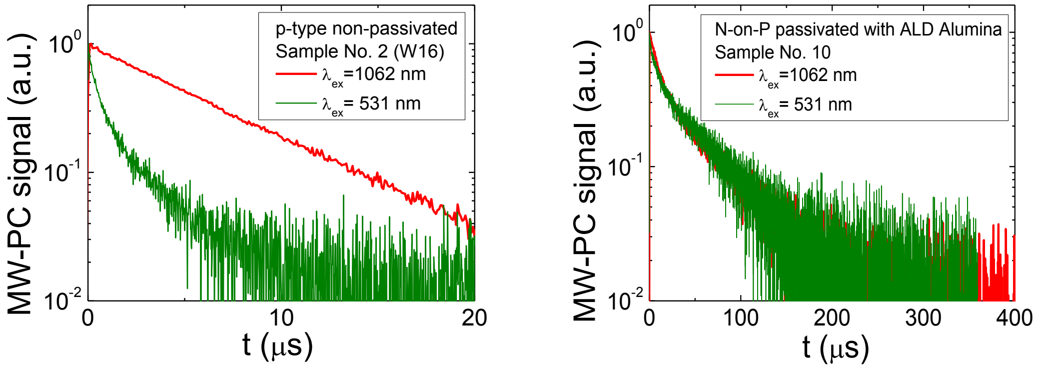

a b

Fig. 4.3. Microwave probed photoconductivity transients measured for bulk (red curves) and near surface (green curves) excitation using 1062 nm and 531 nm light laser pulses, respectively, in non-passivated (a) and alumina passivated (b) sidewall surfaces.

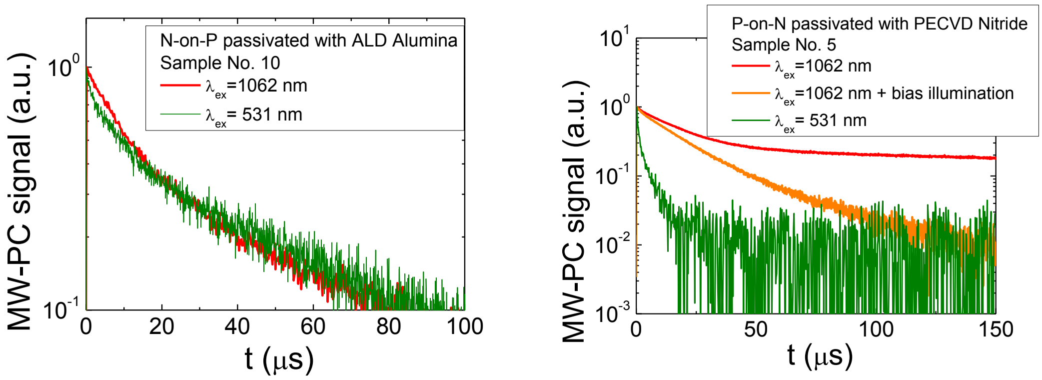

Fig. 4.4. Microwave probed photoconductivity transients measured for bulk (red curves - without additional cw bias-illumination and orange curves - with additional cw bias-illumination) and near surface (green curves) excitation using 1062 nm and 531 nm light laser pulses, respectively. Here, the MW-PC transients obtained for different passivation layers, exploited for different conductivity type Si material, are illustrated. Additional bias illumination serves for suppression of trapping effect.

The similar changes of the MW-PC transients have been obtained in the case of three-dimensional measurement regime, as illustrated in Figs. 4.4. However, the trapping effect, i.e. concerted action of surface recombination and trapping centres, has been observed when excess carriers are able to change a filling of the surface traps, when excitation is performed directly of sidewall boundary. To verify whether it is really a trapping effect, the additional bias (cw-steady-state) illumination has been applied using broad spectral range light together with pulsed laser beam excitation. The decrease of the amplitude of the asymptotic component under bias illumination (suppression of trapping by the bias illumination) is a clear indication of existence of trapping effect, i.e. competition of deep (recombination) and shallow (trapping) centres.

Table 4.1. Values of the surface recombination velocity and of the effective decay lifetime in samples of different conductivity, of surface passivation method and state compared with those obtained for non-irradiated and proton irradiated devices.

Sample notification Wafer, No.	$\tau_{R,eff}$ (μs)	τ_{tr} (μs)	s (cm/s)
p-type detector , p-Si, non-passivated, non-irradiated			
W18, No. 3	8	33	9.3×10^{3}
W16, No. 2	6	-	1.9×10^{4}
W16, No. 3	9	62	9.3×10^{3}
ATLAS Φ7 No.3	6	-	1.9×10^{4}
ATLAS Φ7 No.5	9	-	1.9×10^{4}
p-type (N-on-P) detector , p-Si, passivated with ALD Alumina, non-irradiated			
8	11	50	560
9	12	64	560
10	15	55	330
11	11	51	370
12	11	62	560
n-type detector , n-Si, non-passivated, non-irradiated			
2	9	610	1.9×10^{4}
3	17	110	1.4×10^{4}
n-type detector (P-on-N), n-Si, passivated with PECVD nitride, non-irradiated			
5	6	480	9.3×10^{3}
6	18	270	4.7×10^{3}
7	18	270	4.7×10^{3}
Irradiated			
Sample notification Wafer, No.	Fluence (neq, cm^{-2})	$\tau_{R,eff}$ (μs)	
B1P6	0.95×10^{13}	0.700	-
B2P10	5.78×10^{13}	0.130	-
B2P8	4.82×10^{14}	0.013	-
B2P3	3.98×10^{15}	0.001	-

Extraction of the parameter of the surface recombination velocity (rate of the carrier supply to the surface) is then implemented for suppressed trapping effect (saturation of the amplitude of the asymptotic component under increase of bias illumination intensity). The extracted values of effective decay lifetime and of surface recombination velocity are presented in the Table 4.1.

It can be deduced from the Table 4.1 that efficient surface passivation has been obtained for p-type sample sidewalls using ALD technology with alumina layers. The less efficient surface passivation appeared in n-type Si using the PECVD technology by formation of nitride layers. The single exponential transients with effective decay lifetimes τ_{eff} independent on excitation wavelength were obtained for the irradiated samples. Only a significant reduction of the τ_{eff} values with enhancement of irradiation fluence was determined. This is a clear indication that bulk recombination process prevails over the surface recombination one, when density of radiation defects becomes high. Therefore, a hypothesis of possible surface passivation [34] by sign inversion of the conductivity type in the heavily irradiated materials becomes susceptible. Also, the higher efficiency of surface passivation [67] by using thermal oxidation technology for surface passivation of n-type Si (with $s \approx 200$ cm/s values) can be implied, relative to that of Si_3N_4.

The results of the study of surface passivation can be summarized as follows: i) passivation of surfaces is rather efficient, - obtained better for p-Si (ALD alumina) than p-Si (PECVD nitride) and n-Si (PECVD nitride or traditional SiO_2); ii) There are a lot of trapping centres at the interface within passivating layer, - extremely long instantaneous lifetimes of trapping in 3D measurement geometry relative to 1D (using this more reliable extraction model) experiment geometry. This trapping effect can efficiently be suppressed by steady-state cw bias illumination; iii) Passivation is rather reproducible, - values of s in different samples vary not more than 2 times; iv) The impact of surface recombination in the irradiated samples is negligible. While, for samples irradiated with fluence $<10^{14}$ neq/cm^2, a weak change of τ_{eff} in 3D geometry relative to that of 1D can be suspected.

4.2. Anneal and fluence dependent carrier lifetime in 26 GeV proton irradiated Si

The aim of these measurements was to perform the tentative calibration measurements for fast and non-invasive dosimetry of irradiation fluence, based on excess carrier lifetime in Si dependence on collected hadron irradiation fluence. Measurements were performed using a tentative instrument VUTEG-5-AIDA fabricated at Vilnius University within 8.3 work-package of the FP7 project AIDA. This study was made on the as-irradiated FZ and CZ Si wafer fragments (described in Section 3.2) of n- and p-type conductivity material and rapidly annealed these samples (kept in de-activation storage area) just after irradiation with 26 GeV protons, to avoid transforms of the radiation defects.

The bulk excitation regime using 1062 nm wavelength pulses was implemented. Validity of mono-exponential decay is identified by analysis of decay curve shape and its invariance/variation type on excitation density, wavelength etc., on the irradiated samples only. Actually, in pure, high resistivity Si samples containing small densities of grown-in traps, the hadrons induced radiation defects become dominating for fluences $\Phi \geq 10^{12}$ cm^{-2}. However, for the smaller irradiation fluences, radiation defects compete with other recombination centres.

Another specific situation, often met in the experiments on irradiated and annealed samples, is the trapping effect. This effect is commonly caused by competition of deep recombination centres (often due to extended defects with large cross-section) and shallow carrier capture centres (those specifically participate in exchange of carriers only with nearest band due to asymmetry of electron and hole capture cross-sections). For rather large initial excess carrier densities $n_{ex}(t=0)$, these deep and shallow levels can share carrier capture flows. Shallow traps may accumulate detectable concentration of trapped carriers, as the characteristic carrier capture ($\tau_{sh,\,C}$) /emission lifetime ($\tau_{sh,\,E}$) is considerably longer for shallow traps than that (τ_R) for deep centres. Thus the main killers of the band excess carriers are deep recombination centres those rapidly diminish density of excess carrier pairs. However, density of trapped carriers on shallow traps approaches to that of free excess carriers, in the asymptotic decay phase. Then, the recombination flow through deep centres is mainly determined by carriers de-trapped from shallow levels. This leads to the non-exponential process, described by relation

$$U(t) \sim n_{ex}(t=0)\exp[-t/\tau_{i,tr}(t)], \tag{4.8}$$

with instantaneous trapping moderated recombination lifetime:

$$\tau_{i,tr}(t, n_{ex}(t)) \cong \tau_R\,[1+(\tau_{sh,E}(t)/\tau_{sh,C}(t))]. \tag{4.9}$$

Roughly, carrier decay transients are similar to a two-componential decay (inherent for surface recombination using the regime of near surface excitation), with long tail. Enhancement of excitation density hides the impact of trapping effect. Alternatively cw bias illumination balances capture/emission on shallow traps and suppresses trapping effect. Symptomatically, the MW-PC transients become mono-exponential when bias steady-state illumination (implemented, for instance, by a halogen lamp) of sufficient intensity is applied.

The carrier lifetime variations obtained in the as-irradiated samples are plotted as a function of irradiation fluence, using the double logarithm scales in Fig. 4.5. These dependencies are compared with those obtained after isothermal annealing at 80 C using different heat treatment exposure times.

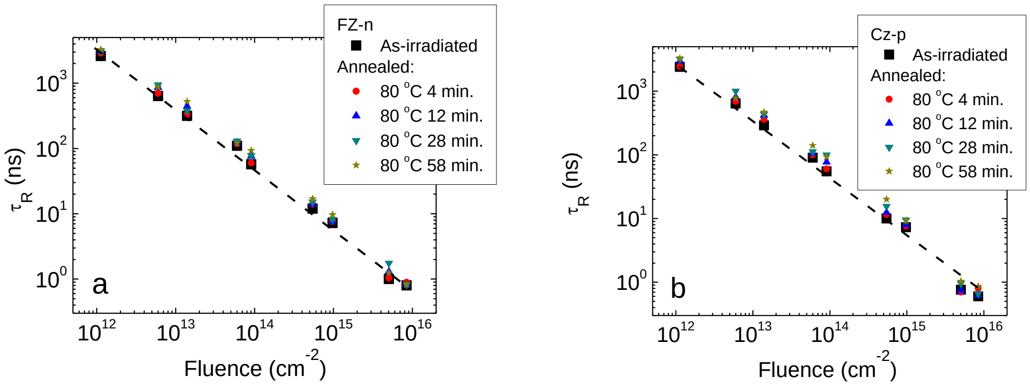

Fig. 4.5. Carrier lifetime variations (black symbols) as a function of irradiation fluence obtained in the as-irradiated samples of n-type (a) and p-type (b). Color symbols represent carrier recombination lifetime values obtained after isothermal annealing at 80 C for different durations. Here are denoted the heat treatment total durations in the legends.

It can be inferred (from Fig. 4.5) that carrier lifetime decreases near linearly with enhancement of irradiation fluence in the employed scale, irrespective of wafer fabrication technology and material conductivity type. The absolute values of τ_R are close in both n- and p-type investigated materials at fixed irradiation fluence. Such observations imply that extended defects dominate in determination of recombination lifetime values. The tetra- and penta-vacancies are revealed within EPR spectra measured by Q and W band spectrometers in MCZ the same geometry Si samples irradiated with neutron fluences >10^{15} cm^{-2}. It seems as if the structure of the prevailing extended defects serving as the dominant recombination centres is invariable, while density of such extended defects increases proportionally to fluence of irradiation. The same range of τ_R values and the linear $\tau_R^{-1}\sim\Phi$ relation obtained on different technology Si samples using different type high energy hadrons, shown in Fig. 4.6 [71], corroborate an assumption of dominant extended defects, acting as the main killers of excess carriers.

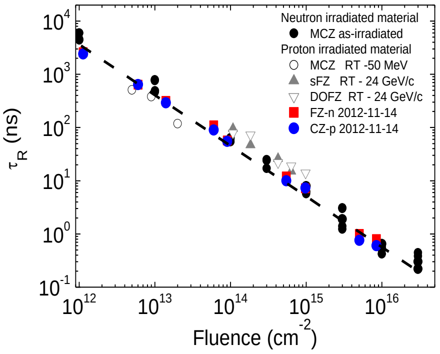

Fig. 4.6. Carrier lifetime as a function of irradiation fluence obtained in the as-irradiated Si samples of different technology using different hadron irradiations. Color symbols represent carrier recombination lifetime values obtained on the samples of this study [71].

The employed heat treatments lead to rather resolvable (on the plots in Fig. 4.5) slight increase (relatively to a wide range $\log\tau_R^{-1}\sim\log\Phi$ line) of carrier lifetime after annealing. This result is in agreement with our previous observations on neutron irradiated samples [71]. The isochronal annealing for temperature range from 80^0 C to a 380^0 C induced an increase in carrier trapping lifetime (Fig. 4.7). These variations are the most significant for the range of irradiation fluences close to 10^{14} cm^{-2}.

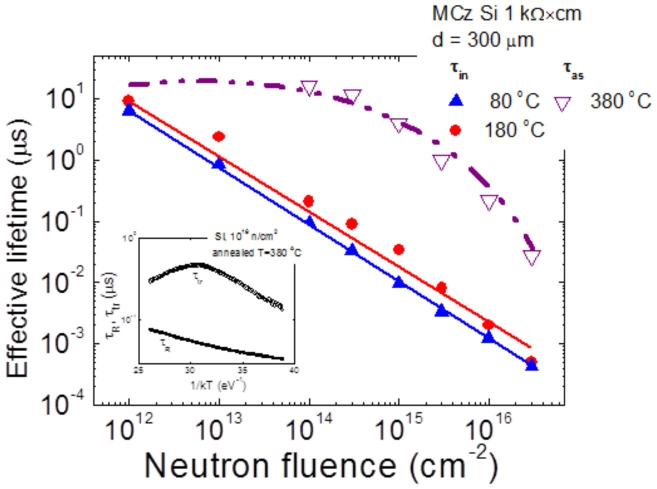

Fig. 4.7. Variations of the effective decay lifetimes in the as-irradiated and annealed Si samples. In the inset, trapping and recombination lifetime dependencies on temperature are illustrated.

The density of the re-arranged radiation defects thus increases with enhancement of thermal activation energy (kT_{annel}). These density changes have been evaluated by modelling the experimentally observed ratio of the carrier recombination (τ_R) and instantaneous trapping (τ_i) lifetime assuming the same dominant trapping E_T and recombination E_R centres, acting together. The MathCad modelled changes of instantaneous carrier trapping lifetime are illustrated in the insets of Fig. 4.8. From these simulated instantaneous trapping lifetimes, the density of trapping centres created by anneal, due to transforms of radiation defects, are illustrated in Fig. 4.8 as a function of neutron irradiation fluence. In can be deduced from Fig. 4.8 that transforms of large fluence introduced defects can be inefficient if heat treatment temperature is insufficient (<380^0 C). The density of the transformed trapping centres saturates for the largest temperatures employed for anneals.

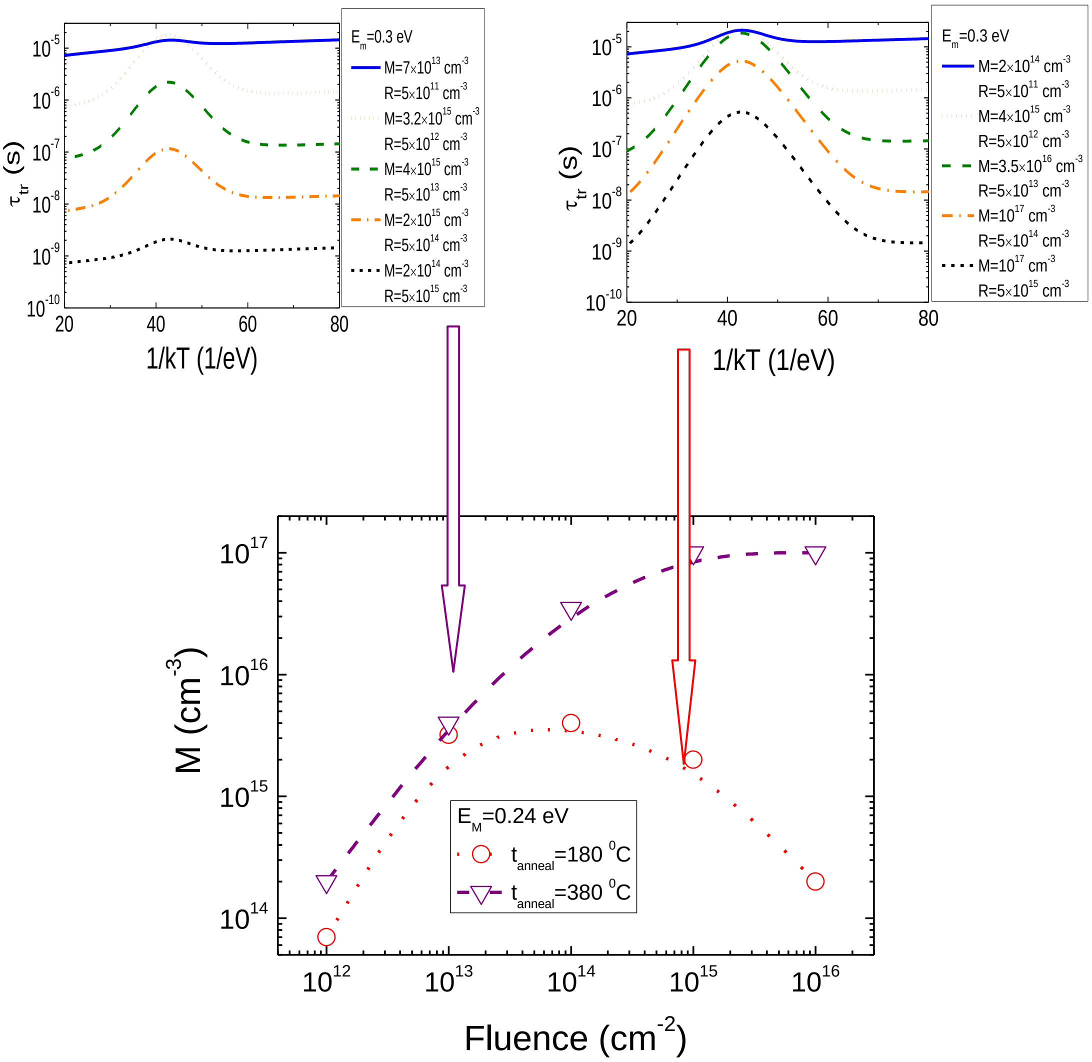

Fig. 4.8. Variations of the density of trapping centres transformed by post-irradiation heat treatment as a function of irradiation fluence, evaluated for neutron irradiated and isochronally (4 h) annealed Si samples in the temperature range from 80^0 C to 380^0 C. In the insets, illustrations of the changes of trapping lifetime for dominant E_M=0.24 eV trapping centres extracted by fitting experimental ratios of recombination (τ_R) and instantaneous trapping (τ_i) lifetimes

To highlight the lifetime variations induced by isothermal (80^0 C) annealing (as in the double logarithm scale shown in Fig. 4.5), the semilog log τ_R~t_{exp} dependences for different fluences are compared in Fig. 4.9. These linear τ_R~$t_{exp,\ anneal}$ dependencies are separately re-plotted in Fig. 4.10, as obtained on fixed fluence irradiated Si samples of n- and p- type investigated material. In the more resolvable scale, Fig. 4.10, variations of lifetime values are scattered. This can be explained by imprecise positioning of the MW-antenna at the centre of wafer tetragon, after each heat treatment step, and inhomogeneity of irradiation beam location on the wafer fragment. Therefore, an additional positioning stage has been performed in the improvements of the VUTEG-5-AIDA instrument. Also, the precise temperature control, within sample compartment of VUTEG-5-AIDA instrument during lifetime measurement, is foreseen in further upgrade of this dosimeter. The obtained deviations in lifetime values after several anneal steps do not exceed the changes of lifetime values measured in the centre and periphery of wafer pieces investigated.

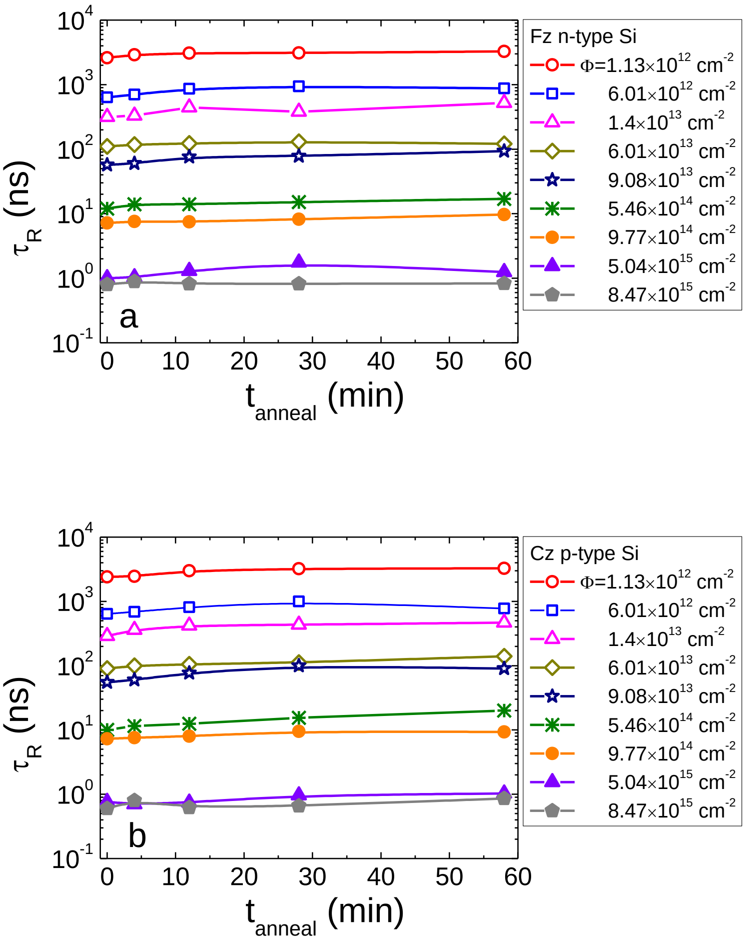

Fig. 4.9. Carrier lifetime as a function of the total annealing exposure time obtained in Si samples of different conductivity n-Si (a) and p-Si (b) type as well as fabrication technology: FZ (a) and Cz (b), respectively, irradiated by different fluences.

The observed increase in carrier recombination lifetime under heat treatments would be favourable technique to restore heavily irradiated particle detectors. In this study, the observed changes of extracted carrier lifetime values can be also influenced by carrier trapping effect. In several MW-PC transients, measured after a few of heat treatment steps, appearance of trapping inherent longer tail was indicated. Additional steady–state bias illumination by halogen lamp was able only slightly modify the appeared trapping induced decay tail. Therefore, installation of the more intense bias illumination source is foreseen in future improvements of the dosimeter.

Appearance of trapping effect can be explained by anneal induced transforms of radiation point defects. Re-arrangement of extended defects is hardly possible by rather low temperature anneals, however, density of definite type point defects is very probable and clearly proved in DLTS spectra of the same type Si material, even under rather low temperature and short duration heat treatments. These point defects usually provide shallower levels in the forbidden gap relatively to those deep (close to mid-gap) traps ascribed to extended radiation defects.

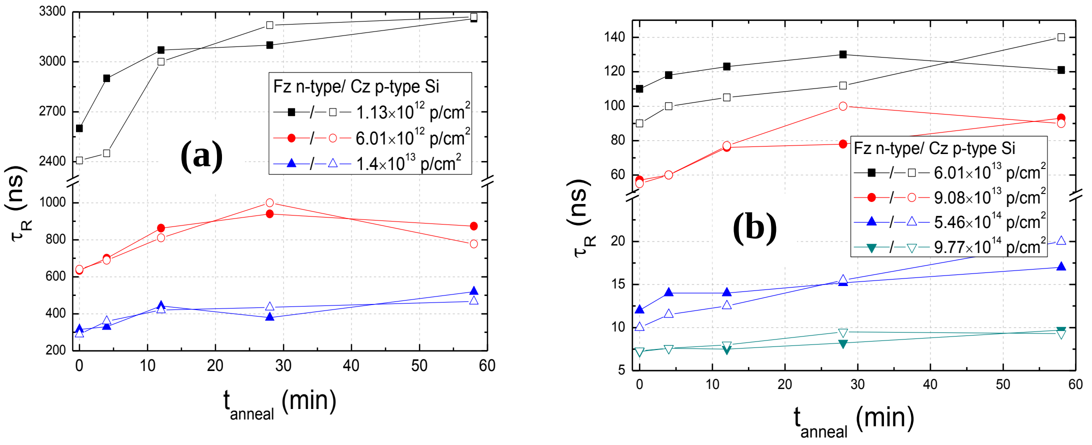

Fig. 4.10. Carrier lifetime as a function of the total annealing exposure time in linear scale obtained in Si samples of different (FZ and Cz) technology and conductivity

type (n- and p- Si) irradiated by fixed fluences in the range of moderate (a) and elevated (b) values .

In summary, the carried out study devoted to calibration of VUTEG-5-AIDA instrument confirmed the contactless MW-PC technique for dosimetry of the just irradiated Si wafer fragments. The obtained carrier recombination lifetime values fit the close to linear relation between hadrons irradiation fluence and excess carrier lifetime. For creation of the precise calibration curve of $\tau_R \sim \Phi$, further research is inevitable to clarify the main factors, as temperature in sample compartment during measurements, storage temperature and heat treatment history of Si samples, impact of the competition between point and extended defects leading to trapping effect. Therefore, an additional positioning stage, precise temperature control, within sample compartment of VUTEG-5-AIDA instrument during lifetime measurement, and installation of the more intense bias illumination source are foreseen in further upgrade of this dosimeter.

4.3. Spectroscopy of point trapping centres induced by hadron irradiation

The high energy radiation detectors, designed for the particle tracking and dosimetry, suffer the un-acceptable radiation damage after irradiations with large fluences, $>10^{14}$ cm^{-2}. To predict the operational characteristics of such devices, the density and types of radiation defects, evolution of extended defects and agglomeration of point defects with enhancement of collected fluence, an impact of these defects on the detector characteristics should be comprehensively examined.

The standard methods, such as capacitance deep level transient spectroscopy (C-DLTS) [72] and thermally stimulated current (TSC) [73] techniques are un-applicable for analysis of the heavily irradiated devices. In this work, therefore, several steady-state and pulsed techniques have been combined to comprehensively evaluate parameters of radiation defects and functional characteristics of the irradiated Si pin detectors. To clarify the prevailing radiation defects and to search their evolution the C-DLTS and TSC techniques have been employed to make a baseline identification of the radiation induced traps after irradiation with rather small fluence 10^{12} cm^{-2}. The steady-state PIS technique [74] has been involved to correlate thermal- and photo- activation energies for definite radiation defects. A contactless technique for simultaneous measurements of the carrier lifetime and the parameters of deep levels based on microwave probed pulsed photo-conductivity (MW-PC) spectroscopy [75] have been applied to correlate carrier capture cross-sections and densities of the identified different radiation defects. A technique for spectroscopy of deep levels in junction structures (BELIV) [76] based on measurements of generation current transient changes with temperature has been applied to evaluate activation energy of dominant deep traps in the irradiated diodes. Pulsed PIS spectroscopic [75, 77] measurements were implemented by combining the analysis of excess carrier densities, of current and of barrier capacitance charging transients modified by a single fs pulse of illumination generated by an optical parametric oscillator with output wavelength in the range from 0.5 to 10 μm. Several deep levels in the range of 0.18 - 0.80 eV have been resolved from spectral analysis in the samples of Si grown by MCZ technology.

The TSC experimental procedure consists of cooling the sample down to a low temperature where filling of the traps is performed (by illumination or forward biasing of the diode). The TSC current measurements are then performed during heating up (with a constant heating rate of 10 K/min) under reverse bias applied to a diode. The active volume of the sample is well controlled, when full depletion regime is maintained during a temperature scan, and thus the defect concentrations can be calculated from the total charge released from the defects during the heating (peaks appear in the TSC spectra).

For measurements of barrier capacitance charging and generation currents, modified by either temperature [76] or photo-ionization quantum energy [77], a pin diode is placed on a sample holder in a cryo-chamber and connected with electrodes by coaxial cable to the external measurement circuitry. The BELIV technique [76, 77], using a reverse biasing regime, is based on the analysis of the barrier capacitance (C_b) and generation current (i_g) changes with the linearly increased voltage ($U=At$) pulse. Current transients have been registered using a 50 Ω load input of the DSO6012A oscilloscope. The measurement circuitry contains an adjusted output of a generator of linearly (with time t) increasing voltage and a diode under investigation, connected in series. Also, spectroscopy of deep levels in junction structures by using BELIV technique, based on measurements of generation current transient changes with temperature for different duration LIV pulses, has been applied to evaluate activation energy of the dominant deep traps in the irradiated diodes.

The PIS spectral measurements have been also performed by registering the steady–state current changes at reverse bias, close to a full depletion regime in the investigated Si diodes. The photo-ionization spectra were recorded by using the halogen lamp light source and a monochromator DMR-4. A sample is usually mounted in liquid nitrogen cryostat, to reduce a leakage current. The photo-ionization spectra have been analyzed by using a δ-potential deep centre approach, known as Lucovsky model [58]. The red-threshold of the photo-activation energy E_{Mo}, ascribed to a deep centre M, and values of the photo-ionization cross-section σ_p have been extracted by using the Lucovsky approach, expressed as in (3.5).

Photo-ionization spectra measured on the same samples by using short pulse excitation regime and by controlling either barrier capacitance [77] (BELIV on diode structures) or photoconductivity [75] (probed by microwaves on wafer samples) changes when varying excitation wavelength have been correlated with steady-state PIS spectra to evaluate role of the carrier capture and deep level filling effects. Pulsed spectroscopic measurements had been implemented by combining the analysis of excess carrier densities, of generation current and of barrier capacitance charging transients modified by a single fs pulse of illumination generated by an optical parametric oscillator with output wavelength in the range from 0.5 to 10 μm.

The DLTS spectra obtained for MCZ n-Si diode irradiated with 10^{12} n/cm^2 fluence recorded varying rate window are illustrated in Fig. 4.11a. An oxygen-vacancy (VO) ascribed carrier trap (~95 K), a double-charged di-vacancy ($V_2^{=/}$, ~125 K) and single charged ($V_2^{-/0}$, ~225 K) di-vacancy associated traps have been identified. Enhancement of irradiation fluence above 10^{12} n/cm^2 leads to an increase of traps density over that of dopants. Therefore, free carriers associated with dopants are captured, and the base region becomes fully depleted even without reverse bias, making standard DLTS technique non-operational. The TSC spectrum recorded for the same n-Si base diode, irradiated with 10^{12} n/cm^2 fluence, illustrated in figure 4.11b, corroborates dominance of V-O and di-vacancy associated radiation defects.

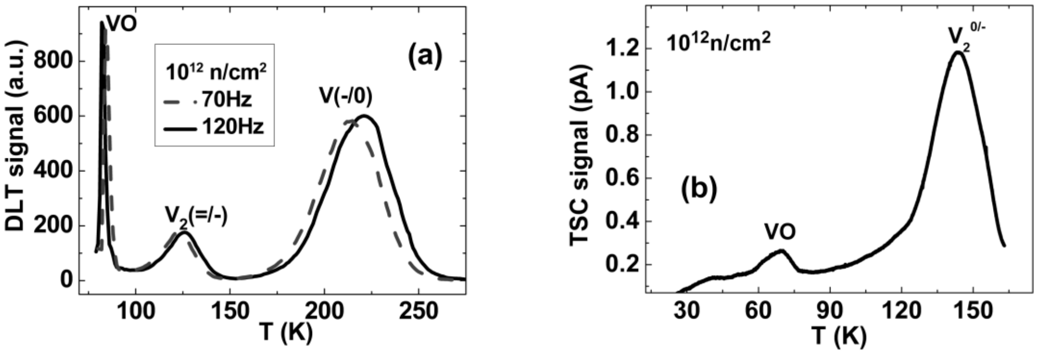

Fig. 4.11. DLTS spectra (a) and TSC spectrum (b) obtained for MCZ n-Si diode irradiated with 10^{12} n/cm^2 fluence.

To track an evolution of deep levels spectrum structure and to evaluate their density, different modifications of photo-ionization spectroscopy were involved. The steady-state photo-ionization spectra recorded on the Si diodes irradiated with neutrons of different fluences are illustrated in Fig. 4.12a. These spectra allow the separation of red-threshold photo-activation energy of different spectral steps. Thin lines in Fig.4.12a correspond to the fitted spectra using Lucovsky model. Extracted E_{Mo} values are denoted on fitted spectral steps in Fig. 4.12a. Several PIS spectral steps (Fig. 4.12a) have been resolved within steady-state current variations with excitation light spectrum. The first spectral step E_{Mo1}=0.41 eV can be ascribed to direct photo-activation of filled single-charged di-vacancy levels. The second one, $E_{Mo2}=E_V+E_M$=0.77 eV, is associated with photoexcitation of electrons from valence band to primary emptied $V_2^{-/0}$ levels, as, in the fully depleted diode base, there is no carriers able to fill the traps. Thereby, PIS measurements confirm prevailing of the $V_2^{-/0}$ traps in 10^{12} n/cm^2 fluence irradiated diodes, in agreement with DLTS spectra recorded for the same diode. Halogen lamp infra-red light source was insufficient to induce recordable current, ascribed to the shallower $V_2^{=/-}$ and VO levels within PIS spectra.

To increase spectral resolution of deep traps, the pulsed PIS technique has been employed by using a single fs pulse of the spectrally bright illumination generated by an optical parametric oscillator (OPO). The probing technique of the MW-PC transients has been applied for wafer samples. Fluence dependent variations of photoconductivity probed PIS spectra steps are shown in Fig. 4.12b. Also, changes of MW-PC amplitudes, directly representing density of photo-ionized carriers and ascribed to the peaks attributed to different deep levels, are shown as a function of neutron fluence in the inset of Fig. 4.12b. The presented MW-PC PIS signal characteristics indicate an increase of the density of traps and formation of deeper traps with enhancement of irradiation fluence.

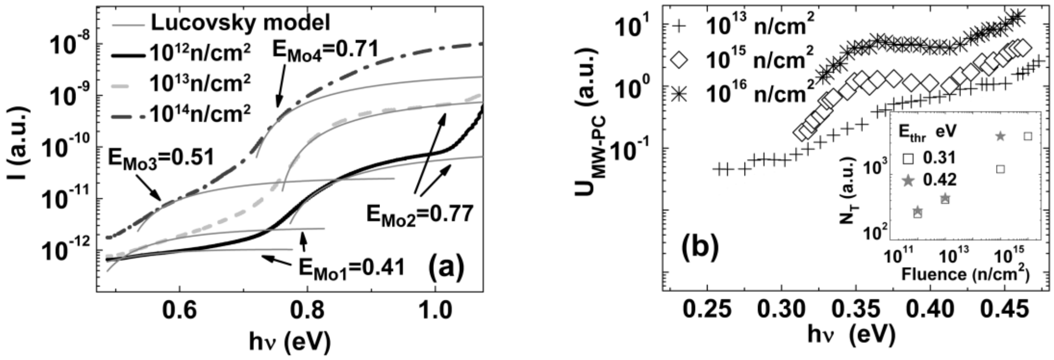

Fig. 4.12. PIS spectra recorded by changes of steady-state photo-current (a) and pulsed MW-PC transient signals (b) obtained for MCZ n-Si diodes (a) and wafer samples (b) irradiated with different fluences.

To correlate variations of deep level spectrum structure changes, dependent on irradiation fluence, the BELIV probed PIS spectra were examined. By varying the wavelength of the OPO pulsed illumination and by controlling of barrier capacitance charging current peak, a PIS spectrum of deep levels is obtained and shown in Fig. 4.13a. Here, the barrier capacitance dependence on excitation quantum energy represents PIS spectrum peaks. The obtained DLTS spectra (Fig. 4.11a) actually corroborated the existence of a set of deep traps characterized by activation energies equal to those extracted from the BELIV-PIS spectroscopy measurements. Restoration of the barrier capacitance charging peak and dominance of the barrier charging current in the pulsed illuminated diode is observed when the density of deep traps is smaller than that of dopants. Prevailing of the generation current within BELIV transients has been observed in Si pin detectors irradiated with elevated fluences of reactor neutrons ($\Phi>10^{13}$ n/cm^2). To evaluate activation energy of deep traps, responsible for generation current, temperature dependent variations of the BELIV transients in the heavily irradiated diodes were examined. These characteristics are illustrated in Fig. 4.13b. It can be noticed in Fig. 4.13b, that activation energy of the filled traps, prevailing in formation of generation current at 500 μs LIV pulses, increases with enhancement of neutron fluence. This result is in agreement with modelling of the deep levels filling, when several traps of high concentration compete in capture of free carriers of low density [14].

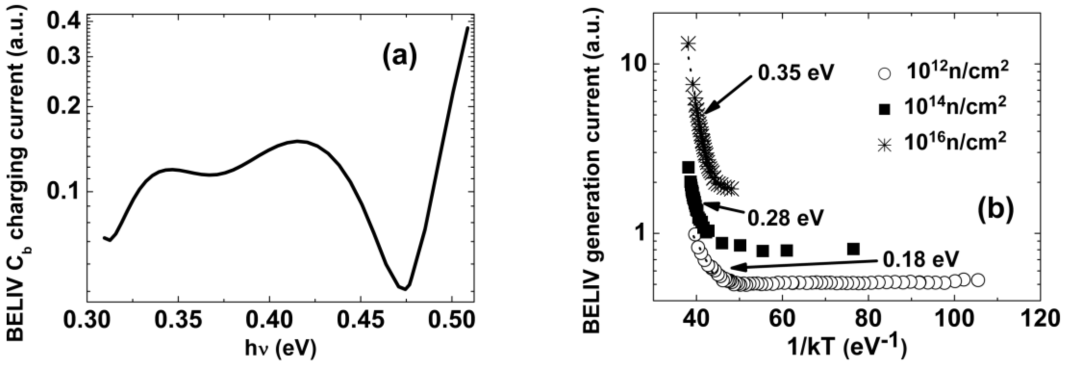

Fig. 4.13. a - Deep level spectra measured by control of barrier capacitance charging current peak changes under pulsed OPO light pulse excitation in Si pin detector structures irradiated with 10^{13} n/cm^2 neutrons fluence. b - Generation current temperature variations extracted from BELIV transients.

It can be inferred that carrier recombination processes determine the dielectric relaxation time within electrically neutral region (ENR) of a base of diode and time scale of stabilization of depletion width. On the other hand, carrier capture/emission processes within space charge (SC) and transition layer (between ENR and SC) regions impact the generation/recombination currents in a diode. The observed decrement of carrier recombination lifetime ascribed to different PIS steps, revealed by MW-PC spectral changes, leads to the reduction of equilibrium carrier density within ENR and to increase of a generation current, due to emission of these captured carriers within SC region.

Summary of the chapter

[A3, A4, A10, P3, P6, P7, P9, P12]

The study of surface passivation on Si strip detectors with slim edges enabled to come to such main results: i) passivation of surfaces is rather reproducible and efficient, nevertheless, it is obtained better for p-Si (ALD alumina) than n-Si (PECVD nitride); ii) There are a lot of trapping centres at the interface within passivating layer; iii) The impact of surface recombination in the irradiated samples is negligible.

The verified carrier recombination lifetime values fit the close to linear relation between hadrons irradiation fluence and excess carrier lifetime. Storage temperature and heat treatment history of the Si samples, impact of the competition between point and extended defects leading to trapping effect.

Several photo-ionization spectral steps have been resolved and identified, - namely, step E_{Mo1} =0.41 eV can be ascribed to direct photo-activation of filled single-charged di-vacancy levels; spectral step at $E_{Mo2}=E_V+E_M$=0.77 eV is associated with photoexcitation of electrons from valence band to primary emptied $V_2^{-/0}$ levels. PIS measurements confirmed the prevailing of the $V_2^{-/0}$ traps in 10^{12} n/cm^2 fluence irradiated diodes, in agreement with DLTS spectra recorded for the same diode. These traps mainly act as carrier trapping centres with a rather long de-trapping time.

V. Characteristics of Cu_2S/CdS structures

5.1. Characterization of Cu_2S-CdS hetero-junctions

A BELIV technique [14, 76] was applied to determine the temporal characteristics of the junction barrier charging and carrier generation currents within CdS junction base region. These results are discussed in more detail in [78], while the main features are summarized below.

Three types of BELIV transients (Fig. 5.1), associated with CdS polycrystalline formation regimes, have been obtained in dark over sets of the investigated Cu_2S-CdS samples. The square-wave shape BELIV transients are inherent for the I-type samples, which were deposited at T_{dep}=220 C of substrate temperature for t_{dep}=60 min. These I-type BELIV transients imply the insulator-specific state of base material, which lacks of free carriers. The II-type and III-type samples are similar, as exhibiting the junction, which depletion can be modified by external voltage. The main difference (respectively to the electrical characteristics of these II- and III-type samples) appears in generation current. For the II-type samples (T_{dep}=260 C, t_{dep}=75 min), the generation current component is pronounced within the rearward wing of transient due to carrier emission from deep traps. For the III-type samples (T_{dep}=260 C, t_{dep}=80 min), the barrier charging current peak prevails which is accompanied with the descending current component due to charge extraction. The observed differences over the BELIV transient shapes were explained [78] assuming variation of relative densities of dopants (which form shallow levels) and carrier capture centres (associated with rather deep levels). Value of free carrier density of the $n_0=1.5\times10^{13}$ cm^{-3} was estimated for junctions of II- and III-type, and it determines concentration of shallow traps. For the I-type samples, a geometrical capacitance C_g can be only evaluated, which was found to be C_g=3 nF, and this C_g value is in agreement with that value calculated using the independently measured thickness d and probed area S of CdS layer. The $Cu_{1.96}S$, $Cu_{1.92}S$, $Cu_{1.81}S$ and other modifications together with Cu_2S were detected by XRD spectroscopy. The XRD spectrum richest in different phase precipitates was obtained in the samples of the I-type [78].

Additionally, the capacitance deep level transient spectroscopy technique modified by using optically induced conductivity regime (C-DLTS-OP) and PIS were applied to identify traps in CdS layer. It was found that the I-type junction samples contain the richest structure of traps with different photo-ionization activation energies. The II-type and III-type samples exhibit two-three step structure of the measured PIS spectrum. The C-DLTS-OP spectra can be recorded only in the samples of II- and III-type. There, only traps of the majority carriers have been distinguished within samples of the II- and III-types.

5.2. Spectroscopy of deep traps

The spectral measurements have been performed for different types of junction structures to identify specific deep traps according to their published signatures. As revealed from BELIV characteristics, most of the Cu_2S-CdS junction structures exhibited full depletion condition even at the smallest reverse voltages, a steady-state bias illumination using white light LED with emission wavelength in the range of 400-700 nm, mounted inside the cryo-chamber, has been employed. Thereby the capacitance deep level transient technique is modified by using optically induced conductivity regime [56], i.e. the C-DLTS-WL technique is implemented in the latter measurements. Measurements of deep trap spectra have been implemented for the probing frequency range of 0.1-2.5 kHz. The base region of the junction (i.e. CdS layer) is then examined. For separation of the overlapping DLTS peaks, the approximation of mono-exponential peaks close to Gaussian shape has been used, like that installed within commercial software of the DLS-82E spectrometer. The shift of simulated overlapping peaks by varying probing frequency is reproduced right enough to identify traps, published in literature. This approach had been verified on Si junctions when DLTS spectra are complicated due to simultaneous action of several known traps.

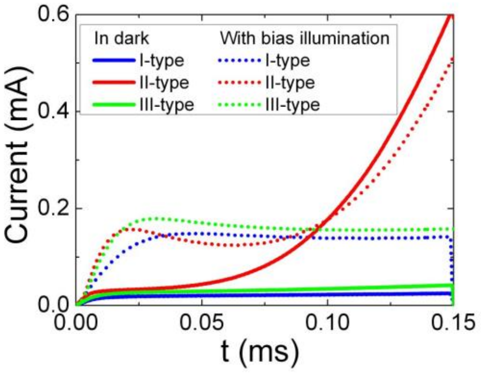

Fig. 5.1. The typical BELIV transients observed in different type Cu_2S-CdS junction structures without (solid curves) and with steady-state wide spectral band illumination (dot curves) by applying the linearly increasing voltage pulse with 1.2 V amplitude at reverse polarity.

The blocking junction of Cu_2S-CdS for majority carriers has been qualitatively tested by varying polarity of the applied voltage and by measurements of pulsed barrier charging current transients induced by linearly increasing voltage (BELIV [53, 76]). The inherent shapes for the reverse biased BELIV transients (Fig. 5.1) indicate that the high resistivity layer exists in the n-type conductivity CdS. The initial peak (Fig. 5.1) of the barrier capacitance charging current is inherent for the reverse biased junction followed by the descending current component due to charge extraction determined reduction of barrier capacitance when depletion width increases with voltage during a LIV pulse.

Three types of BELIV transients, associated with CdS polycrystalline properties, have been obtained over the sets of Cu_2S-CdS samples investigated in dark. The square-wave shape BELIV transients are inherent for the I-type samples. These I-type BELIV transients imply the insulator-specific state of base material, which lacks of free carriers. For the II-type samples, the generation current component is pronounced within the rearward wing of transient due to carrier emission from deep traps. For the III-type samples, the barrier charging current peak prevails which is accompanied with the descending current component due to charge extraction. For steady illuminated samples of type-II and type-III, barrier capacitance increases relatively to that value measured in dark. This observation indicates a recovery of the junction under steady-state illumination. For the illuminated structure, the initial barrier capacitance charging current decreases with enhancement of reverse voltage due to widening of depleted layer. However, the thermal emission current, which increases due to traps within enhanced depleted volume, becomes prevailing within rearward wing of BELIV pulse. This indicates that all the investigated junction types exhibit wide spectrum of defects acting as carrier capture/generation centres. Presence of high density of carrier generation centres is additionally confirmed by differences in C-V characteristics. The observed differences over the BELIV transient shapes were explained [53, 76] assuming variation of relative densities of dopants (which form shallow levels) and carrier capture centres (associated with deep levels). Value of free carrier density of the n_0=1.5×10^{13} cm^{-3} is estimated for junctions of II- and III-type, and it determines concentration of shallow traps. For the I-type samples, a geometrical capacitance C_g can be only evaluated, which was found to be C_g =3 nF, and this C_g value is in agreement with independently measured thickness d and probed area S of CdS layer.

Intensity of the white LED was insufficient to get measurable DLTS signal on samples of I-type, containing the smallest equilibrium carrier density and exhibiting the capacitor-like BELIV and C-V characteristics. For the samples containing the II-type and the III-type junctions, the white light of LED illumination induces a stationary domain of the excess carriers those make a virtual cathode, and, thus, enables measurements of barrier capacitance changes due to carrier thermal emission from deep levels. The C-DLTS-WL spectra obtained on samples of the II- and III-type are shown in Fig. 5.2.

For the samples of II-type (Fig. 5.2a), four overlapping peaks (Fig. 5.2c) can be resolved. To identify prevailing traps, the experimentally measured spectra were simulated by Gaussian shape curves, like as in [79], to extract the DLTS signatures. It can be noticed that peaks at 138 K, at 157 K, at 183 K and at 225 K comprise a temperature scanned DLTS spectrum. The shifts of these peaks under varied lock-in amplifier frequency in the range of 1.5-2.5 kHz are in good agreement with predictable peak variations within routine DLTS spectroscopy. The range of DLTS signal filtering frequencies implies rather fast carrier emission times in samples of the II-type.

A more complicated DLTS-WL spectrum appears for samples of the III-type (Fig. 5.2b). There, peaks associated with majority (at 205 K, at 232 K, and at 255 K) carrier traps are present. A shift of these peaks with varied filtering frequency is also observable. However, thermal emission lifetimes in samples of the III-type are a little bit longer than those deduced from the peak shifts in samples of the II-type. The DLTS signatures are again extracted after the simulated peaks are fitted to the experimental ones for majority carrier traps.

The Arrhenius plots (Fig. 5.2d) using DLS-82E software have been made using the data obtained for variations of each peak temperature position ascribed to filtering frequency. Then, activation energy values have been extracted and listed in Table 5.1. Peaks from E_1 to E_4 were associated with electron traps according to literature data [80-85] published for polycrystalline CdS. Also, DLTS peaks were analyzed using literature data for crystalline CdS and correlated with those for polycrystalline CdS.

The photo-ionization spectra measured for all the separated types of samples are shown in Fig. 5.3. These spectra were recorded at room (solid blue line) and liquid nitrogen (dash green line) temperatures. It can be noticed, that the BELIV separated types of samples are corroborated by different structure of the PIS spectra. Namely, the I-type junction samples contain the richest structure of traps with different photo-ionization activation energies (Fig. 5.3a), and, at least, three steps can be easily distinguished using Lucovsky approach. The II-type samples (Fig. 5.3b) exhibit two-three step structure of the measured PIS spectrum. Also two-three PIS peaks can be resolved within spectrum of the III-type samples (Fig. 5.3c). Position of steps within each PIS spectrum is listed in Table 5.2. Activation energy values have been extracted on the basis of the fitted PIS steps by varying the red-threshold values within simulated electron-photon cross-section spectral variation curves. The obtained values of activation energy are listed in Table 5.2. The red–threshold activation energy values, extracted using Lucovsky model, are also denoted in Fig. 5.3.

Leakage current, due to simultaneous thermal emission from different traps, increases significantly a pedestal of the PIS signal. Therefore, extraction of the activation energy for deep traps is more reliable using those PIS measured at 77 K temperature. While the existence of these peaks is clearly confirmed within PIS spectra measured at room temperature. Also, low temperature measurements are preferential, as an impact of the phonon-electron interactions are efficiently reduced with decrease of temperature.

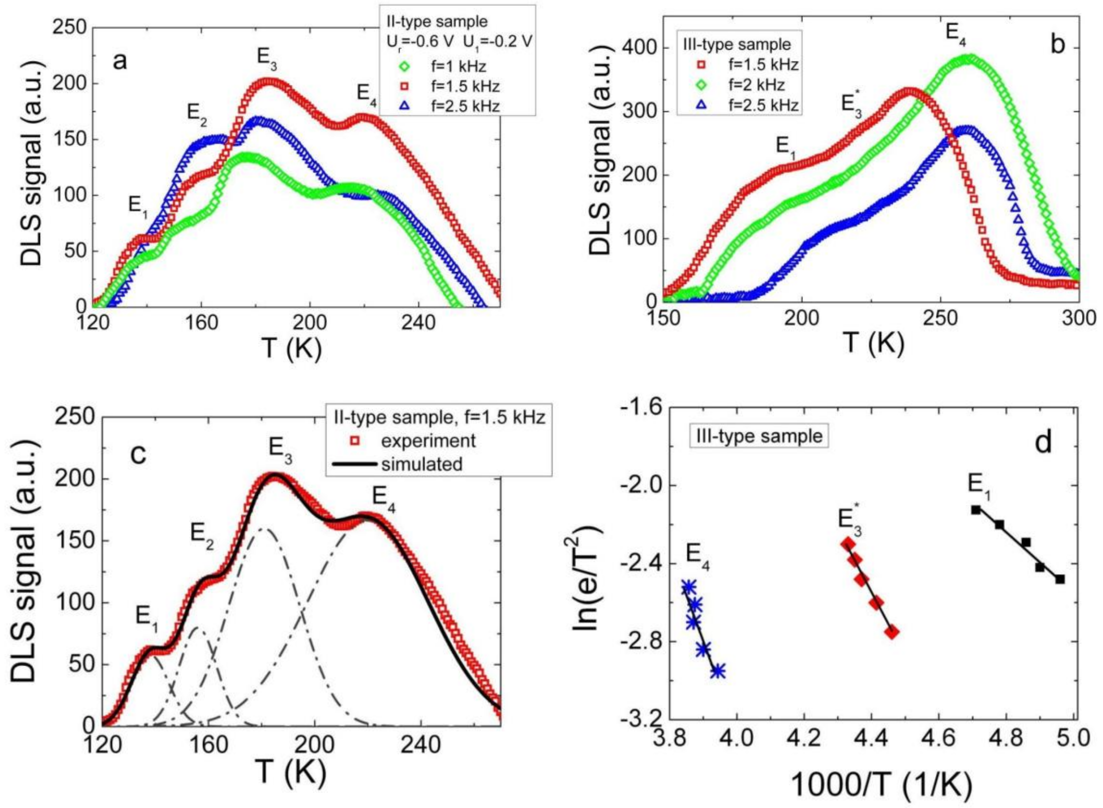

Fig. 5.2. C-DLTS-WL spectra obtained on samples of the II- (a) and III-type (b) of Cu_2S-CdS junction samples, as measured at 0.6 V reverse bias voltage using temperature scan regime for lock-in frequencies range from 400 to 2500 Hz. c - Simulated spectrum of sample of type-II. d - Arrhenius plots for III-type sample.

Table 5.1. DLTS peaks obtained within spectra of different type samples.

Type of samples	Temperature at which DLTS peak is observed (K)	Energy of thermal activation of trap obtained from Arrhenius plot (eV)	Origin of the trap, reference
II-type	138	E_1=0.15±0.01	electrons- trap in polycrystalline CdS [81, 84]
	157	E_2=0.22±0.02	electrons- trap in polycrystalline CdS [83, 85]
	183	E_3=0.26±0.02	electrons- trap in polycrystalline CdS [84]
	225	E_4=0.40±0.02	electrons- trap in polycrystalline CdS [81]
III-type	205	E_1=0.13±0.01	electrons- trap in polycrystalline CdS [81]
	232	E_3^*=0.31±0.02	electrons- trap in polycrystalline CdS [81, 84]
	255	E_4=0.4±0.02	electrons- trap in polycrystalline CdS [81]

The combined analysis of the extracted values of DLTS and PIS peaks has been performed keeping in mind that DLTS represents directly thermal activation energy while photo-ionization transitions are probable only from the filled to the empty levels. The correlated values of activation energies for thermal and photo-emission of carrier transitions are presented in Table 5.3.

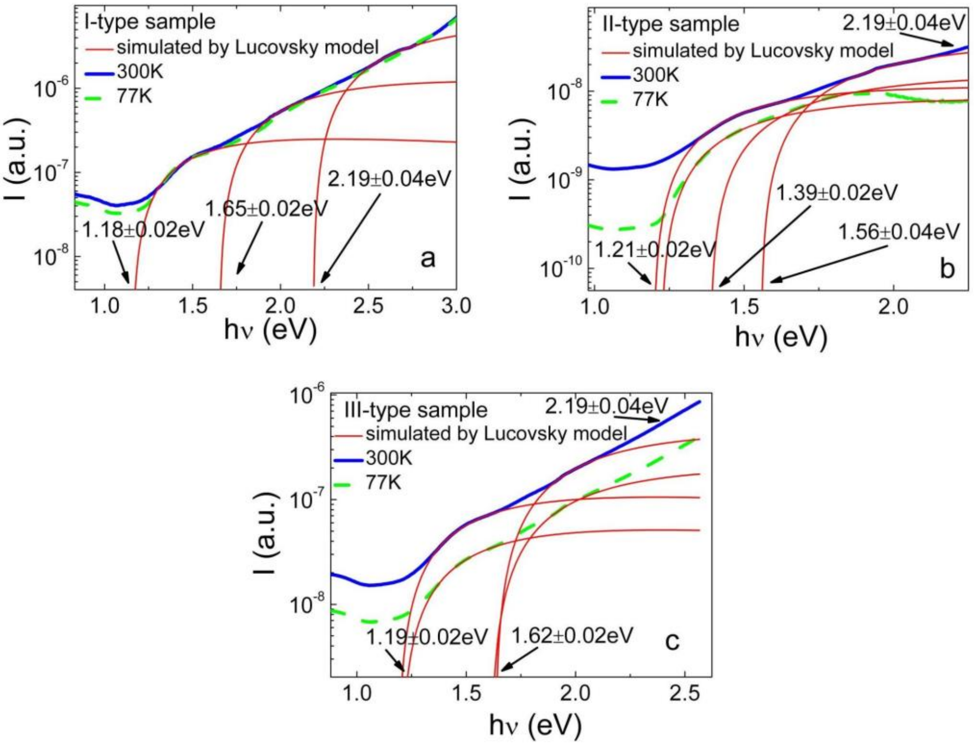

Fig. 5.3. Photo-ionization spectra obtained on the I-type (a), on the II-type (b), and on the III-type (c) of Cu_2S-CdS junction samples, as measured at 0.5 V bias voltage and at two different temperatures: at room (solid blue line) as well as at liquid nitrogen (dash green line). Thin red lines represent the simulated by Lucovsky model PIS steps fitted to the experimental spectrum.

Table 5.2. PIS peaks obtained within spectra of different type samples.

Type of samples	Photon energy at which PIS peak is observed (eV)	Energy of photo-activation of trap extracted by using Lucovsky approach (eV)
I-type	1.4	1.17±0.02
	1.8	1.65±0.02
	2.5	2.19±0.04
II-type	1.3	1.21±0.02
	1.9-2.0	1.56±0.04
	2.5	2.19±0.04
III-type	1.3	1.19±0.02
	2.0	1.62±0.02
	2.5	2.19±0.04

Shallow levels identified by DLTS spectroscopy, were not observable in PIS spectra, as PIS steps are hidden by absorption edge transitions for enhanced energy photons. Coincidence of DLTS and PIS activation energy has been obtained only for the level with activation energy E=0.34±0.04 eV. Trap with such activation energy is ascribed in literature [80-86] to Cu impurities in CdS polycrystalline material. Deeper levels with activation energy of 0.9 and 1.34 eV, identified by PIS measurements and observed in all the separated types of samples, can be associated with electron and hole traps, known as recombination centres in CdS crystals [86].

Table 5.3. Correlation of PIS peaks with DLTS peaks obtained within spectra of different type samples.

Type of samples	Thermal activation energy (eV)	Energy of photo-activation of trap (eV)	Balance of activation energies for E_g(300K)= 2.53 eV	Origin of the trap	Refs.
I-type		1.17±0.02	1.34±0.02	electrons-trap, recombination centre	[86]
		1.65±0.02	0.90±0.02	holes-trap, Cu impurities associated	[80]
		2.19±0.04	0.34±0.04	Cu impurities associated; electrons-trap in polycrystalline CdS	[80] [81, 84]
II-type		1.21±0.02	1.31±0.02	electrons-trap, recombination centre	[86]
		1.56±0.04	1.0±0.04	holes-trap, Cu impurities associated	[80]
	0.26- 0.40	2.19±0.04	0.34±0.04	holes-trap, Cu impurities associated; electrons-trap in polycrystalline CdS	[80] [81, 84]
III-type		1.19±0.02	1.34±0.02	electrons-trap, recombination centre	[86]
		1.62±0.02	0.90±0.02	holes-trap, Cu impurities associated	[80]
	0.31±0.02	2.19±0.04	0.34±0.04	holes-trap, Cu impurities associated; electrons-trap in polycrystalline CdS	[80] [81, 84]

In summary of spectral measurements, the I-type junction samples, having the smallest free carrier densities and the largest concentration of traps, as deduced from BELIV transients, contain the richest structure of traps with different photo-ionization activation energies. The II-type and III-type samples exhibit two-three step structure of the measured PIS spectrum. The C-DLTS-WL spectra can be recorded only in the samples of II- and III-type. There, only traps of the majority carriers have been distinguished in DLTS. The same level with activation energy E=0.34±0.04 eV has been identified by DLTS and PIS measurements. Trap with such activation energy is ascribed to Cu impurities in CdS polycrystalline material. Deeper levels with activation energy of 0.9 and 1.34 eV, identified by PIS measurements and observed in all the separated types of samples, can be associated with carrier traps, known as recombination centres in CdS material. The combined examination of deep traps modified characteristics, by using barrier capacitance charging current, thermal- and photo-ionization spectroscopy techniques, appeared to be sufficient to separate the different sample types formed by slightly different layer deposition conditions.

5.3. Steady-state photoluminescence spectra and confocal microscopy images

The steady-state UV excitation induced photoluminescence spectra and microscopy images obtained on CdS samples of the I-type, the II-type, and the III-type are illustrated in Figs. 5.4, 5.5, and 5.6, respectively. These confocal microscopy investigations were performed by Dr. D. Dobrovolskas. Two bands of photoluminescence have been observed within all types of samples, namely, a narrower band of green luminescence (G-PL) with a peak at 500 nm and a wider band of red luminescence (R-PL) with a peak at 700 nm, Figs. 5.4-5.6. It can be noticed, however, that the absolute values of PL intensity and a ratio between the green PL to the red PL intensities differ significantly, when comparing PL spectra for samples of these three types.

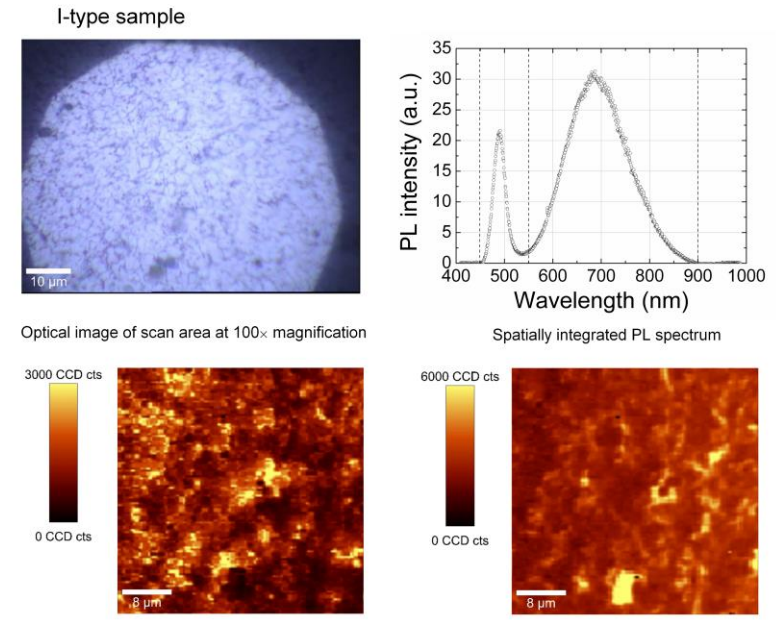

Optical image of scan area at 100× magnification

Spatially integrated PL spectrum

Fig. 5.4. Optical field microscopy image (top-left), a PL spectrum integrated over inspected area (top-right), the topographs of the distribution of the green-light luminescence (bottom-left) and of the red-light luminescence (bottom-right) panels, respectively, recorded for the CdS sample of the I-type.

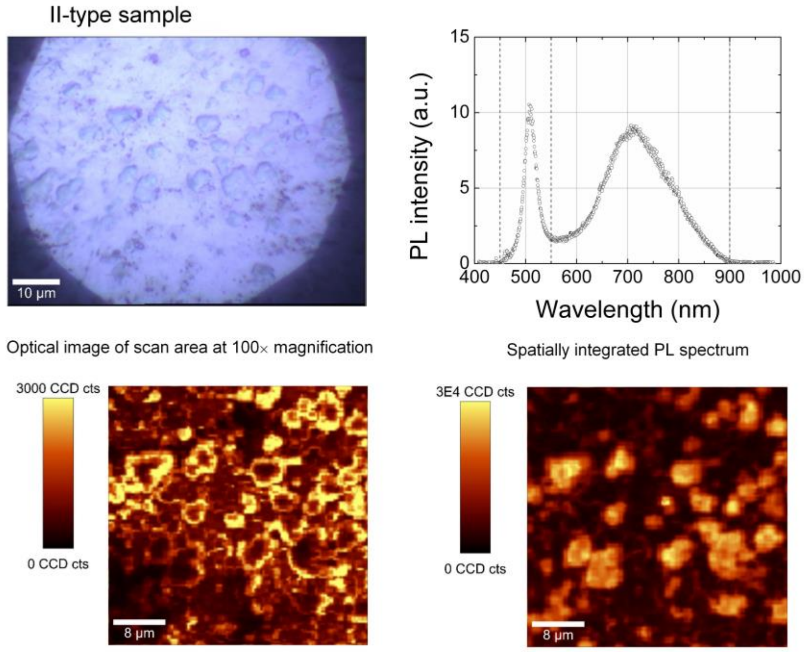

Optical image of scan area at 100× magnification

Spatially integrated PL spectrum

Fig. 5.5. Optical field microscopy image (top-left), a PL spectrum integrated over inspected area (top-right), the topographs of the distribution of the green-light luminescence (bottom-left) and of the red-light luminescence (bottom-right) panels, respectively, recorded on the CdS sample of the II-type.

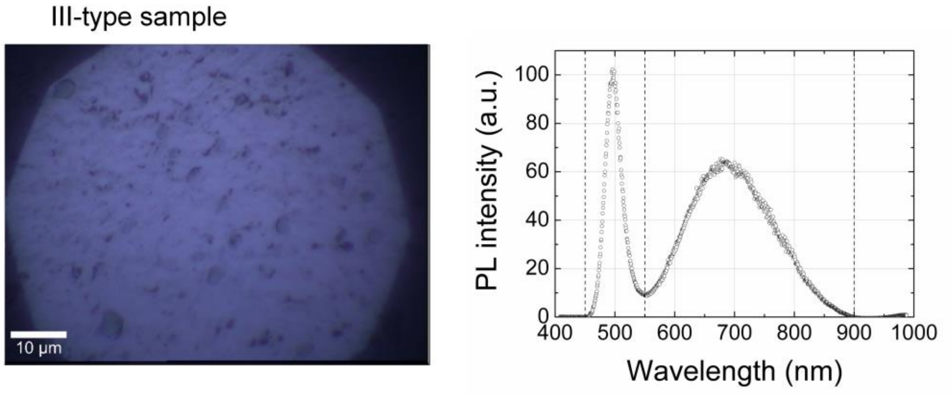

Optical image of scan area at 100× magnification

Spatially integrated PL spectrum

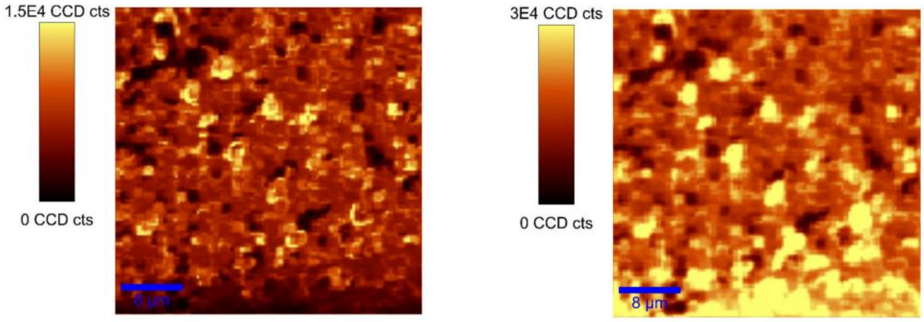

Fig. 5.6. Optical field microscopy image (top-left), a PL spectrum integrated over inspected area (top-right), the topographs of the distribution of the green-light luminescence (bottom-left) and of the red-light luminescence (bottom-right) panels, respectively, recorded on the CdS sample of the III-type.

The ratio $R_{PL}=I_{G\text{-}PL}/I_{R\text{-}PL}$ of peak intensities obtained for the I-type CdS samples is close to unity, i.e. $R_{PL\text{-}I\text{-}type}<1$. These ratios are estimated to be $R_{PL\text{-}II\text{-}type}\geq 1$ and $R_{PL\text{-}III\text{-}type}>1.5$, respectively. Spatial distribution of the $I_{G\text{-}PL}$ and $I_{R\text{-}PL}$ was examined within microscopy (CMI) scan area by using spectral filters. It can be noticed within bottom pictures in Figs. 5.4-5.6, that spatial distribution of the green PL (G-PL) and red PL (R-PL) radiative centres is obtained different among all three type samples. Namely, centres of G-PL and R-PL are spatially separated for samples of the I- and III-type samples, while locations of these G-PL and R-PL centres nearly coincide for samples of the II-type. This result confirms the enhanced generation current in BELIV transients registered for the samples of the II-type, indicating that deep traps are located in the same micro-crystallites.

Comparison of the confocal microscopy images and of the PL spectra among the CdS polycrystalline layers of different types implies that the most homogeneous CdS layer is obtained for the II-type samples. The smallest size (≤1 μm) of the micro-crystallites is unveiled for the I-type samples, while the crystallites within layers of the II-type are the largest ones (2-10 μm), as deduced from CMI. Location of the G-PL and R-PL centres is obtained to be the closest to each other for the II-type layers (Figs. 5.4-5.6). This indicates that traps responsible for G-R-PL donor-acceptor or band-deep level radiative recombination are most homogeneously distributed in the II-type samples. These observations are in agreement with BELIV characteristics, where the most qualitative CdS-Cu_2S junctions (with clearly expressed barrier capacitance) were obtained on CdS substrates of the II-type.

5.4. Photoconductivity and photoluminescence transients and quenching effects

The simultaneously measured transients of PL and MW-PC under different background illumination are illustrated in Fig. 5.7a. The reversible luminescence photo-quenching effect (PL-PQ) has been clearly observed, as a decrease of PL intensity with enhancement of the background illumination. In these experiments different bias illumination regimes, together with UV excitation of PL, have been implemented by carrying out measurements in dark, at room lighting and under illumination with incandescent lamp. The photoconductivity transients (Fig. 5.7a), however, show nearly invariant excess carrier decay (MW-PC transient) shape. Two-componential MW-PC transients with fast initial component and a long-tail are inherent for all the investigated types of samples. Duration of the initial MW-PC transient component is in the same time scale (of several nanoseconds) as in PL decay. However, the long-tail MW-PC relaxation, obtained by extrapolating this (MW-PC transient) curve to *t*=0, represents the non-exponential decay of excess carrier density due to non-radiative processes.

The photoluminescence photo-quenching effect has been also resolved for the green CW UV light excited photoluminescence band (G-PL) by examination of the confocal microscopy images, highlighted by comparing PL intensity obtained without (Fig. 5.7b) and with (Fig. 5.7c) background illumination. The intensity of background illumination was varied using incandescent lamp. Comparison of G-PL intensity of UV excited PL with and without background illumination is shown in Fig. 5.7d. The G-PL islands (Fig. 5.7b), clearly observable within microscopy image without bias illumination, disappear (Fig. 5.7c) when bias illumination is switched-on. The changes in the amplitude of PL peak are clearly seen for G-PL band, while intensity of the red PL band slightly increases within long wavelength spectral wing. Recovery of a G-PL peak intensity occurs to be noticeably long at room temperature. Thus, the luminescence photo-quenching effect seems to be accompanied with thermal quenching of PL. These luminescence photo- and thermal-quenching effects are well-known in bulk crystals of CdS material [82], and are explained by interplay of several deep traps, those redistribute excess carrier flows among different radiative and non-radiative recombination centres within crystalline volumes. A sketch of redistribution of radiative recombination flows including potential barriers is presented in Fig. 5.7e. There, bias illumination modified (lowered) barrier can be a reason for G-PL quenching. The green photoluminescence can be ascribed to the nearly interband radiative recombination, assuming the band-gap value E_G=2.42-2.47 eV [83, 84]. Existence of the G-PL within microcrystalline volumes of the CdS polycrystalline material and PL-PQ effect imply a complicated interplay of defects in redistribution of the photo- pulse excited carriers within crystalline volumes of CdS.

These changes of the confocal microscopy and PL-PQ spectroscopy characteristics are more pronounced for the II-type samples. The G-PL can be associated with interband radiative transitions observed as PL peaked at ~500 nm. A reduction of the G-PL intensity due to PL-PQ determines a seeming shift of the R-PL peak (Fig. 5.7d). Also, an increase of the steady-state R-PL intensity (within a long wavelength spectral wing) implies a switch of radiative electron-hole plasma [84] recombination flow (ascribed to G-PL) towards R-PL channel (associated with deep traps). On the basis of deep level parameters for these samples, resolved by the PIS and thermal-emission (DLTS) spectroscopy [58], the R-PL peaked at 700 nm can be ascribed to centres with activation energy $E_{A,DL}$=1.75 eV. The latter $E_{A,DL}$=1.75 value is in good agreement with that E_{DL}=1.65±0.04 eV [58] (extracted from photo-ionization spectra recorded on the same CdS samples) and corrected E_G=2.42 eV value (instead of E_G=2.52 at 300 K [91]).

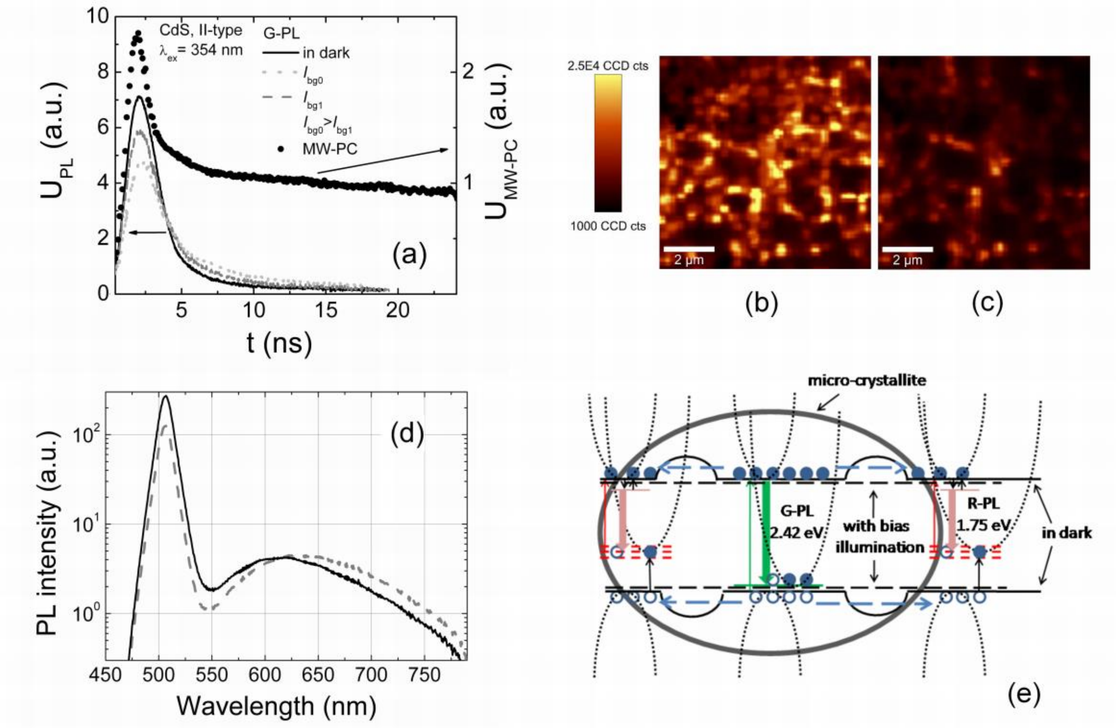

Fig. 5.7. PL photo-quenching characteristics: (a) comparison of MW-PC and PL transients varying intensity of background illumination. CdS surface PL intensity mapping in darkness (b), and under white light illumination (c), envisaged PL photo-quenching effect, when PL integrated within spectral range from 450 nm to 750 nm. (d) Spatially integrated PL spectrum for initial scan in darkness (black solid curve) and for scan made during background illumination (gray dash curve). (e) A sketch of photoluminescence quenching by redistribution of recombination flows under bias illumination.

Complicated redistribution of excess carriers among the radiative and non-radiative recombination centres within polycrystalline CdS material is corroborated by examination of the MW-PC transients (Fig. 5.8). The isomorphic MW-PC transients (within semi-log plot) over wide range of time displays from nanosecond (top axis in Fig. 5.8a) to millisecond (bottom axis in Fig. 5.8a) scales have been observed. The invariant shape transients (seeming as two-componential) for different display time-scales imply entirely non-exponential carrier decay process, when MW-PC signal is integrated over excitation laser beam spot area.

Actually, the MW-PC transients represent a sum of excess carrier densities decay through both radiative (PL) and non-radiative ($n_{ex,as}$) recombination, averaged over excitation spot area. The asymptotic decay component ($n_{ex,as}$) can be rather precisely simulated using stretched exponent model

$$n_{ex,as}(t) = n_{ex,as}(t=0)e^{-(t/\tau_{se})^{\alpha}} , \tag{5.1}$$

with fractional index α and specific time-constant τ_{se} parameters, when a peak amplitude is normalized to unity ($n_{ex,as}(t)|_{normalized}=\exp[-(t/\tau_{se})^{\alpha}]$), Fig. 5.8b. Extrapolating the fitted $n_{ex,as}(t)$ to the initial instant (t=0, ascribed to the MW-PC initial peak) of the experimental MW-PC transient ($U_{MW\text{-}PC}(t)$), a $n_{ex,PL}(t)$ density of excess carriers decaying by radiative transitions (as a differential between the initial and asymptotic components) can be evaluated. The simulated ratio

$$\frac{n_{ex,PL}(t)}{n_{ex,PL}(0)} = \frac{U_{MW-PC}(t)}{U_{MW-PC}(0)} - e^{-(t/\tau_{se})^{\alpha}} \tag{5.2}$$

is compared with experimental PL transient within an inset of Fig. 5.8b. It can be deduced from Fig. 5.8b that simulated main components of the MW-PC transient, shown in Fig. 5.8a, fit well the experimental MW-PC and PL transients, simultaneously measured on the same sample.

A comparison of MW-PC and PL transients obtained in different type CdS samples is presented in Fig. 5.9. It can be noticed that the initial carrier decay rate through the non-radiative recombination channels, highlighted within MW-PC transients, is higher in samples of I-type containing the lowest equilibrium carrier density. Amplitude of the asymptotic relaxation for I-type sample is larger than that for II- and III-type samples. The observed differences of MW-PC transients can be explained by larger volumes of microcrystals in II- and III-type samples. Owing to the larger volumes (and ratio of bulk material to crystallite surface) of microcrystals in II- and III-type samples, as observed in confocal microscopy images, Figs. 5.4-5.6, the radiative (G-PL) interband recombination efficiency is elevated in II- and III-type samples. The radiative interband recombination seems to be responsible for the fast initial decay component.

Excess carrier decay at microcrystal boundaries and within disordered structure surrounding the microcrystals appears through carrier capture limited random-walk. The latter process leads to the stretched exponent inherent behaviour of carrier density relaxation. The rate of asymptotic carrier density changes (Fig. 5.9b) depends on the structure of disordered material, which is characterized by the fractional index α and by a specific stretched exponent lifetime τ_{se}. The PL transients also exhibit different initial (Fig. 5.9c) and asymptotic (Fig. 5.9d) PL relaxation. The slowest initial PL decay is again observed in I-type samples. While asymptotic PL relaxation is inherent for all the investigated types of CdS samples, but rate of carrier decay within this asymptotic relaxation component is different for various types of samples. These observations imply, that processes of radiative recombination, during rather long time of about 200 ns (Fig. 5.9d), contemporize also in microcrystals surrounding structure by exchange of carriers between microcrystals and their boundary area. The asymptotic tail of PL transients (Fig. 5.9d) can be also associated with PL spectrum changes under varied excitation density (Fig. 5.10). The G-PL photo-quenching is clearly expressed for all types of samples. A shift of G-PL peak intensity to the long wavelength (R-PL) wing peak intensity appears also with increase of pulsed excitation density (Fig. 5.10).

This can be explained by excess carrier density accelerated radiative recombination through trap levels, assuming a non-radiative capture of carriers before radiative transition. Here, a barrier inherent behaviour of carrier transport mediated radiative recombination can be also implied. It can be assumed that barrier widens and sinks with increase of excess carrier density, and thereby energy of emitted photons decreases. Such a behaviour can be explained by barrier existence for different recombination counter-partners, i.e. holes and electrons involved [84]. On the other hand, these PL spectral shifts, accompanied by PL photo-quenching, can be alternatively explained by processes, governed by interplay of point traps [82]. Here, the switch of recombination flow from deeper trap to shallower one (being, r and s centres in nomenclature of [82, 86]) is the main reason of spectral changes.

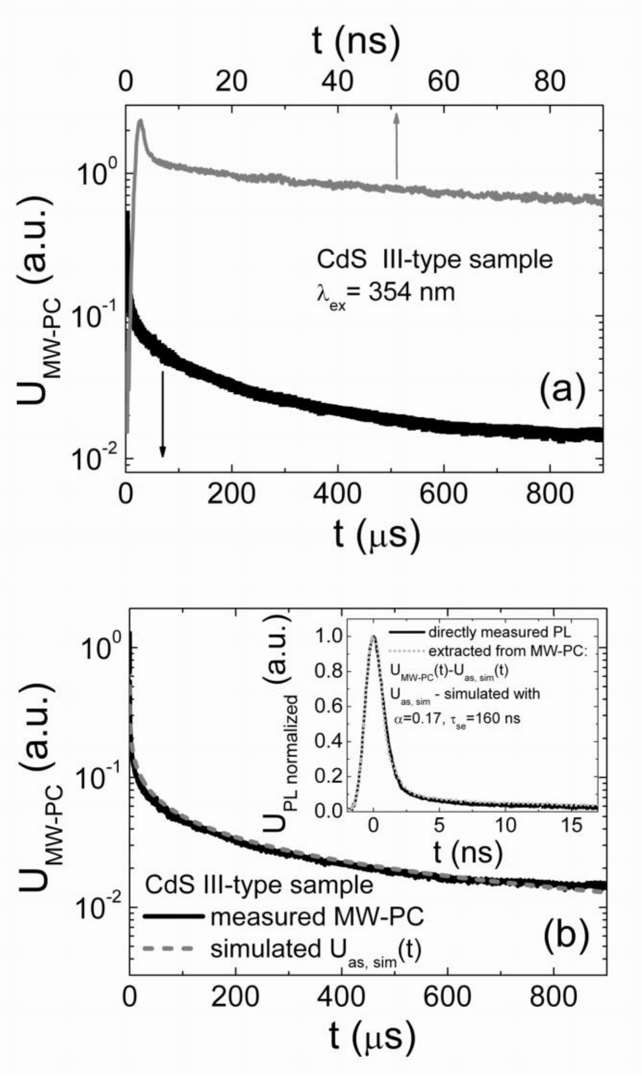

Fig. 5.8. a - MW-PC transients, recorded using different display scales (top – ns scale, grey curve; bottom - μs scale, black curve) and represented within semi-log plot. b - Comparison of simulated components of PL (in the inset, by subtracting the fitted and simulated stretched exponent from the experimental decay curve) and MW-PC (simulated stretched exponent relaxation) with experimental ones.

Dependence of the asymptotic PL component on sample type is confirmed by the MW-PC transients recorded for different type samples (Fig. 5.11). This dependence can be roughly estimated (Fig. 5.11a) by analysis of the ratio of the amplitudes $r_{asti}=U_{as}/U_{in}$, using values of the asymptotic U_{as} relaxation, extrapolated to the initial decay moment (t=0), and that of the initial decay peak U_{in}. The smallest r_{asti} ratio has been obtained for II-type samples, while this ratio r_{asti} is the largest for the I-type samples. The large relative amplitude U_{as} indicates the enhanced role of the disorder, where excess carrier non-radiative recombination is governed by carrier random-walk transport. The smaller the r_{asti} is the more efficient integral PL efficiency is obtained. There, carrier recombination within micro-crystallites prevails within initial component of MW-PC transient.

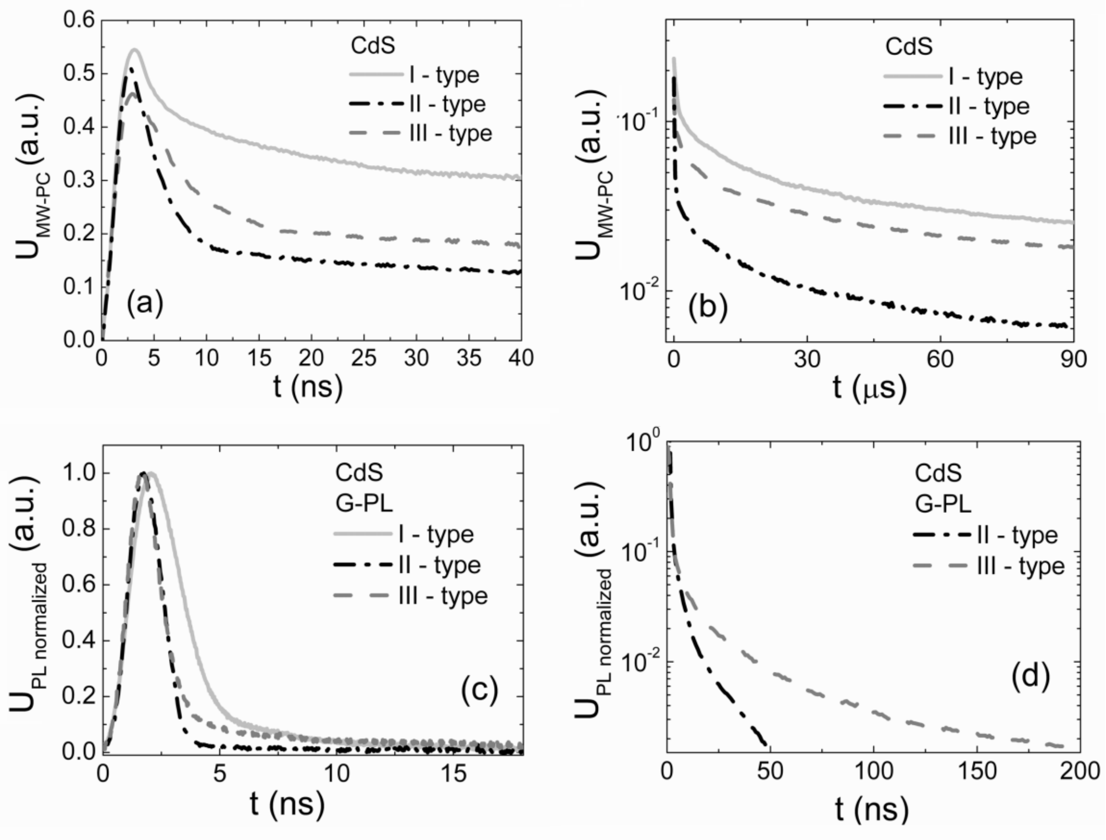

Fig. 5.9. Comparison of the MW-PC initial (a) and asymptotic (b) decays correlated with G-PL of the initial (c) and asymptotic (d) relaxation components in polycrystalline layers of I-, II- and III-type samples of CdS material.

A linearization of the U_{as} within MW-PC transients is possible when using a stretched exponent approximation, e.g. (Refs. [87, 88])

$$n_{ex}(t) = n_{ex}(t=0)e^{-(t/\tau_{se})^{\alpha}}, \tag{5.3}$$

with fractional index α. Such a display of a MW-PC transient is illustrated in Fig. 5.11b. Fractional index α is obtained from a linear fit of $U_{as}(t)$ variations using a plot of the double logarithm for normalized U_{as} values versus a logarithm of time, i.e. $\ln(\ln(U_{MWR}(0)/U_{MWR}(t)))$ versus $\ln(t)$. Values of α can then be associated with material disorder characteristics, such as scaling exponents d_w, d_f, ζ [89, 90]. Additionally a fractal factor f, defined as a measure of the compression of a configuration space, can be employed in analysis of the fractional index α. These parameters had been introduced within axiomatic Scher-Lax-Phillips (SLP) model [91, 92] which provides an unambiguous way to interpret experimental results. This approach has been exploited for the analysis of the microwave probed photoconductivity U_{as} in different types of CdS polycrystalline layers, in this work.

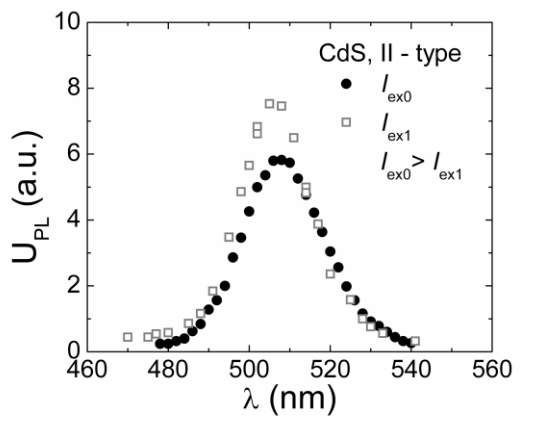

Fig. 5.10. Comparison of PL spectra under pulsed excitation of varied intensity in II-type sample. The G-PL peak intensity decreases and peak slightly shifts to the long wavelength wing with increase of pulsed UV excitation intensity: I_{ex0} (solid symbols)>I_{ex1} (hollow symbols).

The SLP model provides a straightforward path to analyze the experimental values of the fractional index α. This model is built upon the assumptions that the dissipation of excitations occurs via a system of fixed randomly distributed traps, while the system is microscopically homogenous. From here it follows that in the asymptotic limit the system exhibits SER with the fractional index defined as $\alpha=d/(d+2)$, where d denotes the dimensionality. Then, it is supposed that in some cases the relaxation dynamics is governed by short- and long-range interactions, which lead to a compression of configuration space and, consequently, to a more general definition of α, i.e. $\alpha=d^*/(d^*+2)$, where $d^*=fd$ is the effective dimensionality. In a wide variety of glasses, f is usually equal to 1 or 1/2, that are specific values to short-range and mixed short- and long-range forces, respectively. However, for polycrystalline materials f can attain even smaller values [92], since a large part of the effective degrees of freedom is inactive due to clustering. Values of fractional index α and fractal factor f for samples of various types, obtained from curves depicted in Fig. 5.11b, are presented in Table 5.4. From these results, it can be inferred that samples of the II-type and the III-type are structurally similar, and that samples of the I–type possess a distinguishably disordered structure.

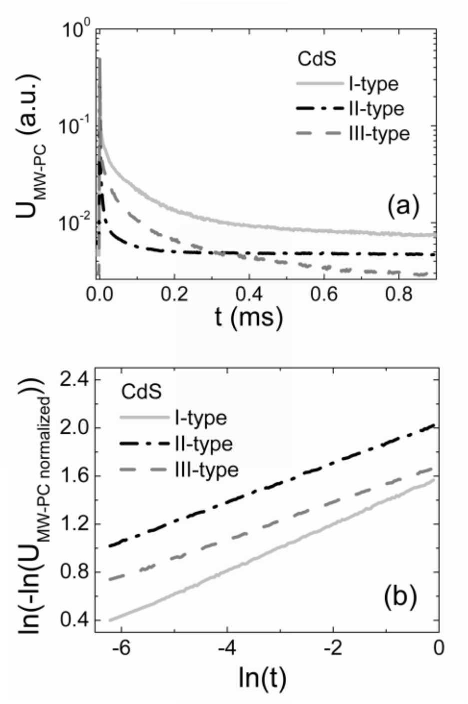

Fig. 5.11. Comparison of the MW-PC transients recorded in I- to III-types of CdS samples at 354 nm wavelength pulsed excitation (a), and display of transients in the stretched exponent scale (b).

Table 5.4. Parameters of disorder in samples of different type.

Parameter	Sample type		
	I-type	II-type	III-type
α	0.20	0.16	0.17
f	0.17	0.13	0.14

The performed study of the CdS polycrystalline material layers by applying combination of different techniques enabled us to separate a few types of samples those differ in density of doping and carrier capture centres. The samples had been sorted into three types according to differences in BELIV transient shapes (Fig. 5.1), which were identified assuming variation of relative densities of dopants and carrier capture, caused by slight changes of layer deposition regimes. Value of free carrier density of the n_0=1.5×10^{13} cm^{-3} is estimated for junctions of II- and III-type, and it determines the concentration of shallow traps. For the I-type samples, equilibrium carrier density is significantly smaller, thus junction appeared to be fully depleted without external applied voltage.

Spatial inhomogeneity, caused by dislocations and other extended imperfections located within the periphery areas surrounding microcrystals, determines carrier recombination and transport features. Excess carriers, brought to the periphery areas, containing space charge regions, are separated by space charge field, and their recombination is only mediated by diffusion, owing to excess carrier density gradients. Carrier capture within local space-charge region fields seems to be potential barrier modified. Screening of this barrier is dependent on equilibrium and excess carrier density. Thereby, the observed G-PL peak intensity in different type samples and its spectral shifts can be explained by variation of carrier densities in various type polycrystalline structures.

Different (fast and slow) carrier decay components should be ascribed to different micro-areas of CdS polycrystalline material. It has been confirmed by photoluminescence microscopy, that PL signal contains a granular structure. Thus, the simultaneous control of photoconductivity (ascribed to integrated over excitation beam spot area) and green photoluminescence (associated with interband recombination within micro-crystalline volumes) spectrum and time resolved signals can be a tool to resolve an impact of different micro-volumes to carrier decay parameters.

Two spectral bands of photoluminescence have been observed within all types of samples: a narrower band of green luminescence peaked at 500 nm, which can be associated with interband radiative recombination, and a wider spectral band of red luminescence with a peak at 700 nm, which can be ascribed to deep traps, mediated radiative transitions. The ratio between the green PL to the red PL intensities, as $R_{PL}=I_{G\text{-}PL}/I_{R\text{-}PL}$, is found to be $R_{PL\text{-}I\text{-}type}<1$ for the I-type CdS samples, while values of this ratio are estimated to be $R_{PL\text{-}II\text{-}type}\geq 1$ and $R_{PL\text{-}III\text{-}type}>1.5$, respectively. Centres of G-PL and R-PL are spatially separated for the I- and III-type samples, while value $R_{PL\text{-}III\text{-}type}>1.5$ indicates the smallest density of deep traps in III-type samples. Spatial location of these G-PL and R-PL centres nearly coincides for samples of the II-type, as identified from images in Figs. 5.4-5.6.

The confocal microscopy images among the CdS polycrystalline layers of different types imply that the most homogeneous CdS layer is obtained for the II-type samples, deposited at 260 C for 75 min. While the PL spectra show that interband recombination within microcrystals (associated with G-PL) prevails in III-type samples, deposited at 260 C for 80 min. This is in agreement with BELIV characteristics, where the most qualitative CdS-Cu_2S junctions (with clearly expressed barrier capacitance and a relatively small leakage current) were obtained on CdS substrates of the III-type.

The photoluminescence photo-quenching effect has been clearly observed (Figs. 5.7, 5.10). The photoluminescence photo-quenching effect has been ascribed to the microcrystalline areas within polycrystalline CdS material and resolved for the green photoluminescence band (G-PL) by examination of the confocal microscopy images without and with background illumination, using incandescent lamp. Existence of the G-PL within microcrystalline volumes of the CdS polycrystalline material and PL-PQ effect imply a complicated interplay of defects in redistribution of the photo-pulse excited carriers over crystallites. The PL-PQ effect is more pronounced for the II-type samples. This can be explained by competition and interplay of radiative and non-radiative recombination centres in redistribution of carrier flows, located within the same crystalline volumes. For all the investigated types of samples, a shift of PL peak appears with decrease of excitation density (Fig. 5.10). This implies a barrier specific behaviour of carrier transport to radiative recombination centres.

Two-componential MW-PC transients with fast initial component and a non-exponential long tail are inherent for all the investigated types of samples, and this is a feature of the polycrystalline structure. Duration of the initial MW-PC transient component is in the same time scale (of several nanoseconds) with G-PL decay, thus it represents carrier density relaxation within crystalline volumes. Only rather small part of excess carriers is shared within radiative recombination processes, observable in PL signal changes. The radiative recombination processes represent the excess carrier density changes within microcrystals, thereby the time scale of the initial MW-PC (U_{in} as a sum of PL and non-radiative recombination, incorporated within U_{as}) and of G-PL signals coincide. The MW-PC response amplitude is proportional to the whole density of excess carriers. Thus, ratio of amplitudes $r_{asti}=U_{as}/U_{in}$ of the MW-PC relaxation components can be a measure for carrier densities decaying within microcrystals and surrounding volume of CdS polycrystals investigated (Figs. 5.8, 5.10 and 5.11). The observed differences of MW-PC transients, when comparing different type samples, can be explained by largest volumes (proven by CMI) of microcrystals in the II-type samples. The excess carriers decay within microcrystals through radiative recombination, is associated with fast initial MW-PC and PL components. The slower PL and MW-PC relaxation components can be ascribed to carrier recombination within microcrystals and their diffusion to microcrystal boundary.

A linearization of MW-PC transients is possible when using a stretched exponent approximation,

$$n_{ex,as}(t) = n_{ex,as}(t=0)e^{-(t/\tau_{se})^{\alpha}}, \tag{5.4}$$

with fractional index α different for different types of CdS structures investigated. Analyzing values of fractional index α, obtained being in the range of α=0.16-0.20 for different samples, conclusions about the structural properties of studied polycrystalline layers can be indirectly drawn. Additionally, the obtained values of $\alpha<1$ hint on dominance of the anomalous character of excess carrier transport within a disordered structure of CdS polycrystals investigated. It has been inferred that samples of the II-type and the III-type are structurally similar and are characterized by fractal factor of $f\cong0.14$, and that samples of the I–type exhibit a distinguishably disordered structure with fractal factor $f\cong0.17$.

By summarizing the results on investigation of the photoluminescence and the photoconductivity transients, it should be inferred that two spectral bands of photoluminescence have been observed within all types of samples, - a narrower spectral band of green luminescence peaked at 500 nm and a wider band of red luminescence with a peak at 700 nm. The ratio between the green PL to the red PL intensities as $R_{PL}=I_{G\text{-}PL}/I_{R\text{-}PL}$ has been obtained for the I-type CdS samples $R_{PL\text{-}I\text{-}type}<1$, while these values are estimated to be $R_{PL\text{-}II\text{-}type}\geq1$ and $R_{PL\text{-}III\text{-}type}>1.5$, respectively. The photoluminescence photo-quenching effect has been ascribed to the microcrystals within polycrystalline CdS material. The PL-PQ effect implies a complicated interplay of defects in redistribution of the photo- pulse excited carriers. The confocal microscopy images of CdS polycrystalline layers for different type samples enabled us to conclude that the most homogeneous CdS layer is obtained for the II-type samples, deposited at 260 C for 75 min. While, in III-type samples deposited at 260 C for 80 min, the PL spectra show that G-PL within microcrystals prevails the traps ascribed R-PL.

The ratio of amplitudes $r_{asti}=U_{as}/U_{in}$, - of the asymptotic component U_{as} (extrapolated to t=0) to the initial MW-PC peak U_{in}, can be a measure for carrier densities decaying within microcrystals and inter-crystallites volume of

CdS polycrystal. The observed differences of MW-PC transients can be explained by larger volumes of micro-crystallites in II- and III-type samples. These observations are corroborated by microscopy imaging. Additionally, density of deep traps is the smallest in microcrystals of III-type samples. However, the most homogeneous distribution of microcrystals has been obtained for II-type samples.

A linearization of MW-PC transients can be performed by using a stretched exponent approximation, with different fractional index α values for separated types of CdS structures.

5.5. In situ evolution of the electrical-optical characteristics in poly-CdS layers

Polycrystalline CdS can also be exploited as a cheap scintillating material for visualization of particle beams and for dosimetry. However, radiation hardness of the polycrystalline CdS is poorly investigated. In addition, the heterostructures Cu_2S-CdS formed on these polycrystalline CdS layers show an opportunity to employ the heterostructures as the particle sensors. Thereby, such a sensor could be suitable for synchronous detection of the optical (acting as a scintillator) and electrical (as a charge collection sensor) responses. Therefore, variations of the characteristics of the proton induced luminescence (PI-L) and of MW-PC transients had synchronously been measured (during irradiation by 1.6 MeV protons) and correlated to evaluate the changes of the radiative and non-radiative recombination in polycrystalline CdS. In order to estimate the suitable range of the resolvable changes of scintillation signals, the efficiency of the optical and particle excitation of the luminescence signals has been studied. Moreover, the defect introduction rate has been evaluated by calibration of the luminescence intensity and the density of the generated excess carriers induced by laser irradiation and proton beam. The difference of a carrier pair generation mechanism inherent for light and for a proton beam has been revealed. This observation has been explained by differences in the momentum conservation conditions inherent for the carrier generation by photons and protons.

For the in situ measurements, the sample was mounted on a cold finger within a specially fabricated irradiation chamber [49, 50]. This chamber contains the coaxial and fiber connectors to transfer the optical and microwave signals between probes inside a vacuum chamber and the measurement instrumentation placed remotely from the irradiation area. The irradiation chamber is also equipped with 3D actuators to adjust the proton beam location on the sample. Protons are accelerated to 1.6 MeV using the Tandetron 4110A ion accelerator. The MW-PC and quasi-steady-state PI-L signals were synchronously recorded during an exposure to a proton beam. The PI-L signals were integrated over τ_{PL-av}=300 ms using a photometer Avantes AvaSpec-2048TEC equipped with a fiber adjusted input.

The simultaneous measurements of the evolution of luminescence and photoconductivity were performed to correlate variations of the recombination parameters in the area subjected to the proton beam. The simultaneous measurements also enabled us to reduce the influence of the lateral inhomogeneity in the polycrystalline layers under study.

The changes in proton induced luminescence spectra obtained during irradiation with 1.6 MeV protons are illustrated in Fig. 5.12a. The spectra consist of two main bands of green (G-L) and red (R-L) luminescence peaked at 552 and 709 nm, respectively, Fig. 5.12b. The G-L band can be attributed to the interband recombination since the band-gap value E_G=2.42-2.47 eV has been previously reported [45, 93]. The R-L band is related to the recombination through the deep levels.

The ratio of the intensities $R_{PL}=I_{G-PL}/I_{R-PL}<1$ of G-L and R-L indicates that the material contains high density of deep traps. These traps act as the centres of donor-acceptor (D-A) radiative transitions. The revealed variation of the peak intensities for the G-L and R-L spectral bands during the irradiation is presented in Fig. 5.12c. The intensity of both the G-L and R-L bands decreases insignificantly under proton irradiation at fluences $\Phi \leq 10^{13}$ cm^{-2}. However, for

$\Phi>10^{13}$ cm^{-2} the intensity of both spectral bands starts to decrease significantly. It can be understood as redistribution of carrier decay flows among channels of the radiative and non-radiative recombination, where the radiation defects act as the non-radiative recombination centres which density is enhanced with irradiation exposure time and, consequently, fluence.

MW-PC transients recorded at different instants, during irradiation by 1.6 MeV protons, are presented in Fig. 5.13a. The two-componential transients of the excess carrier decay have been observed, which contain a fast initial constituent and a slow asymptotic term. It was revealed in our previous study, Ref. [78], that a disordered structure is inherent for these CdS polycrystalline layers. The disorder determines the non-exponential decay characteristic with the long asymptotic component. Such a relaxation curve of the changes of carrier density in time t can well be approximated by the stretched-exponent model (SE) (5.4) with a fractional index α and a characteristic time $\tau_{SE.}$ The best fits for different samples fabricated by the same technology regimes have been obtained at the fractional index α varying in the rage of α=0.17-0.20. The rather small values of α indicate a large degree of disorder in comparison with the perfect crystals (with α=1) or crystals containing nets of extended defects (with α>0.5). The drastic disorder of the examined CdS polycrystalline layers considerably complicates analysis of the changes of stretched-exponential transients with α<0.15. Therefore, the changes of the instantaneous lifetimes for the transients recorded on the microsecond time scale have been examined. This enabled us to reduce the transient acquisition time during the rapid measurements in search of evolution of the carrier decay rates (Fig. 5.13a), and to reduce an impact of the electrical noises inevitable during operation of a proton accelerator. The recorded changes of the instantaneous decay lifetime τ as a function of the fluence of irradiation by 1.6 MeV protons are shown in Fig. 5.13b. It has been obtained that changes of the instantaneous decay lifetime correlate well with the PI-L intensity changes relative to a fluence scale. The decrease of the instantaneous decay lifetime τ from 3 to 1 μs is clearly observed (Fig. 5.13b) in the range of fluences $\Phi \leq 5\times10^{14}$ cm^{-2} in agreement with PI-L characteristics (Fig. 5.12c).

One of the objectives of this study was to correlate the changes of the non-radiative and radiative recombination characteristics during irradiation by high energy protons. It has been verified by TRIM simulations that the stopping range of 1.6 MeV protons (~23 μm) exceeds the thickness of the samples under study (d=20 μm). As a consequence, the energy loss of protons was nearly homogeneous within the CdS layer thickness. In contrary, the optical excitation at 345 nm wavelength determines the initially inhomogeneous excitation due to a large absorption coefficient β=1.25×10^{5} cm^{-1} [96].

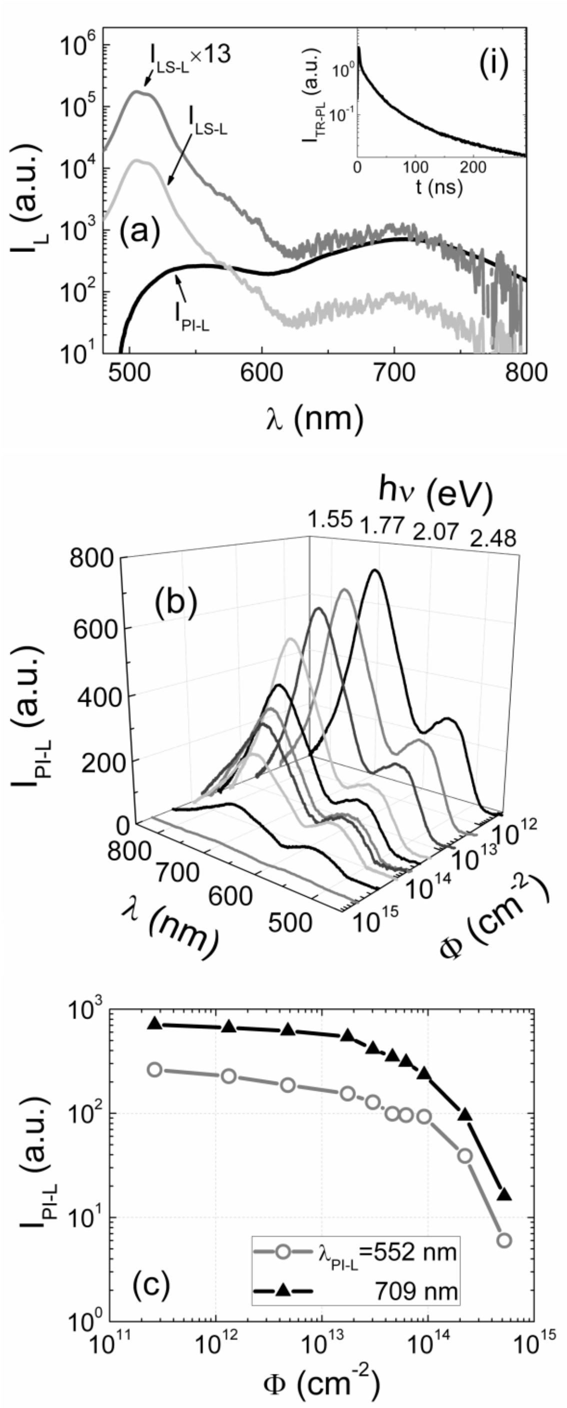

Fig. 5.12. a - Comparison of the laser induced luminescence spectra recorded using the steady-state measurement regime in the non-irradiated CdS layer recorded under pulsed laser excitation and that PI-L excited by a proton beam of very small fluence (the dark-gray curve represents a magnified amplitude of a LS-L spectrum). TR-PL transient measured for R-L spectral band is shown in the inset (i); b - Evolution of the proton induced luminescence spectra with irradiation fluence; c - variation of peak intensities in two luminescence bands as a function of fluence of irradiation by 1.6 MeV protons.

Thereby, a layer-depth distribution of the excess carrier density acquires the stabilized in-depth profile only after diffusion time $t_D \cong d^2/D = 4$ μs (estimated using approximation $d \cong (Dt_D)^{1/2}$) overwhelming the layer thickness d. Here, $D \cong 1$ cm^2/s is the coefficient of carrier ambipolar diffusion in CdS [97]. The transitional process of the profile stabilization might also be a reason of the fast initial component in the decay of photoconductivity and TR-PL (inset in Fig. 5.12a) with characteristic decay time of ~30 ns.

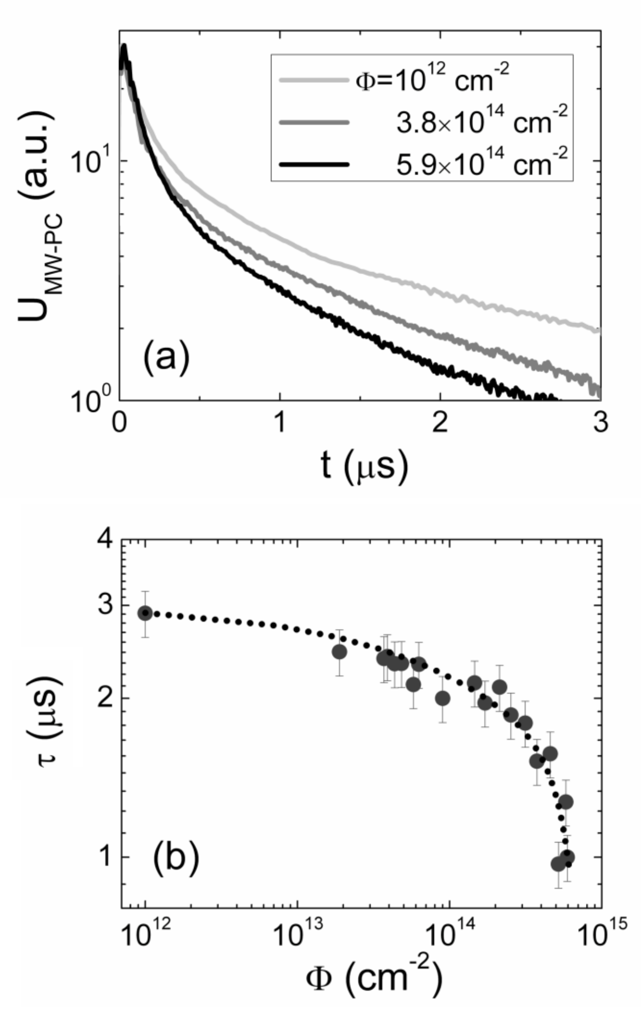

Fig. 5.13. a - MW-PC transients recorded at different instants during 1.6 MeV proton irradiation (corresponding fluences are indicated in the legend); b - variation of effective carrier lifetime values as a function of 1.6 MeV proton irradiation fluence.

In our experiments, the areas ($A_L = 3.1\times10^{-2}$ cm^2) of the laser beam spot and the microwave needle-tip probe are significantly smaller than the area $A_P \approx 7$ cm^2 of the proton beam spot. Thereby simultaneous in situ measurements of the MW-PC transients and the steady-state recorded luminescence (S-L) spectra can be accomplished during proton irradiation. The proton induced S-L signal has been collected by a multi-fiber probe of the total area of A_{pr}=3×10^{-2} cm^{2}. This multi-fiber probe has been spatially separated a little bit from the laser beam spot location within the proton beam spot, to avoid an optical noise due to scattered laser light. In Fig. 5.12a, the S-L spectra excited by a laser (LS-L) pulse and by a 1.6 MeV proton beam (PI-S-L, at a very initial stage of irradiation, - 1 sec) are compared. The laser excitation has been implemented using 354 nm wavelength light with the total excitation energy of E_{L}=0.11 μJ per laser pulse. The spectra shown in Fig. 5.12a PI-S-L have been recorded at the proton beam current of i_P=24 nA.

5.6. Evaluation of the detector and dosimeter parameters

This comparison has been employed to evaluate initially the excess carrier density excited by protons and to relate it to the red S-L (at 709 nm wavelength) induced by protons (R-PI-L). The dark-grey curve in Fig. 5.12a represents the R-LS-L spectrum (magnified by a factor of 13) recorded under laser pulse excitation. The magnification factor has been chosen to match the intensity of the red luminescence under laser (R-LS-L) and proton beam (R-PI-L) excitations. The average of the excess carrier density generated by the proton beam can be evaluated by comparison of the corresponding density generated by the laser pulse. The latter can be estimated using the absorption coefficient β at the laser light wavelength. To increase the evaluation precision, the inhomogeneity of the laser excitation and the time integration of S-L signal have been taken into account. The density n_0 of the excess carriers photo-generated by the laser is evaluated by relation $n_0=\beta E_{\mathrm{L}}/A_L E_1=7.8\times10^{19}$ cm^{-3}. Here, E_{L} is the fixed total energy per laser pulse used in calibration measurements, A_L is the area of a laser beam spot, and E_1=3.5 eV is the quantum energy with a unit efficiency of carrier pair production at 354 nm wavelength. The depth averaged

$$< n_L >_d = n_0 \left(\frac{1}{d}\right)\int_0^d e^{-\beta x} dx = \frac{n_0}{\beta d}(1-e^{-\beta d}) \cong 3.1\times 10^{17} cm^{-3} \tag{5.5}$$

carrier density can then be equalized with excess pair density n_P generated homogeneously in d by the penetrative protons. The equivalent density n_P of excess carrier pairs generated permanently by a proton beam would be equal to $<n_L>_\mathrm{d}$ if the time of signal integration coincides with t_D, i.e. for $<n_L>_\mathrm{d} t_D = n_P t_D$. However, the changes of the laser induced carrier density due to recombination are not accounted for within the equality $<n_L>_\mathrm{d} t_D = n_P t_D$. To include the carrier density reduction caused by recombination, the resultant density of carriers is expressed as $<n_L>_\mathrm{d}\, f(\tau_{R\text{-}L}, t_D)$, where the coefficient

$$f(\tau_{R-L}{}^{in}, t_D) \cong \frac{1}{t_D}\int_0^t \exp\left[-\frac{t}{\tau_{R-L}{}^{in}}\right] dt \tag{5.6}$$

evaluated for $\beta d=1$ is introduced. It has been obtained by equalization of the intensities (Fig. 5.12a) for the R-LS-L and that integrated density $n_P t_D$ exceeds the $<n_L>_\mathrm{d} t_D$ by about 13 times (i.e. $n_P t_D / <n_L>_\mathrm{d} t_D = 13$ when changes of laser induced carrier density due to recombination are not accounted). The calculated value of $f(\tau_{R\text{-}L}{}^{in},\ t_D) \cong 7.5\times 10^{-3}$ with $f(\tau_{R\text{-}L}{}^{in},\ t_D) \cong \tau_{R\text{-}L}{}^{in}/t_D$ is then obtained. These evaluations have been performed using the initial TR-PL decay time $\tau_{YG\text{-}L}{}^{in}$~30 ns for R-L band estimated from the UV pulsed laser induced TR-PL transient (inset in Fig. 5.12a), and the spectro-photometer signal obtained by integrating spectral response over t_D=40 μs. Then, n_p is evaluated as $n_p = 13 f(\tau_{R\text{-}L}{}^{in},\ t_D) <n_L>_\mathrm{d} = 3\times 10^{16}$ cm^{-3}. The number of electron hole pairs generated by a single 1.6 MeV proton can be estimated by independent evaluation of the proton flux using the proton beam current i_P and the beam area A_P=7 cm^2. The flux of protons is then obtained to be $F_P = i_P/eA_P \cong 2.1\times 10^{10}$ cm^{-2}s^{-1} with $e = 1.6\times 10^{-19}$ C as the elementary charge of proton.

Then, the quantity of protons crossing the CdS layer has been estimated to be $N_P = F_P \tau_{L\text{-}av} A_P \cong 1.5\times 10^9$. These protons generate the R-L signal integrated over the time $\tau_{L\text{-}av}$=10 ms. This signal is equivalent to a R-L signal obtained due to excitation by a single laser pulse. The correlation procedures enabled evaluation of the efficiency κ_P of the carrier density generation by a single proton $\kappa_P=n_P/N_P$. The κ_P value $\kappa_P\cong2\times10^7$ cm^{-3} per proton has then been estimated. The number of charges collected per unit length of a sensor material is an important parameter in the design of particle detectors. This parameter $\kappa_P A_P$ represents the efficiency κ_P of the carrier density generation by a single proton within the beam of area A_P, and it can be evaluated using κ_P. For the CdS layers under study, it has been estimated to be $\kappa_P A_P=60$ carrier pairs per a micrometer of the layer depth per 1.6 MeV proton. This $\kappa_P A_P=60$ μm^{-1}p^{-1} value is close to the values for the wide-gap materials, as listed in Ref. [98].

The defect introduction rate can be evaluated from the evolution of the R-PI-L reduction as a function of fluence. The R-PI-L decrease can be explained through the reduced rate of excess carrier generation by proton flux g_P ($n_P=g_P\tau_{rd}$). The reduction is caused by shortening of the carrier capture time τ_{rd} due to increasing density of the radiation induced defects $N_{rd}=1/\sigma_{rd}\tau_{rd}v_T$ with the parameters of capture cross-section σ_{rd} and thermal velocity v_T. This PI-L intensity decrease is observable when τ_{rd} becomes shorter than τ_{PI-L} (i.e. $\tau_{rd}<<\tau_{PI-L}$). The instantaneous lifetime of the TR-PL decay time in the stage of asymptotic decay for the spectral range of R-L was evaluated for the same non-irradiated CdS sample (see inset in Fig. 5.12a) to be equal to $\tau_{R-L}^{as}=200$ ns. Therefore, the observable density N_{rd} is in the range of $N_{rd0}\cong5\times10^{13}$ cm^{-3}, assuming the typical values of σ_{rd}~10^{-14}cm^2 and v_T~10^7 cm/s. Using the clearly expressed fragment of a curve of changes of the R-L peak values in Fig. 5.12c, the introduction rate $K_P=\Delta N_{rd}/\Delta\Phi\sim\Delta I_{R-L}/\Delta\Phi$ of radiation defects is estimated to be $K_P\cong0.9$ cm^{-1}.

The difference of a carrier pair generation mechanism inherent for light and for a proton beam can be deduced from Fig. 5.12a. It can be seen that a laser light excitation leads to the immediate luminescence with prevailing of the direct interband (excitonic) transitions. However, the radiative interband recombination is significantly weaker (by about three orders of magnitude) under proton irradiation. This can be understood by considering a momentum

$h\mathbf{k}$ conservation conditions in the photon-electron and proton-atom-electron interactions. In the former case, momentum conservation is easily fulfilled owing to a small momentum of a photon. Under photo-excitation of the direct-band-gap semiconductors, the photon absorption results in excitation of electron and hole with nearly equal quasi-momenta, since the photon momentum is comparatively small. Consequently, they efficiently recombine via direct optical transitions. Meanwhile, the proton momentum is considerably larger than that of photon. Thus, the probability of electron-hole pair excitation via direct band-to-band excitation is considerably lower. Meanwhile for carrier pair generation by proton, the momentum conservation within **k**–space seems to be impossible for the direct interactions due to large momentum of a proton. One of the possible mechanisms would be the carrier generation during annihilation of the primary radiation defects, e.g. vacancy–interstitial pairs. Then, a motion of such carriers within a coordinate space would be rather free. Thereby, radiative recombination through the D-A transitions is the most efficient mediated by the diffusion brought carriers. The obtained opposite ratio for the interband and D-A radiative recombination intensities ascribed to the light and the proton excitation, respectively, is similar to that observed in GaN epi-layers.

Summary of the chapter

[A1, A5, A8, P5]

The results on investigation of the photoluminescence and the photoconductivity transients showed two spectral bands of photoluminescence that have been observed within all types of samples, - a narrower spectral band of green luminescence peaked at 500 nm and a wider band of red luminescence with a peak at 700 nm. The ratio between the green PL to the red PL intensities as $R_{PL}=I_{G-PL}/I_{R-PL}$ has been obtained for the I-type CdS samples $R_{PL-I-type}<1$, while these values are estimated to be R_{PL}-$_{\text{II-type}}\geq 1$ and R_{PL}-$_{\text{III-type}}>1.5$, respectively. The PL-PQ effect has been ascribed to the microcrystals within polycrystalline CdS material. It implies a complicated interplay of defects in redistribution of the photo- pulse excited carriers. The confocal microscopy images of CdS polycrystalline layers for different type samples enabled us to conclude that the most homogeneous CdS layer is obtained for the II-type samples, deposited at 260 C for 75 min. While, in III-type samples deposited at 260 C for 80 min, the PL spectra show that G-PL within microcrystals prevails the traps ascribed R-PL.

The ratio of amplitudes $r_{asti}=U_{as}/U_{in}$, - of the asymptotic component U_{as} (extrapolated to t=0) to the initial MW-PC peak U_{in}, can be a measure for carrier densities decaying within microcrystals and inter-crystallites volume of CdS polycrystal. The observed differences of MW-PC transients can be explained by larger volumes of micro-crystallites in II- and III-type samples. These observations are corroborated by microscopy imaging. Additionally, density of deep traps is the smallest in microcrystals of III-type samples. The most homogeneous distribution of microcrystals has been obtained for II-type samples.

A linearization of MW-PC transients can be performed by using a stretched exponent approximation, with different fractional index α values for separated types of CdS structures. The obtained values of α=0.16-0.20 hint on dominance of the anomalous character of excess carrier transport within a disordered structure of CdS polycrystals investigated. It has been inferred that samples of the II-type and the III-type are structurally similar and characterized by a fractal factor of $f\cong0.14$, and that samples of the I–type show a distinguishably disordered structure characterized by the fractal factor $f\cong0.17$.

Variations of the characteristics of the PI-L as well as LS-L characteristics and of the MW-PC transients had been examined in order to reveal the peculiarities of radiative and non-radiative recombination in polycrystalline CdS layers. This study also enabled us to determine the radiation damage and particle generation parameters. The correlative analysis of the parameters of microwave probed photoconductivity, of time resolved luminescence spectroscopy and of the in situ changes in the synchronously measured steady-state luminescence spectral structure and MW-PC transients during 1.6 MeV proton beam irradiation enabled us to evaluate the following parameters: the efficiency of the carrier pair generation κ_P=2×10^{7} cm^{-3} per 1.6 MeV proton, the introduction rate of radiation defects K_P≅0.9 cm^{-1}, and a probable quantity of the collected charge per unit length of a sensor as $\kappa_P A_P$=60 μm^{-1}p^{-1}. The latter $\kappa_P A_P$ value is close to the inherent values for the wide-gap materials. The difference of a carrier pair generation mechanism inherent for light and for a proton beam has been revealed. This observation has been explained by differences in the momentum $h\mathbf{k}$ conservation conditions inherent for the carrier generation by photons and protons. The possible mechanism of excess carrier excitation by a proton beam could be a carrier generation process through the very fast annihilation of the primary vacancy–interstitial type radiation defects. A suitable range of the resolvable changes of scintillation signals in the range of proton fluences $\Phi<10^{15}$ cm^{-2} has been determined for CdS polycrystalline layers.

VI. Characterization of GaN structures

GaN is a promising material for radiation hard particle detectors operating in harsh environment of irradiations [100-105]. To support the sufficient charge collection efficiency within a detector volume, the rather thick layers of detector base region should be used in design of the diode type particle detectors. Also, the large resistivity material is desirable to form the active area of the particle detector. Significant problems appear in formation of junctions and electrodes on GaN [106] caused by contamination with metals during metallization and due to their interplay with the intrinsic grown-in defects of high density. Up-to-now, rather high density of dislocations is inherent for GaN layers grown by MOCVD technology. Thereby, dislocation nets may introduce the disorder inherent carrier transport and recombination effects [88]. The disorder can be a reason for the stretched-exponent relaxation (SER) type transients [88, 101, 102, 106-109] in both photoconductivity (PC) and PL decay. These phenomena are often accompanied by the persistent photoconductivity [107, 108] barrier mediated carrier trapping [88], and photoconductivity quenching [107] effects. These effects [101, 102, 107-109] and interpretation of the photoluminescence spectral bands [101, 102, 107-110] are commonly considered on the basis of the point defect analysis by including the defect transforms in configurational space [107], temperature dependent changes of trap activation energy [109] and carrier decay lifetime, extracted from the SER fits of the experimental time resolved PL and PC transients [107-109]. However, existence of the disorder inherent PL and PC effects necessitates clarifying of the role of carrier transport and capture dynamics. In MOCVD grown GaN epi-layers, averaged density of dislocations exceeds values of 10^8 cm^{-2}, therefore their role cannot be ignored in analysis of the barrier associated carrier capture, the radiative recombination transitions involving dislocation cores ascribed deep levels [94], the space charge regions surrounding dislocation cores, and the dislocation nets caused carrier random-walk diffusion-limited [111] carrier transport and trapping effects.

The aim of this investigation was to study the MOCVD grown GaN on sapphire substrates epi-layers of different thickness in order to clarify the role of surface recombination, to separate the impact of the radiative and non-radiative recombination parameters and the disorder factors. The time and spectrum resolved contactless methods of the PL and MW-PC were combined for the synchronous measurements in order to control a performance of the radiative and non-radiative recombination channels.

6.1. Photoluminescence and photoconductivity transients

The MW-PC and PL transients have been synchronously measured in these experiments by collecting a response of the same UV (354 nm) excitation beam spot, generated by a micro-chip laser STA-1-TH employed for the pulsed (500 ps) excitation of the excess carriers. The excitation density is varied by spectrally neutral optical filters in the range of 0.001–2 $\mu J/cm^2$. The MW-PC response has been detected by using a coaxial needle-tip probe and a near field probing regime. The MW probed photoresponse signal is transferred to a digital 1GHz oscilloscope Tektronix TDS-5104, equipped with a computer, where MW-PC transient is displayed and processed. The PL light is collected from the area with normal directed towards a bisector between the incident and the reflected UV light beams. The UV filtered PL light is focused onto a slit of a Jobin Yvon monochromator. The PL light is dispersed using a grating within the monochromator, and the PL pulsed signal is detected by a Hamamatsu H10721 photomultiplier. This PL signal is also transferred to another channel of the digital oscilloscope TDS-5104, where the PL transient is displayed and processed together with MW-PC transient.

The initial photoconductivity decay component appears in the same time domain relative to the radiative recombination kinetics in GaN layers (Fig. 6.1). Duration of the U_{PL} decay comprises $\tau_{r,i}\approx 2.3$ ns evaluated within a relaxation stage of the PL transient at a level exp(-1)≈0.368 of the normalized amplitude of PL signal.

Therefore, to distinguish the carrier decay rates ascribed to the microcrystals (where UV-PL is the most efficient) and the periphery surrounding the monocrystalline volumes, a subtraction procedure (illustrated in Fig. 6.1) for the normalized PL and MW-PC signals can be applied for a rough primary estimation of the impact of radiative (*r*) and non-radiative (*nr*) channels. The overlapped components of carrier decay through the radiative and non-radiative recombination within a system of distributed parameters are mediated through carrier diffusion. Then, MW-PC signal (which amplitude $U_{MW\text{-}PC}$ is proportional to the excess carrier density *n,* i.e. $U_{MW\text{-}PC}{\sim}n$) can be approximated by synchronous linear (non-radiative $\sim n$) and non-linear (radiative $\sim n^2$) processes. In this case, a decay of the excess carrier density in time *t* is generally described by continuity equation

$$\frac{\partial n}{\partial t} = D\frac{\partial^2 n}{\partial y^2} - \frac{n}{\tau_{nr}} - \gamma n^2 \tag{6.1}$$

with parameters of the carrier diffusion coefficient *D* along spatial coordinate *y*, of the characteristic time of non-radiative decay τ_{nr}, of the coefficient γ of radiative recombination using relevant boundary conditions (e.g. of a type $D\partial n/\partial y|_{y0}=sn$) on surface ($y=y_0$ with surface recombination velocity *s*). The continuity equation can be solved analytically only at approach of the instantaneous decay time $\tau_{r,i}=1/\gamma n$ for radiative recombination. Solution of this equation can be approximated by a sum

$$n(t) = n(t=0)\sum_{mi} A_m \exp[-(\frac{\eta_m^2 D+1}{\tau_{nr}})t]\exp[-(\frac{1}{\tau_{r,i}})t_i] \tag{6.2}$$

over the spatial frequencies [62, 128, 129] η_m and instantaneous lifetimes $\tau_{r,i}$. Replacing the sum by an integral averaged over duration $\tau_{MW\text{-}PC}$ of the MW-PC decay and keeping in mind linearity of the detection regime ($U_{MW\text{-}PC}{\sim}n(t)$), the MW-PC transient can be described (through normalized, -subscript *norm*, amplitudes of the non-radiative (*nr*) and radiative (*r*) recombination components) by expression

$$U_{MW-PC}(t) \approx \frac{U_{MW-PC}}{\tau_{MW-PC}}\int U_{nr,norm}(t)U_{r,norm}(t-\Theta)d\Theta\,. \tag{6.3}$$

Assuming $U_{r,norm} \approx U_{PL,norm}$ and $U_{MW\text{-}PC,0} = U_{MW\text{-}PC}(t\text{-}\Theta=0)$, the differential MW-PC component ascribed to the non-radiative decay

$$U_{MW-PC,nr}(t) = U_{MW-PC}(t=0) - \frac{U_{MW-PC,0}}{\tau_{MW-PC}} \int U_{nr,norm}(t) U_{PL,norm}(t-\Theta) d\Theta \tag{6.4}$$

leads to an approach:

$$\begin{aligned} U^{s}_{MW-PC,nr}(t)\} &= \frac{1}{\tau_{MW-PC}} \int_0^t [1-U_{PL}(\Theta)] U_{MW-PC}(t-\Theta) d\Theta \approx \\ &\approx \frac{1}{\tau_{PL}} \int_0^{\tau_{PL}} [1-U_{PL}(\Theta)] U_{MW-PC}(t-\Theta) d\Theta + U_{MW-PC}(t>\tau_{PL}) \end{aligned} \quad . \tag{6.5}$$

The obtained differential signal is shown by stars in Fig. 6.1. This differential signal $U^{s}_{MW\text{-}PC,nr}$ (a residual MW-PC signal) can then be attributed to the peripheral areas of a multi-crystalline material. The elimination ($U_{MW\text{-}PC}$ -U_{PL}) of this PL decay component from the integral MW-PC signal ($U_{MW\text{-}PC}$) leads to a decrease of the initial amplitude of the normalized ($U^{s}_{MW\text{-}PC} \sim U_{MW\text{-}PC}$ -U_{PL}) component. This $U^{s}_{MW\text{-}PC}$ component coincides with MW-PC transient after UV-PL signal disappears (within a linear scale). This result implies that the micro-volumes within a multi-crystalline GaN layer coincide (for which the MW-PC and PL signals are synchronously collected and exhibit the fast decay components in MW-PC and PL transients). Thus, it can be assumed that the slower (than $\tau_{r,i}$ in U_{PL}) MW-PC initial component $U^{s}_{MW\text{-}PC}$ is ascribed to the stretched-exponent decay, and it appears due to carrier brought to a periphery of the monocrystalline micro-volumes (columns) within a GaN epi-layer. The dislocations are namely located within these periphery areas surrounding the crystalline columns. The excess carriers, brought to the periphery areas with space charge regions within Cottrell spheres/cylinders of dislocations, are separated by the space charge field.

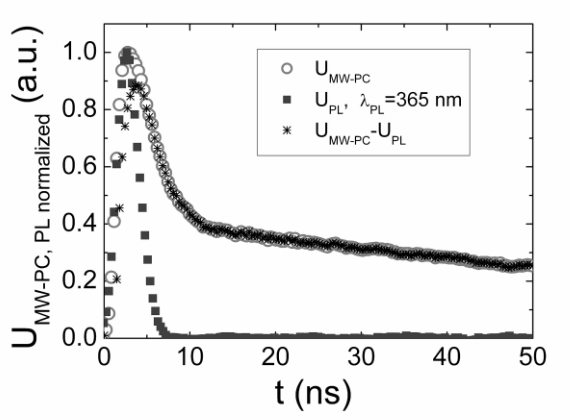

Fig. 6.1. The MW-PC decay transient displayed within an initial stage of the MW-PC signal relaxation compared with a simultaneously registered PL transient at 365 nm PL wavelength in the 5.6 μm thick epi-layer.

Thus, the excess carrier recombination is only mediated by carrier diffusion, caused by the excess carrier density gradients. Thereby, these different (fast and slow) carrier decay components should be ascribed to the different micro-areas of the epi-GaN material. To collect the MW-PC and PL signal from the same excited volume (where the lateral micro-inhomogeneity of material is inevitable), the synchronous detection of the MW-PC and PL responses is necessary in order to highlight the impact of the radiative and non-radiative carrier decay. The transient MW-PC signals, integrated over the excited area, contain the overlapped components of carrier decay through the radiative and non-radiative recombination.

The initial component of the MW-PC transients is in the same time scale as that of the PL transients measured for the different PL wavelengths (Fig. 6.2). A reduction of the UV excitation intensity leads to a decrease of the amplitude of the asymptotic component within the MW-PC transients. This can be understood as the potential barrier mediated carrier trapping [88]. The reduction of the excitation intensity also leads to a shortening of the initial MW-PC decay component as illustrated in Fig. 6.2a. This hints a decrease of the impact of the radiative recombination (PL) within the MW-PC signal, as a rather small excess carrier part decays through the radiative channels, due to a limited efficiency of the PL. This simultaneously indicates an increase in the role of carrier trapping centres. The carrier trapping processes are however mediated (limited) by diffusion [88, 89], for a small density of the mobile carriers in the disordered peripheral areas of the multi-crystalline material. The barrier and diffusion limited trapping [88, 89] leads to the long (in a millisecond time scale), non-exponential relaxation of the MW-PC signal (Fig. 6.2a).

The UV-PL (exciton attributed) intensity follows a reduction of the UV excitation density. However, the reduction of the UV excitation intensity causes an enhancement of the Y-PL amplitude and asymptotic component duration, as can be inferred from Fig. 6.2b. Nevertheless, the measurable Y-PL signal can only be obtained in the scale of hundred microseconds in the time resolved PL at wavelengths $\lambda_{PL}\geq525$ nm. Additionally, the long tail PL relaxation component weakens for the shorter wavelength PL, $\lambda_{PL}<500$ nm (Fig. 6.2c). These observations can be understood at assumption that the non-linear, barrier mediated carrier trapping centres (associated with the non-exponential MW-PC relaxation) could be related to the B-PL radiative recombination. A reduction of excitation density leads to an enhancement of the barrier and to the decrease of the asymptotic component within the MW-PC transients. The B-PL radiative recombination channel governs then the excess carriers involved into the space charge region which surrounds a dislocation core, if B-PL can be attributed to the radiative recombination through the deep levels ascribed to the dislocation core. At this assumption, the intensity of B-PL radiative recombination is weakly dependent on excess carrier density, provided the excitation density is insufficient to considerably modify the potential barrier ascribed to a dislocation. Consequently, a competing channel, as the sub-system levels of the D-A type point defects ascribed to the Y-PL radiative recombination [110], becomes a prevailing one.

These traps seem to be located in the periphery of the micro-crystals, and the carriers, brought to a micro-crystal boundary by diffusion, determine the component of the fast Y-PL decay. The impact of carriers photo-generated in the micro-crystals is thereby reduced within the entire Y-PL signal with a decrease of excitation intensity (Fig. 6.2b). The role of the Y-PL centres localized at surface of a micro-crystal is equalized to influence of those existing in the periphery of the micro-crystals, for the small density of the photo-excited carriers. Then, the relative impact of the Y-PL centres located in the periphery of the micro-crystals increases with reduction of excitation density, and this leads to the enhancement of the relative amplitude of the Y-PL and stretched-exponent type relaxation. The latter SER trapping process is governed and limited by random-walk of small density mobile carriers in the disordered peripheral areas.

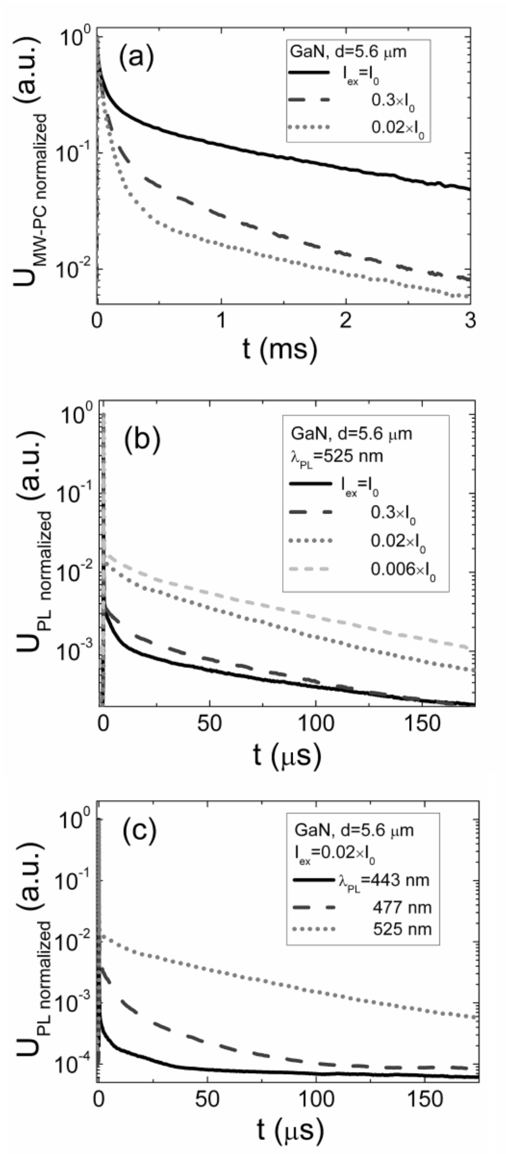

Fig. 6.2. The MW-PC transients (a) and PL decay transients at 525 nm wavelength (b) measured varying excitation intensity and luminescence wavelength (c) in 5.6 μm thick GaN epi-layer.

6.2. Photoluminescence spectral characteristics

The registered PL amplitudes (extracted from the PL transients dispersed at fixed wavelength) as a function of the PL quantum energy ($h\nu$) are plotted in Fig. 6.3. Several PL bands can be resolved within a PL spectrum: namely, the exciton ascribed UV-PL band appearing for $h\nu$>3.3 eV, the defects attributed bands of blue B-PL (for 2.5<$h\nu$<3.0 eV) and the yellow Y-PL (with $h\nu$<2.4 eV). These PL bands are well examined [110, 115-121] thereby our spectroscopy results correlate with literature data. It can be deduced from the comparison of these spectra measured at different excitation densities that the intensity of the UV-PL band increases with excitation density, while the intensity of B-PL band is nearly invariant, but the intensity of the Y-PL increases with reduction of excitation density.

This clearly indicates that the role of the Y-PL is enhanced with reduction of the excess carrier density, and it can be associated with the carrier trapping centres, being a sub-system of D-A radiative recombination, interpreted in detail [110]. Carrier trapping centres, as usual, act together with the recombination ones. For the large initial excess carrier density within conduction/valence band, the main carrier capture flow runs through the deep recombination centres, while the shallower trapping centres are being filled with excess carriers. During these processes, the density of excess carriers in conduction band can become either an equal or smaller relative to that of the shallow trapping centres. Then, the recombination process proceeds on a support of the carriers thermally generated from the trapping centres. A reduction of the initial excess carrier density (being proportional to the excitation intensity) highlights the impact of the trapping centres in PL transients. The trapped carriers can proceed their existence either being thermally released to conduction band or captured to the deeper centre. The latter process is then responsible for the D-A radiative recombination. Such the scenarios can be ascribed to the Y-PL behaviour in our observations by correlating results on PL and MW-PC transients. These results are in the qualitative agreement with literature data [115-121].

The B-PL band is also interpreted [110] as the D-A transitions ascribed to the defects of different origin (relative to Y-PL). In our experiments, the nearly invariant intensity of the B-PL band transients has been obtained when changing the excitation density. Therefore, the PL spectra (in Fig. 6.3) were normalized to peak amplitude of the B-PL band. The spectral position of the B-PL peak is also stable and independent of the epi-layer thickness, while an appearance of the UV-PL and Y-PL depends on layer thickness.

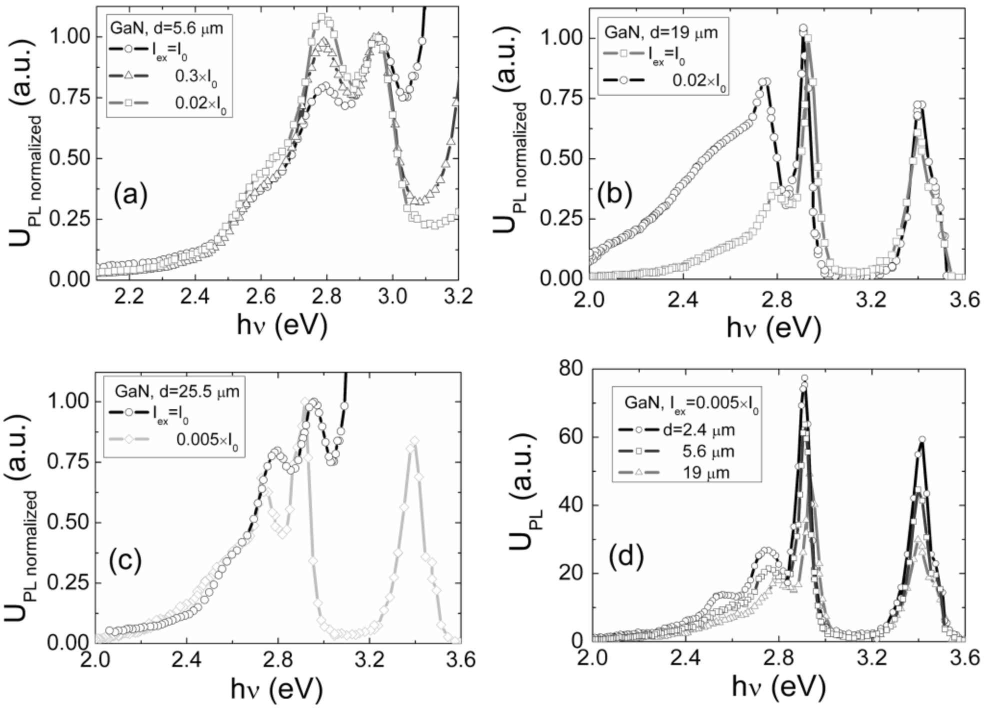

Fig. 6.3. Spectral variations of the normalized amplitude of the PL transients measured at different excitation densities on different thickness (*d*) GaN samples: (a) *d*=5.6 μm; (b) *d*=19 μm; (c) *d*=25.5 μm; (d) at fixed I_{ex} for *d*=2.4, 5.6 and 19 μm.

The changes of the UV-PL intensity relative to that of B-PL in rather thick layers can be explained by the re-absorption effect for PL radiation wavelengths close to the threshold of interband transitions. The B-PL intensity increases slightly with excitation density irrespective of the epi-layer thickness (Fig. 6.3d), while the intensity of the UV-PL and Y-PL (Figs. 6.3a – 6.3c) changes considerably and non-linearly with excitation intensity in epi-layers of different thickness. The absolute values of the B-PL intensity decrease with an increase of the epi-layer thickness, which is in agreement with reduction of TDD (Table 3.3), reciprocally dependent on layer thickness. For fixed excitation intensity (Fig. 6.3d), the density of defects, responsible for both the Y-PL and B-PL, decreases with enhancement of the epi-layer thickness. This implies that quality of the epi-layer improves with increase of layer thickness.

The time and spectrum resolved changes of the B-PL, being different from that of Y-PL, hint on different origin of these B-PL defects. The main candidate, as a B-PL centre, would be dislocations, which are inevitable even in the rather thick MOCVD-grown GaN layers [94].The interpretation [110] of the B-PL through the D-A type recombination is not contradicted in this approach. Here, the D-A system could be understood as the dislocation core ascribed levels. The relative stability of the B-PL would be in good agreement with the dislocation core ascribed D-A transitions, where variation of dislocation density with epi-layer thickness can be assumed rather small for the identical growth regime.

6.3. Recombination parameters and their relation with material structure

Complicated redistribution of excess carriers among the radiative and non-radiative recombination centres in GaN layers has been revealed by the combination of the MW-PC and PL transient techniques. The observed two-componential MW-PC transients imply the non-exponential carrier decay process. A linearization of these residual MW-PC (after subtraction of the PL inherent component) transients is only possible using the stretched exponent approximation [88, 90, 92]. This approximation yields to a description of excess carrier density variations in time expressed as in (5.3), where α is a fractional index which is associated with material disorder characteristics [88, 90, 92]. Fractional index is evaluated from a linear fit of the double logarithm of the normalized transients (Fig. 6.4) displayed on the logarithm time scale ($\ln(-\ln(U(t)/U(0)))$ versus $\ln(t)$) [90, 92].

A rather good linearity of the normalized MW-PC signals approximated by a stretch-exponent is obtained (Fig. 6.4a) over a wide range of running time (form ns to ms) within a transient. The linearity is reached for the epi-layers of different thickness. However, the slopes of these lines in the plots are different.

The slope increases with a thickness of epi-layer (Fig. 6.4b). This slope correlated with α can be associated with the fractal index [89, 90, 92]. The approach of α to unity implies a reduction of the disorder of material. Thereby, the crystalline structure slightly straightens up with enlargement of the thickness of GaN epi-layer over 15 μm. This result is in agreement with a reduction of the Y-PL intensity correlated with an increase of the epi-layer thickness (Fig. 6.3d).

Variation of the fractal index of an epi-layer (Fig. 6.4) is also correlated with the relative amplitude of an asymptotical component in the MW-PC transients (Fig. 6.5a) represented as a function of epi-layer thickness. The larger the relative amplitude of the asymptotic decay component is, the larger fraction of the excess carriers is involved into a random-walk/trapping within the inter-crystalline area, and the less fraction of the excess carrier density recombines in the micro-crystal volume. The relative amplitudes of the asymptotical component in the MW-PC transients obtained in the same thickness (2.5 μm) epi-layers (grown by using VU and TU MOCVD reactors) is compared in Fig. 6.5a. It can be deduced that nearly the same quality of the GaN epi-layer is obtained if the growth regime is similar. However, the crystal quality is reduced under deviations from the optimal growth temperature regime. The stretch-exponent component within MW-PC transients correlates with manifestation of the traps responsible for the PL, - such a correlation can be deduced from comparison of the excitation intensity dependent changes of amplitudes of the asymptotic component in the MW-PC and PL transients, Fig. 6.2, and Y-PL transients, shown in Figs. 6.2b and 6.5b.

For thin epi-layers, the impact of the surface recombination should always be evaluated. In the dislocation-rich thin samples, the surface recombination can be significant due to several reasons: i) the recombination on layer surfaces, ii) the recombination on dislocations cylinders (threading dislocations prevail), iii) the surface recombination on boundaries of a micro-crystal. The surface recombination on the epi-layer interface/surface should be dependent on layer thickness d. Assuming the un-matched crystal cell constant at the interface between the GaN and sapphire, the largest surface recombination velocity s→∞ could be ascribed to this interface. For rather large surface recombination velocity, the recombination is limited by carrier diffusion to this interface. The shortest effective carrier decay lifetime τ_D is then evaluated as $\tau_D = d^2/\pi^2 D \cong 1–125$ ns for the entire range of layer thicknesses examined. Here, $D \geq 5$ cm^2/s is the coefficient of the carrier diffusion (estimated using the mobility values in Table 3.3). The square symbols in Fig. 6.6 represent the simulated τ_D values calculated for the epi-layers examined as a function of layer thickness.

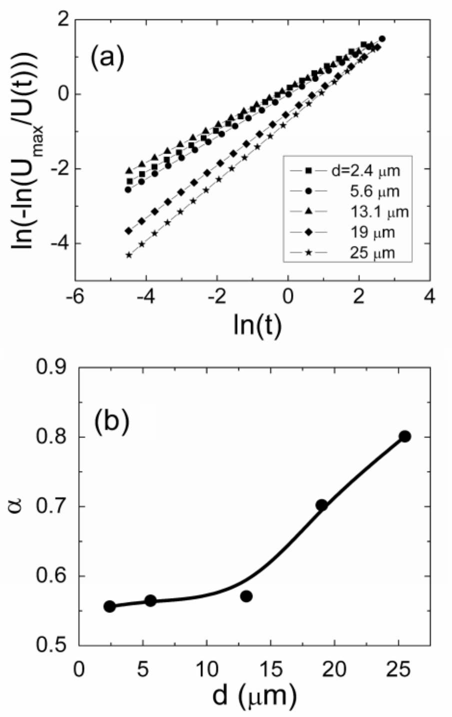

Fig. 6.4. Evaluation of the fractional index α by linearization of the normalized MW-PC transients at $I_{ex} \cong I_0$, ascribed to the non-radiative recombination (a), and variation of the fractional index as a function of epi-layer thickness (b).

It can be noticed that the specific lifetime values cover the time scale from 1 ns to hundreds of ns, measured at low excitation (pulsed) level $n/n_0<1$ (where excess carrier density n is significantly lower than equilibrium carrier density $n_0>3\times10^{16}$ cm^{-3}, i.e. $n<<n_0$). However, the inherent lifetime values measured by MW-PC technique show the significantly longer characteristic times. Additionally, any clear dependence of the MW-PC decay on the epi-layer

thickness was not revealed. The surface recombination on micro-crystal boundaries (which size can also be represented through $d=\phi$, with ϕ a diameter of a micro-crystal) can also be estimated by assuming very rapid surface recombination and using τ_D. The probable value of a diameter of the micro-crystals should be less than the thickness of a layer. Then, the simulated τ_D dependence on d is represented by a solid line in Fig. 6.6.

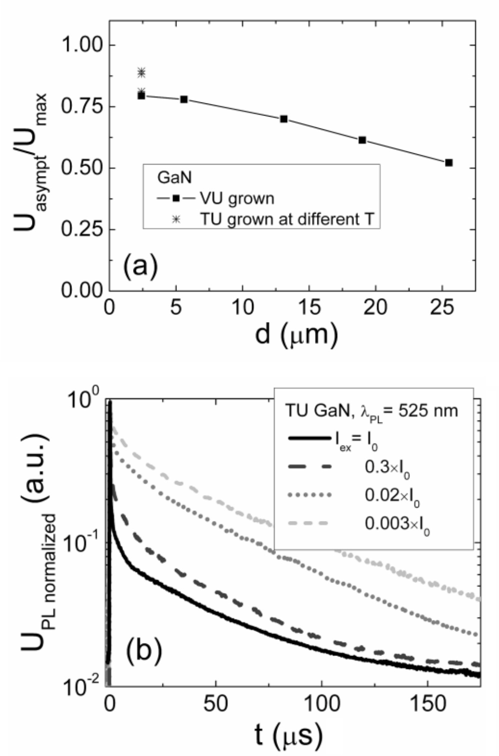

Fig. 6.5. a - Ratio of the amplitude of the asymptotic component in the MW-PC transient to peak amplitude of the residual MW-PC response as a function of an epi-layer thickness for $I_{ex}\cong I_0$. b - Variation of the Y-PL transients dependent on excitation density in the 2.4 μm thick GaN 1047 sample.

It can be deduced from this dependence that the characteristic τ_D times should be shorter than 10 ns for the layers investigated. This is in good agreement with a range of the measured decay lifetimes for UV-PL and B-PL. Thereby, it can roughly be inferred that UV-PL is limited by the size of micro-crystals and the surface recombination on their boundaries, while B-PL is determined by the carrier (from the inter-crystalline area) recombination on the dislocations. For the recombination on the dislocations, the effective length $\Delta_{dislocation}$ can be estimated using a probable surface density N_{disl} of dislocations and assuming their nearly homogeneous (integrally) distribution, as $\Delta_{dislocation}=N^{1/2}_{disl}$. A diameter of dislocation is determined by space charge region surrounding it. In reality, this diameter can reach a measure of about 1 μm. Thereby the largest density of dislocations is also limited, even for the compact deployment of micro-crystals and surrounding dislocations. The probable τ_D range due to $\Delta_{dislocation}$ changes is again represented by a solid line in Fig. 6.6. Values of τ_D~1-10 ns correlated with N_{disl}~10^8–10^{10} cm^{-2} (Table 3.3) agree with the experimentally observed range for the B-PL and the initial component of the MW-PC transients.

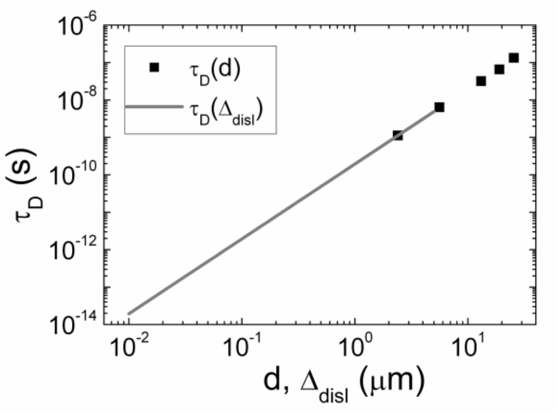

Fig. 6.6. Simulated lifetime (τ_D) of the diffusion limited surface recombination as a function of the epi-layer thickness (d) and of the effective distance ($\Delta_{\mathrm{dislocation}}$) between the dislocations.

By concluding the results, discussed in Sections 6.1-6.3, it can be inferred that normalized MW-PC transients enabled us to distinguish the carrier decay components associated with carrier decay within micro-crystals and the disordered structure on the periphery areas surrounding crystalline columns. This examination combined with analysis of the PL spectral and temporal changes allowed for attribution of the trapping component, revealed in MW-PC transients, to the yellow Y-PL band in the range of $h\nu$<2.4 eV. It has been obtained that intensity of UV-PL band increases with excitation density, while intensity of B-PL band is nearly invariant. The B-PL has been ascribed to carrier recombination on the dislocation cylinder surfaces. Fractional index α with values $0.5<\alpha<0.8$ was evaluated for the stretched-exponent component which fits the experimental transients determined by the disordered structure ascribed to the periphery areas surrounding the crystalline columns.

6.4. In situ variations of photoconductivity and luminescence

This work is addressed to the study of the efficiency of proton induced steady-state photoluminescence. To evaluate the density of the high energy proton induced excess carriers, a correlation between the MW-PC transients and the PI-L intensity has been examined. The proton energy range (1.6 MeV) has been chosen to implement the nearly homogeneous and rather strong excitation of the 2.5 μm thick GaN epi-layers. To estimate radiation hardness of such material, evolution of MW-PC and PI-L characteristics has been studied by the in situ measurements of the changes of PI-L intensity and MW-PC decay rate during exposure to a proton beam reaching fluences up to 10^{15} cm^{-2}.

The 2.5 μm thick GaN epi-layers [88, 105] MOCVD grown on sapphire substrate have been examined. Dislocation density in these epi-layers was evaluated to be of about 10^{10} cm^{-2}. The measurements were implemented similarly to those performed on CdS material, described in Section 5. The photoluminescence spectra and photoconductivity transients were initially examined to calibrate densities of the photo-excited excess carriers and luminescence (L) intensity using various regimes (time resolved, - TR-L and steady-state S-L) of luminescence recording. The TR-L and S-L spectra and MW-PC transients have been simultaneously recorded in these calibration measurements. The transient signals of the MW-PC and TR-L/S-L have been measured by collecting a response to the same UV (354 nm) excitation beam spot (of an area of 8×10^{-3} cm^{2}), generated by a micro-chip laser STA-1-TH employed for the pulsed (of 500 ps duration and 100 Hz repetition rate) excitation of the excess carriers. The MW-PC response has been detected by using a coaxial needle-tip probe and a near field probing regime. The UV filtered TR-L light is focused onto a slit of a Jobin Yvon monochromator. The TR-L light is dispersed using a grating within the monochromator, and the TR-

L signal is detected by a Hamamatsu H10721 photomultiplier. This TR-L signal is also transferred to another channel of the digital oscilloscope TDS-5104, where the TR-L transient is displayed and processed together with MW-PC transient. The laser induced luminescence spectra registered by a signal integration regime (LS-L) have complementarily been registered by employing a spectro-photometer Avantes AvaSpec-2048TEC equipped with a fiber adjusted input. The LS-L light has been transferred to the photometer input slit using a fiberscope with an aperture area of 8×10^{-3} cm^2.

For the in situ measurements, the sample has been mounted on a cold finger within a specially fabricated irradiation chamber, described in Section 2.7. Protons were accelerated to 1.6 MeV by using the Tandetron 4110A ion accelerator. The MW-PC and quasi-steady-state PI-L signals have been synchronously recorded during exposure to a proton beam of a spot area of 0.2–0.8 cm^2. One of the issues analysed in this research was to correlate the changes of non-radiative recombination properties with radiative recombination channels under radiation damage by high energy protons. The thickness of epi-layers and the energy of protons have been chosen on the basis of the initial simulations made by TRIM [124]. It can easily be verified by the TRIM simulations that stopping range of the 1.6 MeV protons significantly exceeds a thickness (d=2.5 μm) of the GaN epi-layers employed. This determines a nearly homogenous energy loss of a proton beam during interaction of protons with GaN material. Contrarily, the optical excitation at 345 nm wavelength determines the initially inhomogeneous excitation due to a large absorption coefficient β=4.7×10^4 cm^{-1} [125].

The distribution of the excess carriers acquires the stabilized in-depth profile only after diffusion time $t_D \cong d^2/D$=63 ns (estimated using approximation $d\cong(Dt_D)^{1/2}$) overwhelming the layer thickness d. Here, $D\cong1$ cm^2/s is the coefficient of carrier ambipolar diffusion in GaN. The transitional process of the profile equilibration can also be implied to be a reason of the fast initial component within transients of photoconductivity decay and TR-L of duration of ~10 ns. As it was shown in Refs. [88, 105], the MW-PC asymptotic decay component of durations in a millisecond time scale obeys $(U_{MW-PC}(t) = U_{MW-PC}(t=0)\exp[-(\frac{t}{\tau_{SE}})^{\alpha})$ the SER law interpreted through a disorder of material. Here, $U_{MW\text{-}PC}(t)$ is the change in time (t) of the amplitude of the MW-PC signal; τ_{SE} is the characteristic time ascribed to the SER process approximated using SER with index α [90, 92]. The disorder in the as-grown GaN epi-layers can be related to the dislocation networks at the prism type crystallites which are twisted to each other by a certain angles [126]. Thereby, the in situ control of the changes of recombination properties of GaN layer has been addressed to analysis of the α changes (Fig. 6.7). α values are extracted using a routine plot (inset i_2 in Fig. 6.7) in SER analysis [96, 98]. It can be deduced from Fig. 6.7 that the α value decreases with the enhancement of proton fluence (Φ) in the range of $\Phi > 10^{13}$ cm^{-2}. Reduction of α value indicates an increase of the disorder degree in the GaN material and the re-arrangement of structure of the grown-in defects induced by radiation defects (where recombination of primary radiation defects can be a reason of local recombination induced annealing effects [127]).

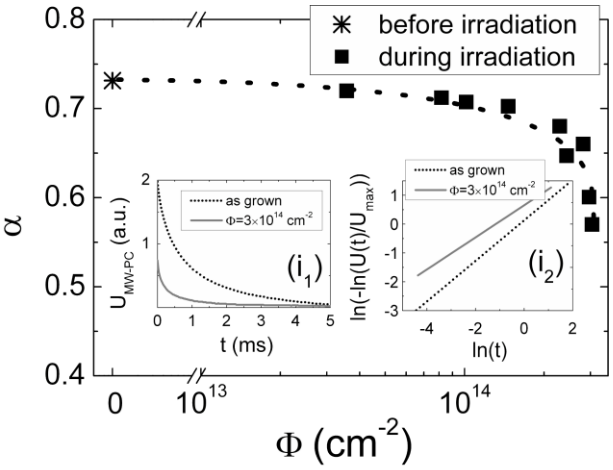

Fig. 6.7. Variation of the SER index dependent on irradiation fluence measured in situ. Inset i_2 represents a traditional plot employed for analysis of MW-PC transients illustrated within inset i_1 for evaluation of SER index of carrier decay in the non-irradiated and proton irradiated GaN.

An area (A_L=8×10^{-3} cm^2) of laser spot and of MW needle-tip probe were significantly less than a proton beam spot area A_P=0.2-0.8 cm^2. Thereby simultaneous in situ measurements of MW-PC transients and S-L spectra can be implemented during proton irradiation. The proton induced S-L signal was collected by a multi-fiber probe of a total area of A_{pr}=3×10^{-2} cm^2 separated from a laser beam location within proton beam spot. In Fig. 6.8a, the S-L spectra excited by a laser pulse of a total energy of E_{L}=0.14 μJ at 354 nm wavelength and by a 1.6 MeV proton beam (at a very initial stage, 1 sec, of irradiation) of i_P=26 nA current are compared. This comparison has been employed to evaluate the initial excess carrier density excited by protons and to relate it to the yellow-green S-L induced by protons.

The gray curve in Fig. 6.8a represents the 6 time magnified amplitude of a LS-L spectrum excited by a laser pulse to fit the intensity of the yellow-green luminescence (YG-L) band of the proton excited the same band S-L in GaN layer. From the latter fit, the average of excess carrier density generated by a proton beam can be evaluated through calibration of the laser pulse parameters and the absorption coefficient β at laser light wavelength. To increase evaluation precision, the inhomogeneity of laser excitation and the time-integration of S-L signal should be included into this fitting procedure. The density n_0 of excess carriers photo-generated by laser is evaluated by relation $n_0=\beta E_{\mathrm{L}}/A_L E_1$ using the E_{L} fixed in calibration measurements, the area A_L of a laser beam spot, and a quantum energy E_1=3.5 eV with a unit efficiency of carrier pair production at 354 nm wavelength. The depth averaged

$$< n_L >_d = n_0 \frac{1}{d}\int_0^d e^{-\beta x} dx = \frac{n_0}{\beta d}(1-e^{-\beta d}) \cong 1.3\times 10^{17} cm^{-3} \qquad (6.6)$$

carrier density can then be equalized with excess pair density n_P generated homogeneously in d by penetrative protons. The equivalent density n_P of excess carrier pairs generated by protons would be equal to $<n_L>$ if time of signal integration coincides with t_D. It has been obtained by equalizing the YG-L intensities (Fig. 6.8a) that integrated density $n_P t_D$ exceeds that $<n_L> t_D$ by about 6 times. This observation is in good agreement with the calculated value of this ratio if a UV pulse induced TR-L transient with initial TR-L decay time $\tau_{YG\text{-}L}^{in}$~10 ns is taken into account for YG-L band, - the spectro-photometer integrated signals over t_D=63 ns are related as

$$n_p t_D = < n_L > \int_0^t \exp[-\frac{t}{\tau_{Y-GL}}]dt = < n_L > t_D \frac{\tau_{Y-GL}}{t_D}. \qquad (6.7)$$

For longer integration times, the instantaneous TR-L decay time in asymptotic $\tau_{YG\text{-}L}^{as}$~50 µs is employed to correlate the n_P and $<n_L>$ values. A quantity of carrier pair generation by a single 1.6 MeV proton can be estimated by independent evaluation of a flux of protons using values of the proton beam current i_P and the beam area $A_P=2\times10^{-1}$ cm^2. The flux of protons is then obtained as $F_P=i_P/eA_P\cong8\times10^{11}$ cm^{-2}s^{-1} with $e=1.6\times10^{-19}$ C the elementary charge of proton. Then, it is estimated a quantity of protons $N_P=F_P\tau_{L\text{-}av}A_P\cong1.6\times10^9$, which cross the GaN layer d and correspond to the YG-L signal integration time $\tau_{L\text{-}av}$=10 ms for a single laser pulse. The efficiency κ_P of a single proton generation is obtained to be $\kappa_P=n_P/N_P\cong1.3\times10^7$ cm^{-3} per proton or $\kappa_P A_{pr}$=40 carrier pairs per a micrometer of layer depth per proton.

This $\kappa_P A_{pr}$=40 µm^{-1}p^{-1} value is close to those values for wide-gap materials, listed in Ref. [98]. However, the evaluated 40 µm^{-1}p^{-1} value for the investigated GaN layers is about twice less than value of $\kappa_P A_{pr}$ published [98] for GaN material, structure of which can be different [128] from the studied in our experiments and different energy of protons had been used[17] for evaluation of $\kappa_P A_{pr}$.

Several TR-L and S-L bands (Fig. 6.8a) can be resolved within both the laser and the proton induced spectra, - namely, the ultra-violet (UV-L) and blue (B-L) bands in the range of wavelengths 350-430 nm, the green-yellow (YG-L) S-L peaked at 560 nm and the red-infrared (RIR-L) with a peak in the range of 710 nm are resolved. For PI-L, a rather sharp peak appears at 700 nm. It has been clarified that this latter PI-L peak should be ascribed to the proton excited luminescence of the sapphire substrate. This PI-L peak at 700 nm has been eliminated from the further consideration of PI-L spectra in GaN layer. The UV-/B-L and YG-L bands are well-known [105, 109, 110, 112, 129-133], and these luminescence bands are commonly ascribed to the growth defects in MOCVD GaN layers. Evolution of the PI-L intensity I_{PI-L} within resolved spectral bands is illustrated in Fig. 6.8b. It can be noticed that the fastest decrease of intensity is obtained for the YG-PI-L band with enhancement of fluence during irradiation exposure. The slower reduction of PI-L intensity is observed for the RIR-PI-L band with increase of exposure. Intensity of the UV-/B-PI-L bands is rather weak (Figs. 6.8a and 6.8b).

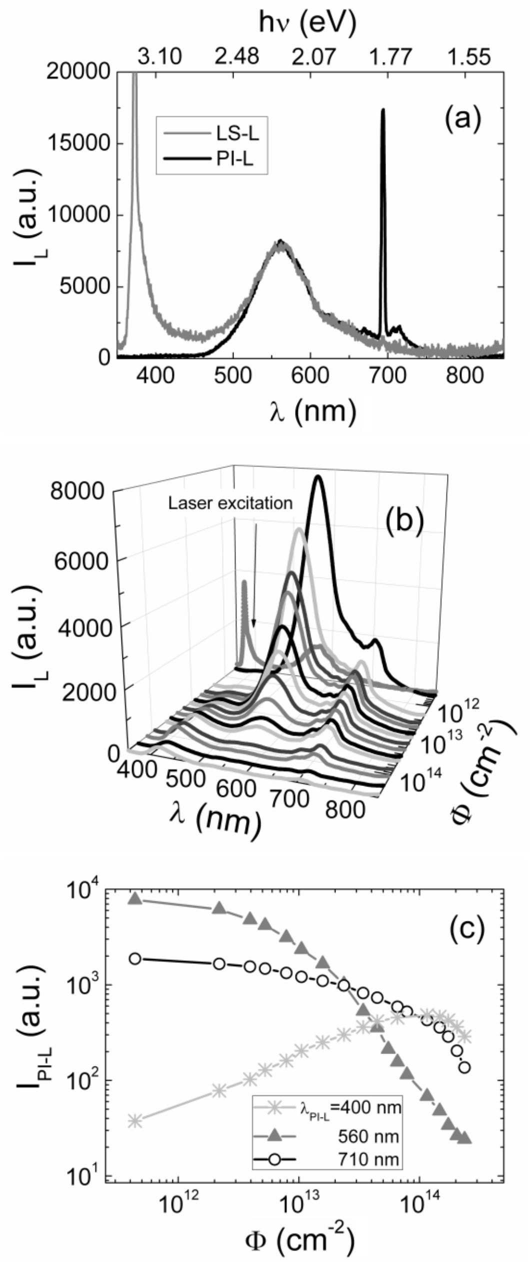

Fig. 6.8. a - Comparison of S-L spectra in the non-irradiated GaN layer recorded under pulsed laser excitation and those excited by a proton beam of very small fluence (the gray curve represents a magnified amplitude of a LS-L spectrum); b - evolution of PI-S-L spectra excited by a proton beam with irradiation fluence where a LS-L spectrum excited by a laser pulse is also shown; c - variation of peak intensity ascribed to different PI-S-L spectral bands as a function of irradiation fluence collected during exposure to the 1.6 MeV proton beam.

It can be deduced from Fig. 6.8c, where evolution of peak intensities of PI-L is represented, that both the intensity of the YG-PI-L and RIR-PI-L bands clearly decreases with enhancement of the proton irradiation fluence. While, intensity of the blue-PI-L (B-PI-L) increases with exposure time to saturated/decreased values at the maximal fluences employed. The discussed observations in evolution of PI-L bands are in good agreement with the examined changes of PI-L spectra under optical excitation, performed by using the post-irradiation measurements [104, 105, 109, 110, 112, 129-133]. The YG-L and the RIR-L bands are commonly associated with randomly distributed point defects [109, 110, 112, 129-133]. The destruction of a net of these point defects should be inferred from the evolution of PI-L bands. This hypothesis [104, 105] is corroborated by the clearly observed increase of the degree of disorder in GaN material (which can qualitatively be estimated from the changes of SER index α in Fig. 6.7) Alternatively to interpretations [109, 110, 112, 129-133] of the B-L origin, the B-PI-L can also be attributed to the dislocations of rather high density, which is more proof for the radiation destruction.

The defect introduction rate can be evaluated from the evolution of YG-PI-L reduction as a function of fluence. The YG-PI-L decrease can be explained through the reduced rate g_P of excess carrier generation $n_P=g_P\tau_{rd}$ by proton flux due to shortening of the carrier capture lifetime τ_{rd} via density of the radiation induced defects $N_{rd}=1/\sigma_{rd}\tau_{rd}v_T$ with the parameters of capture cross-section σ_{rd} and thermal velocity v_T. This PI-L intensity decrease is implied to be observable when τ_{rd} becomes shorter than $\tau_{PI\text{-}L}$, i.e. $\tau_{rd}<<\tau_{PI\text{-}L}$. The instantaneous lifetime of TR-L decay time in asymptotic ($\tau_{YG-L}{}^{as}$~50 μs) part for spectral range of YG-L, evaluated for the same non-irradiated GaN samples, hints that the observable density N_{rd} is in the range of $N_{rd0} \cong 2\times10^{11}$ cm^{-3}, assuming the typical values of $\sigma_{rd}\sim10^{-14}$ cm^{2} and $v_T\sim10^{7}$ cm/s. Using the clearly expressed fragment of a curve of changes of the YG-L peak values in Fig. 6.8c, the introduction rate $K_P=\Delta N_{rd}/\Delta\Phi\sim\Delta I_{YG-L}/\Delta\Phi$ of radiation defects is estimated to be $K_P\cong0.6$ cm^{-1}. This implies that proton irradiation determines both the creation of the specific radiation defects with rate of $K_P\cong0.6$ cm^{-1} and their production transforms the material structure by increasing its disorder, as deduced from the observed decrease of value of the stretched-exponent index (Fig. 6.7). The degree of disorder determines the character of carrier diffusion and trapping, thereby influencing a redistribution of carrier flows through radiative and non-radiative decay channels.

By summarizing the in situ measurement results it can be concluded that the combined examination of the evolution of parameters of the non-radiative recombination (implemented by the on-line measurements of MW-PC transients) and the radiative recombination (by recording the quasi-steady-state PI-L induced by protons) shows a correlation in decrease of signatures of the material disorder degree luminescence efficiency. Comparison of the luminescence spectra induced by a proton beam and by a laser pulse, enabled us to evaluate the efficiency of excess carrier generation by $\kappa_P=\langle n_P\rangle/N_P\cong1.3\times10^{7}$ cm^{-3} per 1.6 MeV proton and carrier pair generation within layer depth by $\kappa_P A_{pr}$=40 μm^{-1}p^{-1}. This $\kappa_P A_{pr}$=40 μm^{-1}p^{-1} value is close to values inherent for wide-gap materials [108]. These parameters indicate that GaN layers can be an efficient material for detection of protons by combining both the electrical measurements, using a proper thickness of detector layer with $\kappa_P A_{pr}$=40 μm^{-1}p^{-1} to reach resolvable charge collection signal, and scintillation detection, using rather fast photo-sensors, capable to integrate the PI-YG-L signals with $\kappa_P\cong10^{7}$ cm^{-3}p^{-1}. However, it has been obtained that the inevitable degradation of the material appears for proton irradiation fluences above 10^{14} cm^{-2}. The observed enhancement of the disorder degree with irradiation fluence seems to be equivalent to the increase of the material resistivity [134-138]. The calibrated reduction of the intensity of PI-L in the range of green-yellow luminescence can also be exploited for dosimetry of the hadron irradiations in rather wide range of fluences.

Summary of the chapter

[A6, A7, A9]

By concluding the results, discussed in Sections 6, it can be inferred that normalized MW-PC transients enabled us to distinguish the carrier decay components associated with carrier decay within micro-crystals and the disordered structure on the periphery areas surrounding crystalline columns. This examination combined with analysis of the PL spectral and temporal changes allowed for attribution of the trapping component, revealed in MW-PC transients, to the yellow Y-PL band in the range of $h\nu<2.4$ eV. It has been obtained that intensity of UV- PL band increases with excitation density, while intensity of B-PL band is nearly invariant. Fractional index α with values $0.5<\alpha<0.8$ was evaluated for the stretched-exponent component which fits the experimental transients determined by the disordered structure ascribed to the periphery areas surrounding the crystalline columns.

The in situ measurements, implemented by combining the examination of the evolution of parameters of the non-radiative recombination and the radiative recombination show a correlation in decrease of signatures of the material disorder degree and the luminescence efficiency. Comparison of the luminescence spectra induced by a proton beam and by a laser pulse, enabled us to evaluate the efficiency of excess carrier generation by $\kappa_P=<n_P>/N_P\cong1.3\times10^7$ cm^{-3} per 1.6 MeV proton and carrier pair generation within layer depth by $\kappa_P A_{pr}=40$ $\mu m^{-1}p^{-1}$. This $\kappa_P A_{pr}=40$ $\mu m^{-1}p^{-1}$ value is close to values inherent for wide-gap materials. These parameters indicate that GaN layers can be an efficient material for detection of protons by combining both the electrical measurements, using a proper thickness of detector layer with $\kappa_P A_{pr}$=40 μm^{-1}p^{-1} to reach resolvable charge collection signal, and scintillation detection, using rather fast photo-sensors, capable to integrate the PI-YG-L signals with $\kappa_P \cong 10^7$ cm^{-3}p^{-1}. However, it has been obtained that the inevitable degradation of the material appears for proton irradiation fluences above 10^{14} cm^{-2}. The observed enhancement of the disorder degree with irradiation fluence seems to be equivalent to the increase of the material resistivity [134-138]. The calibrated reduction of the intensity of PI-L in the range of green-yellow luminescence can also be exploited for dosimetry of the hadron irradiations in rather wide range of fluences.

VII. Instrument VUTEG-5-AIDA for dosimetry of large fluence hadron irradiations

7.1. Principles and regimes of VUTEG-5-AIDA operation

Fast dosimetry of background irradiations within accelerator facilities, where large fluences are collected during rather short exposures, possesses the methodical and technical challenges. Different techniques, based on measurements of degradation of the electrical characteristics in heavily irradiated semiconductor devices or on control of products of nuclear reactions in metal foils, are anticipated to be applied within advanced dosimetry at accelerators environment [103, 104]. Therefore, a contactless technique based on carrier lifetime control within irradiated Si wafer fragments is presented. This technique enables fast measurements of a big amount of irradiated samples, collected from different irradiation areas, and direct evaluation of fluence based on strong relation of absolute carrier recombination lifetime values in high resistivity Si material those decrease linearly as a function of irradiation fluence Φ in wide range of fluence variations: $5\times10^{11}<\Phi<5\times10^{16}$ cm^{-2}.

The employed contactless technique is based on measurements and analysis of the MW-PCT, briefly described in Section 3.2.5. Radiation defects induced by large fluxes of ionizing radiation comprise a set of deep centres those act as carrier traps. Depending on types and activation parameters of the aforementioned radiation defects, the deep traps associated to these defects play different role in redistribution of excess carrier flows and on electrical characteristics of materials, acting either as carrier trapping or recombination centres. In low and moderately irradiated material, a big variety of extended and point defects of various species appears. Then, excess carrier decay exhibits a complicated behaviour and photoconductivity relaxation transients are non-exponential, containing several components dependent on carrier density, temperature, background illumination and other external factors. Variations of excess carrier decay transients measured on non-irradiated fragment of Si wafer are illustrated in Fig. 7.1. The non-exponential, a two-componential transient (curve 1 in Fig. 7.1) is observed for the low level pulsed excitation regime, where an initial fast component is ascribed to recombination, while the second one indicates carrier trapping effect, which delays recombination. Such decay behaviour indicates that several traps compete and interact within redistribution of carrier decay flows. Carrier decay becomes single-exponential (transients 2-4 in Fig. 7.1), when steady-state broad-band additional bias illumination (BI) is applied. Then, recombination process prevails (curves 2-4), as trapping to shallower levels is suppressed due to their filling by BI. Actually, a linear dependence between recombination lifetime (τ_R) and hadrons irradiation fluence is obtained and serves as a basis for dosimetry by this MW-PCT technique.

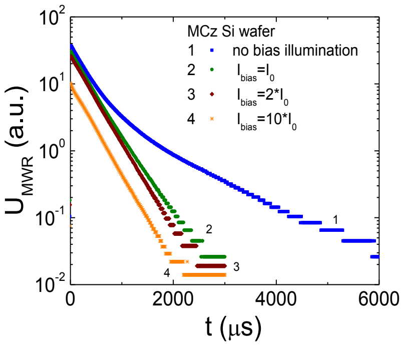

Fig. 7.1. MW-PC transients measured on non-irradiated n-Si wafer fragment at low level excitation regime without (1) and with (2-4) additional bias illumination.

7.2. Design of the instrument VUTEG-5-AIDA

To reach prevailing of recombination process and to cover wide range of fluences, the designed and fabricated instrument VUTEG-5-AIDA for dosimetry of collected fluence by MW-PCT technique (Fig. 7.2) contains a dark measurement cabinet, wherein a steady-state bias illumination source is installed. Sample under investigation, being placed within transparent plastic (polythene) bag, is mounted on positioning stage and brought into area of intersection of 500 ps pulsed IR (1062 nm) laser beam and of slit microwave antenna. The instrument also contains modules for adjustments of measurement regime by varying pulsed IR light intensity using neutral optical filters, by MW bridge varied coupling between sample and slit antenna and by changing intensity of bias illumination. Transients are recorded by a 1 GHz band digital oscilloscope and data processing is performed by personal computer. The possibility to average about 10^2 -10^3 transients enables us to significantly reduce an impact of noises. Recombination parameters are rapidly extracted by using software installed for data processing.

Fig. 7.2. Instrument VUTEG-5-AIDA for contactless dosimetry of irradiation fluence by MW-PCT technique.

7.3. Measurement regimes

To simplify mounting and to ensure a reliable positioning of the sample within measurement spot of spatial resolution of about 100 μm, to avoid surface contamination and to mark samples taken from different irradiation areas, methodology of measurements using VUTEG-5-AIDA instrument is designed by employing samples enveloped within plastic bags. These polythene bags, however, induce light scattering and some reduction of recorded MW-PCT signals. To verify characteristics of carrier recombination lifetime dependent on fluence, measured with and without plastic bag, the amplitude and decay rate parameters have been examined on several sets of Si wafer and device structures. These characteristics, measured by VUTEG-5-AIDA instrument, are illustrated in Fig. 7.3. It can be noticed in Fig. 7.3, that MW-PCT signal amplitude values are reduced for the sample-in-bag relatively to those obtained for bare sample. However, these amplitude characteristics are parallel, i.e. show the same dependence on fluence. Actually, a signal decreases within range of the highest fluences applied, due to approach of τ_R values to that of laser pulse duration and to a consequent decrease of the initially photo-excited excess carrier density. Carrier lifetime values as a function of irradiation fluence remain invariable irrespective of sample envelope.

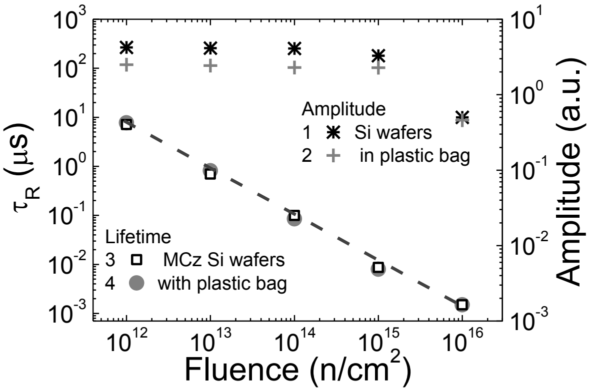

Fig. 7.3. Fluence dependent variations of MW-PCT signal amplitude (1, 2) and of carrier lifetime (3, 4) measured for bare (1, 3) and enveloped (2, 4) Si samples.

To increase precision of the dosimetry of collected fluence by MW-PCT technique and VUTEG-5-AIDA instrument, the calibration measurements using different materials, various structures and irradiations have been performed. These characteristics are illustrated in Fig. 7.4. It can be deduced that the linear decrease is obtained within τ_R-Φ characteristic for wafer fragments and diode structures made of Si, grown by various (FZ, MCZ, DOFZ) technologies, and irradiated with neutrons and protons of different energies. Additionally, absolute values of carrier recombination lifetime ascribed to definite hadron fluence nearly coincide, irrespective of hadrons energy in the range of penetrative particles. These observations can be explained by the rather homogenous damage of irradiated Si materials when displacement extended defects (directly formed by irradiation or resulted from defects aggregation reactions) prevail and act as the dominant recombination centres.

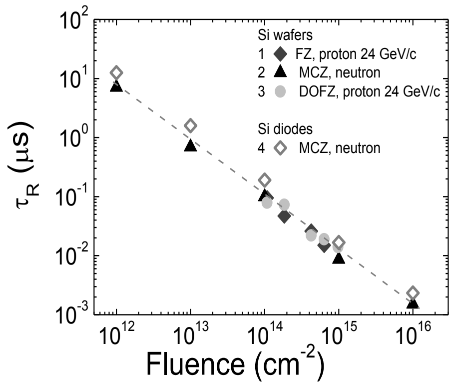

Fig. 7.4. Carrier lifetime variations as a function of irradiation fluence measured on Si wafer (1-3) and diode (4) samples made of different growth technology (FZ-1, MCZ - 2&4, DOFZ - 3) material and irradiated by neutrons (2&4) and protons (1&3).

7.4. Instrumentation for profiling of irradiation inhomogeneity

In order to increase precision, reliability and dynamic range of the measurement technique, VUTEG-5-AIDA instrument has been upgraded by adding temperature control and lateral mapping modules. A photograph of the instrument is shown in Fig. 7.5 left.

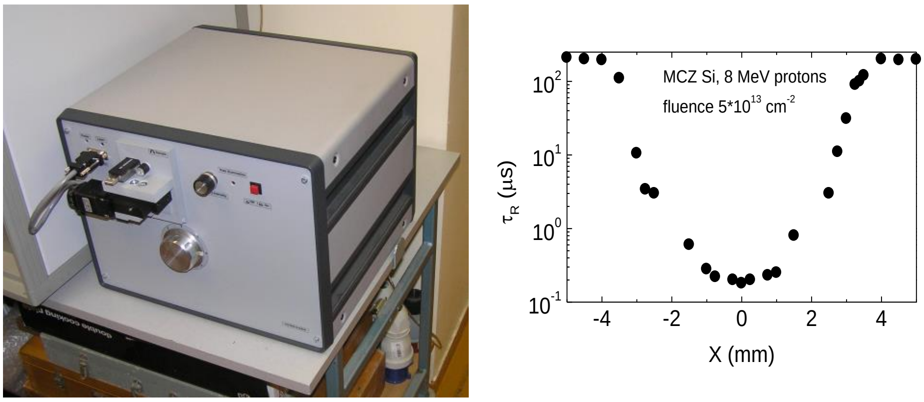

Fig. 7.5. On the left - the upgraded instrument VUTEG-5-AIDA-M. On the right - the distribution of the carrier recombination lifetime scanned across diameter within Si wafer fragment irradiated by 8 MeV proton beam with a spot diameter of 5 mm.

The upgraded instrument was tested at VU. The single dimensional scanner of the MW-PC transients with spatial resolution of about 20 µm has been fabricated in order to examine carrier lifetime lateral distribution. The instrument has been tested using Si wafer fragment irradiated by 8 MeV proton beam with a spot diameter of 5 mm. The mapped profile of the carrier recombination lifetime single-dimensional distribution is illustrated in Fig. 7.5b, where rather sharp proton beam contour is reproduced.

7.5. Software for measurement control and data processing

Software for measurement control and data processing based on LabVIEW platform was created including requirements specific for various regimes applied, for the calibration precision and for parameter extraction. The hierarchic window system was chosen for manipulation with instrument VUTEG-5-AIDA. An illustration of the main window for control interface is illustrated in Fig. 7.6.

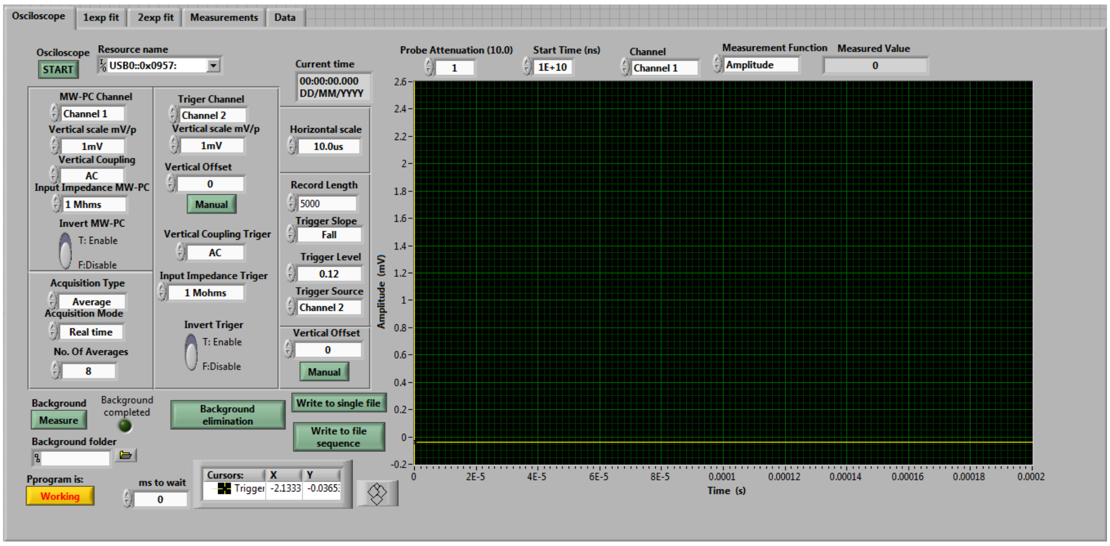

Resource name: USB0::0x0957:
Current time: 00:00:00.000 DD/MM/YYYY
MW-PC Channel: Channel 1
Vertical scale mV/p: 1mV
Vertical Coupling: AC
Input Impedance MW-PC: 1 Mhms
Invert MW-PC: T: Enable F:Disable
Acquisition Type: Average
Acquisition Mode: Real time
No. Of Averages: 8
Triger Channel: Channel 2
Vertical scale mV/p: 1mV
Vertical Offset: 0
Vertical Coupling Triger: AC
Input Impedance Triger: 1 Mohms
Invert Triger: T: Enable F:Disable
Horizontal scale: 10.0us
Record Length: 5000
Trigger Slope: Fall
Trigger Level: 0.12
Trigger Source: Channel 2
Vertical Offset: 0
Background folder:
Pprogram is: Working
ms to wait: 0
Cursors: Trigger X -2.1333 Y -0.0365
Probe Attenuation (10.0): 1
Start Time (ns): 1E+10
Channel: Channel 1
Measurement Function: Amplitude
Measured Value: 0

Fig. 7.6. VUTEG-5-Aida control interface main window.

There, five main tabs are presented: 1. “Oscilloscope” – where the manipulation with the main control tools for oscilloscope and a module for background signal elimination are presented. 2. “1exp fit” – this is an instrument for the single exponential fit of the registered transients, exploited when bulk recombination prevails. 3. “2exp fit”. This is a program for analysis and parameter extraction by using two-exponential fitting of the recorded transients. This software function is applied for data processing and parameter extraction in the annealed samples, when carrier trapping effect is important. Also, this operation is necessary if surface recombination velocity can be efficient, e.g. for non-irradiated non-passivated samples. To discriminate the prevailing processes, the additional bias illumination source is then manipulated. 4. “Measurements” – it is a command window to manipulate the oscilloscope and VUTEG-5-AIDA operational instruments for automatic measurement procedures. 5. “Data” – this is also a command window addressed to manipulate the data storage and graphic representation procedures.

Summary of the chapter

[A2, A10, P3, P12]

The VUTEG-5-AIDA dosimeter for monitoring of the large fluence irradiations within facilities of hadron accelerators and spallators has been designed and fabricated. This instrument has been installed at CERN and approved for the monitoring of the accelerator environments and particle beams. This instrument contains two different sample compartments, one of which is devoted for the rapid monitoring of the accelerator environments by using Si wafer fragment samples enveloped in plastic bags. Another compartment contains step motor driven scan instruments together with temperature/humidity control sensors is addressed to more precise examination of as-irradiated detectors and particle beams.

Conclusions

1. Passivation of surfaces of the Si strip detectors with slim edges is rather reproducible and efficient if passivating layer contains a steady-state built-in charge of proper polarity,- it is obtained better for p-Si (ALD alumina) than n-Si (PECVD nitride). Nevertheless, a lot of trapping centres exist at the interface within passivating layer.
2. The impact of surface recombination in the irradiated samples is negligible, when bulk density of the irradiation introduced defects considerably reduces carrier recombination lifetime relative to that determined by surface recombination velocity.
3. The close to a linear (using the double-logarithm scale) relation between the hadron irradiation fluence Φ and the excess carrier lifetime τ exists in large resistivity Si material when hadron irradiations produce extended radiation defects of varied density, proportional to the hadron fluence. This dependence is held independently of large resistivity Si growth technology and hadron type if recombination through extended radiation defects dominates. The small shift of the absolute values of carrier recombination lifetime within this linear τ-Φ characteristic can be taken into account by calibration measurements. Point radiation defects lead to carrier trapping effect and appearance of two-exponential photoresponse decay transient.
4. Spectroscopy of deep levels in Si attributed to point radiation defects unveiled several photo-ionization spectrum steps that have been resolved and identified, - namely, step E_{Mo1}=0.41 eV can be ascribed to direct photo-activation of filled single-charged di-vacancy levels; spectral step at $E_{Mo2}=E_V+E_M$=0.77 eV is associated with photoexcitation of electrons from valence band to primary emptied $V_2^{-/0}$ levels. Photo-ionization spectra confirmed the prevailing of the $V_2^{-/0}$ traps in 10^{12} n/cm^2 fluence irradiated diodes, in agreement with DLTS spectra recorded for the same diode. These traps mainly act as carrier trapping centres with rather long de-trapping time.
5. The photoluminescence photo-quenching effect has been revealed and ascribed to the microcrystals within polycrystalline CdS material. The PL-PQ

effect implies a complicated interplay of defects in redistribution of the photo-pulse excited carriers. The confocal microscopy images of CdS polycrystalline layers for different type samples enabled us to conclude that the most homogeneous CdS layer is obtained for the II-type samples, deposited at 260 C for 75 min. While, in III-type samples deposited at 260 C for 80 min, the PL spectra show that G-PL within microcrystals prevails the traps ascribed R-PL.

6. The transients of carrier decay can be well described by using a stretched exponent approximation, with different fractional index α values for separated types of CdS structures. The obtained values of α=0.16-0.20 hint on dominance of the anomalous character of excess carrier transport within a disordered structure of CdS polycrystals investigated. It has been inferred that samples of the II-type and the III-type are structurally similar and characterized by a fractal factor of $f\cong0.14$, and that samples of the I–type show a distinguishably disordered structure characterized by the fractal factor $f\cong0.17$.

7. The correlative analysis of the polycrystalline CdS parameters using the microwave probed photoconductivity, the time resolved luminescence spectroscopy and the in situ changes in the simultaneously measured luminescence spectra during 1.6 MeV proton beam irradiation enabled us to evaluate the following parameters: the efficiency of the carrier pair generation $\kappa_P=2\times10^7$ cm^{-3} per 1.6 MeV proton, the introduction rate of radiation defects $K_P\cong0.9$ cm^{-1} and the probable quantity of the collected charge per unit length of a sensor as $\kappa_P A_P=60$ μm^{-1}p^{-1}. A suitable range of the resolvable changes of scintillation signals in the range of proton fluences $\Phi<10^{15}$ cm^{-2} has been determined for CdS polycrystalline layers.

8. Comparison of the luminescence spectra induced by a proton beam and by a laser pulse in MOCVD grown GaN layers, enabled us to evaluate the efficiency of excess carrier generation by $\kappa_P=\langle n_P\rangle/N_P\cong1.3\times10^7$ cm^{-3} per 1.6 MeV proton and carrier pair generation within layer depth by $\kappa_P A_{pr}=40$ μm^{-1}p^{-1}. These parameters indicate that GaN layers can be an efficient material for detection of protons by combining both the electrical measurements, using

a proper thickness of detector layer with $\kappa_P A_{pr}$=40 μm^{-1}p^{-1} to reach the resolvable charge collection signal, and scintillation detection, using rather fast photo-sensors, capable to integrate the PI-YG-L signals with $\kappa_P \cong 10^7$ cm^{-3}p^{-1}. However, it has been obtained that the inevitable degradation of the material appears for proton irradiation fluences above 10^{14} cm^{-2} with radiation defect introduction rate $K_P \cong 0.6$ cm^{-1}. The calibrated reduction of the intensity of PI-L in the range of green-yellow luminescence can also be exploited for dosimetry of the hadron irradiations in rather wide range of fluences.

9. The difference in a carrier pair generation mechanism inherent for light and for a proton beam has been revealed in CdS and GaN layers. This observation has been explained by differences in the momentum conservation conditions inherent for the carrier generation by photons and protons. The possible mechanism of excess carrier excitation by proton beam could be a carrier generation process through the very fast annihilation of the primary vacancy–interstitial type radiation defects.
10. The VUTEG-5-AIDA dosimeter for monitoring of the large fluence irradiations within facilities of hadron accelerators and spallators has been designed and fabricated. This instrument has been installed at CERN and approved for the monitoring of the accelerator environments and particle beams.
11. The VUTEG-5-AIDA dosimeter enables rapid monitoring of the accelerator environments by using Si wafer fragment samples enveloped in plastic bags and precise examination of as-irradiated detectors and particle beams, which is implemented by lateral scans of carrier recombination lifetimes and by analysis of the amplitude and lifetime of the carrier trapping component within microwave probed photoconductivity transients.

References

[1] cern.ch/rd50 accessed on September 15, 2014.

[2] cern.ch/rd48 ROSE accessed on September 25, 2014.

[3] *ELEXSYS Userís Manual*, Bruker BioSpin Corporation, 2001.

[4] G. Lutz, *Semiconductor Radiation Detectors*, Springer, 1999.

[5] H. Spieler, *Semiconductor detector systems*, Oxford University Press, 2005.

[6] S. N. Ahmed, *Physics and Engineering of Radiation Detection,* Academic Press, Elsevier, 2007.

[7] C. Baldock, Y. De Deene, S. Doran, G. Ibbott, A. Jirasek, M. Lepage, K. B. McAuley, M. Oldham and L. J. Schreiner, *Topical Review: Polymer gel dosimetry,* Phys Med Biol. 2010 Feb 11, **55**(5): R1–R63.

[8] P.B. Moon, *Artificial Radioactivity*, Cambridge Univ. Press, 1949.

[9] A. Abragam and B. Bleany, *Electron paramagnetic resonance of transition ions,* Oxford: ClearendonPress, p. 911, 1970.

[10] International Commission on Radiation Units and Measurements. *Dosimetry Systems for Use in Radiation Processing.* Bethesda: 2008. (ICRU Report 80).

[11] D. F. Regulla and U. Deffner, *Dosimetry by ESR Spectroscopy of Alanine,* Int. J. Appl. Radiat. Isot., Vol. **33**, pp. 1101-1114, 1982.

[12] G. Lindstroem, *Radiation Damage in Silicon Detectors*, Nucl. Instr. Meth. A, **512**, 30, 2003.

[13] A. Chilingarov, H. Feick, E. Fretwurst, G. Lindstrom, S. Roe and T. Schultz, Nucl. Instr. and Meth. A **360** (1995) 1.

[14] E. Gaubas, T. Čeponis and J. Vaitkus, *Impact of generation current on the evaluation of the depletion width in heavily irradiated Si detectors*, J. Appl. Phys. **110** (2011) 033719.

[15] G. Bertolini, A. Coche, *Semiconductor Detectors*, Elsevier Science, 1968.

[16] S. Deme, *Semiconductor Detectors for Nuclear Radiation Measurement*, Wiley-Interscience, 1971.

[17] E. Fortunato et al., *Large Area Position Sensitive Detector Based on Amorphous Silicon Technology*, Mat. Res. Soc. Symp. Proceedings, **297**, 1993.

[18] G. F. Knoll, *Radiation Detection and Measurement*, Wiley, 2000.

[19] J. M. Taylor, *Semiconductor Particle Detectors*, Butterworths, 1963.

[20] W.R.T. Ten Kate, *The Silicon Microstrip Detector*, Technische Universiteit Delft, 1987.

[21] L. Rossi, et al., *Pixel detectors, from fundamentals to applications. Particle acceleration and detection*, ed. Springer, 2006.

[22] D.V. Lang, J. Appl. Phys. **45** (1974) 3023.

[23] D. K. Schroder, *Semiconductor Material and Device Characterization*, Wiley, New York, 1998.

[24] Y. Murakami, et. Al., J. Appl. Phys. **75** (1994) 3548.

[25] M. J. Cohen, *Semiconductor Photodetectors,* Society of Photo Optical, 2005.

[26] P. N. J. Dennis, *Photodetectors,* Springer, 1986.

[27] S. I. Parker et al., IEEE Transactions on Nuclear Sciencs NS-53 (2006) 1676.

[28] M. Bomben et al., Nuclear Instruments and Methods A **712** (2013) 41.

[29] M. Schbfthaler, R. Brendel, G. Langguth and J. H. Werner, *High-Quality Surface Passivation by Corona-Charged Oxides for Semiconductor Surface Characterization*, Photovoltaic Specialists Conference, 1994, 24th IEEE, Vol. **2**, pp. 1509-1512.

[30] M. M. Mandoc, M. L. C. Adams, G. Dingemans, N. M. Terlinden, M. C. M. van de Sanden, W. M. M. Kessels, *Corona Charging and Optical Second-Harmonic Generation Studies of the Field-Effect Passivation of c-Si by* Al_2O_3 *Films*, 36th IEEE PVSC, 2010.

[31] M. Christophersen et al., Nuclear Instruments and Methods A **699** (2013) 14.

[32] M. Christophersen, V. Fadeyev, S. Ely, B. F. Phlips, H. F.-W. Sadrozinski, Solid-State Electronics **81** (2013) 8.

[33] M. Christophersen, V.Fadeyev, B. F. Phlips, H. F.-W. Sadrozinski, *Scribing–cleaving passivation for high energy physics silicon sensors*, Proceedings of Science, Vertex 2012 (2013) 20.

[34] V. Fadeyev, S. Ely, Z. Galloway et al., Nuclear Instruments and Methods A **765** (2014) 59.

[35] R. Blachnik and A. Muller, Thermochim. Acta **361**, 31 (2000).

[36] Z. Nan, X. Y. Wang and Z. Zhao, J. Cryst. Growth **295**, 92 (2006).

[37] K. Okamoto, S. Kawai, Japan J. Appl. Phys. **12** (1973) 1130.

[38] G. She, X. Zhang, W. Shi, Y. Cai, N. Wang, P. Liu and D. Chen, Cryst. Growth Des. **8**, 1789 (2008).

[39] V. M. Garcia, P. K. Nair and M. T. S. Nair, J. Cryst. Growth **203**, 113 (1999).

[40] I. Grozdanov, M. J. Najdoski, Solid State Chem. **114** (1995) 469.

[41] A. Setkus, A. Galdikas, A. Mironas, I. Simkiene, I. Ancutiene, V. Janickis, S. Kaciulis, G. Mattongo, G. M. Ingo, Thin Solid Films **391** (2001) 275.

[42] N. Banno, T. Sakamoto, T. Hasegawa, K. Terabe, M. Aono, Japan J. Appl. Phys. **45** (2006) 3666.

[43] K. L. Chopra and S. R. Das, *Thin Film Solar Cells*, Plenum, New York, 1983.

[44] E. Bertran, J.L. Marenza, J. Esteve, J.M. Codina, J. Phys. D: Appl. Phys. 17 (1984) 1679.

[45] T. Yamamoto, K. Tanaka, E. Kubota and K. Osakada, *Deposition of copper sulfide on the surface of poly(ethylene terephthalate) and poly(vinyl alcohol) films in aqueous solution to give electrically conductive films*, Chemistry of Materials, vol. **5**, no. 9, pp. 1352-1357, 1993.

[46] A. Goldenblum, G. Popovici, E. Elena, A. Oprea, C. Nae, Thin Solid Films 141 (1986) 215.

[47] E. Aperathitis, C. G. Scott, J. Phys. Condens. Matter 1 (1989) SB269.

[48] E. Vanhoecke, M. Burgelman, L. Anaf, Thin Solid Films 144 (1986) 223.

[49] L. Soriano, M. Leon and F. Arjona, *On the photoconductivity of copper sulphide polycrystalline thin films*, Solar Energy Materials, vol. **12**, issue 2, pp. 149-155, 1985.

[50] M. Kundu, T. Hasegawa, K. Terabe, K. Yamamoto and M. Aono, *Structural studies of copper sulfide films: effect of ambient atmosphere*, Science and Technology of Advanced Materials, vol. **9**, no. 3, 035011, 2008.

[51] T. S. Te Velde, Energy Conv. 15 (1975) 111.

[52] A. Goldenblum, A. Oprea, J. Phys. D: Appl. Phys. 27 (1994) 582.

[53] E. Gaubas, T. Čeponis, V. Kalendra, J. Kusakovskij, A. Uleckas, *Barrier evaluation by linearly increasing voltage technique applied to Si solar cells and irradiated pin diodes,* ISRN Mater. Sc. **2012**, ID543790.

[54] E. Gaubas, T. Ceponis, S. Sakalauskas, A. Uleckas, A. Velicka, Lith. J. Phys. 51 (2011) 227.

[55] E. Gaubas, T. Čeponis, J. V. Vaitkus *Pulsed capacitance technique for evaluation of barrier structures*, LAMBERT Academic Publishing, Saarbrucken-Berlin, 2013, ISBN: 978-3-659-50518-8.

[56] P. Blood, J. W. Orton, *The electrical characterization of semiconductors: Majority carriers and electron states*, Academic Press: London, UK, 1992.

[57] V. Kalendra, D. Bajarūnas, E. Gaubas, *Comparative study of the photo-ionization and of DLTS characteristics in the hadrons irradiated Si detectors*. In Proceedings of Radiation interaction with material and its use in technologies-2012, Technologija, Kaunas, 2012.

[58] G. Lucovsky, *On the photoionization of deep impurity centers in semiconductors,* Solid State Commun. 1965, **3**, 299-302.

[59] E. Gaubas, A. Uleckas, R. Grigonis, V. Sirutkaitis, J. Vanhellemont, *Microwave probed photoconductivity spectroscopy of deep levels in Ni doped Ge*, Appl. Phys. Lett. 2008, *92*, 222102.

[60] A. G. Aberle, S. Glunz, W. Warta, J. Appl. Phys. **71**, 442 (1992).

[61] T. Oteradian, Solid-State Electron. **36**, 153 (1993).

[62] R. Smith, *Semiconductors*, Second Edition, Cambridge University Press, 1978.

[63] E. Gaubas, J. Vaitkus, E. Simoen, C. Claeys and J. Vanhellemont, *Excess carrier cross-sectional profiling technique for determination of the surface recombination velocity*, Materials Science in Semiconductor Processing, vol. **4**, issues 1-3, pp. 125-131, 2001.

[64] Presentations of E. Gaubas, J. Vaitkus at CERN rd39 and rd50 workshops 2007-2009, http://www.cern.ch/rd50

[65] E. Gaubas, A. Uleckas, J. Vaitkus, J. Raisanen and P. Tikkanen, *Instrumentation for the in situ control of carrier recombination characteristics during irradiation by protons*, Review of Scientific Instruments **81**, 053303, 2010.

[66] E. Gaubas, J. Vanhellemont, *A simple technique for the separation of bulk and surface recombination parameters in silicon,* J. Appl. Phys., **80**(11), pp.6293-6297, (1996).

[67] E. Gaubas, *Transient absorption techniques for investigation of recombination properties in semiconductor materials*. Lith. Journ. Phys. vol. **43** (2003) 145-165.

[68] E. Gaubas, K. Grigoras, I. Simkiene, *Velocity of surface recombination in silicon after various surface passivation technological procedures,* Lith. Journ. Phys. 37(6), pp. 544-550, 1997.

[69] E. Gaubas, J. Vanhellemont, *Comparative study of carrier lifetime variations with doping in Si and Ge,* Journal of The Electrochemical Society, Volume **154**, Number 3, (2007), pp. H231-H238.

[70] E. Gaubas, *Recombination processes and light - induced gradiential phenomena in silicon and III-V group compounds,* Habilitation Dissertation, 2002, Vilnius.

[71] E. Gaubas, T. Čeponis, A. Uleckas, J. Vaitkus, *Anneal dependent variations of recombination and generation lifetime in neutron irradiated MCZ Si,* Nuclear Instruments and Methods in Physics Research A, vol. **612**, (2010), pp. 563-565.

[72] *F. Hönniger, E. Fretwurst, G. Lindström, G. Kramberger, I. Pintilie, R. Röder,* DLTS measurements of radiation induced defects in epitaxial and MCz silicon detectors, Nucl. Instrum. Meth. A ***583*** *(2007) 104.*

[73] I. Pintilie, C. Tivarus, L. Pintilie, M. Moll, E. Fretwurst, G. Lindstroem, *Thermally stimulated current method applied to highly irradiated silicon diodes, Nucl. Instrum. Meth. A* **476** (2002) 652.

[74] V. Kalendra, V. Kažukauskas, N. Vainorius, J. Vaitkus, *Influence of irradiation by neutrons on the properties of* p^+*–n–*n^+ *Si radiation detectors, Physica B: Condensed Matter* **404** (2009) 4664.

[75] E. Gaubas, A.UIeckas and J. Vaitkus, *Spectroscopy of neutron irradiation induced deep levels in silicon by microwave probed photoconductivity transients, Nucl. Instrum. Meth. A* 607 (2009) 92.

[76] E. Gaubas, T. Čeponis, S. Sakalauskas, A. Uleckas and A. Velička, *Fluence dependent variations of barrier charging and generation currents in neutron and proton irradiated Si particle detectors, Lith. Journ. Phys.* **51** (2011) 230.

[77] E. Gaubas, T. Ceponis, A. Uleckas and R. Grigonis, *Room temperature spectroscopy of deep levels in junction structures using barrier capacitance charging current transients,* 2012 *JINST* **7** P01003.

[78] E. Gaubas, I. Brytavskyi, T. Čeponis, J. Kusakovskij and G. Tamulaitis, *Barrier capacitance characteristics of* $CdS–Cu_2S$ *junction structures,* Thin Solid Films, vol. 531, pp. 131-136, 2013.

[79] Semitrap DLS-82E user manual, Semilab, 1982.

[80] F. Poulin, A. W. Brinkman, J. Woods, *Electron and hole traps in the* Cu_xS*-CdS heterojunction,* J. Cryst. Growth 1982, **59**, 240-245.

[81] P. Besomi, B. Wessels, *Deep level defects in polycrystalline cadmium sulphide,* J. Appl. Phys. 1980, **51**, 4305-4310.

[82] M. Hussein, G. Lleti, G. Sagnes, G. Bastide, M. Rouzeyre, *Deep level transient spectroscopy of electron traps and sensitizing centers in undoped CdS single crystals,* J. Appl. Phys. 1981, **52**, 261-269.

[83] D. Verity, D. Shaw, F. J. Bryant, C. G. Scott, *DLTS investigation of electron traps in as-grown and Cd-fired CdS*, Phys. Stat. Sol. (a) 1983, **78**, 267-275.

[84] M. Claybourn, A. W. Brinkman, G. J. Russel, J. Woods, *Electron traps in single-crystal CdS*, Philos. Mag. B 1987, **56**, 385-395.

[85] W. Zhao, L. Bing, Zh. Xu, X. Jing, H. Zheng, L. Cai, F. Liang-Huan, Zh. Jia-Gui, *Deep level transient spectroscopy investigation of deep levels in CdS/CdTe thin film solar cells with Te:Cu back contact*, China Phys. B 2010, **19**, 027303.

[86] L. E. Lashkarev, A. V. Liubchenko, M. K. Sheinkman, *Non-equilibrium processes in photo-conductors (in Russian)*; Naukova Dumka: Kiev, 1981.

[87] L. Pavesi, *Influence of dispersive exciton motion on the recombination dynamics in porous silicon*, Journal of Applied Physics, vol. **80**, issue 1, pp. 216-225, 1996.

[88] E. Gaubas, S. Juršėnas, S. Miasojedovas, J. Vaitkus and A. Žukauskas, *Carrier and defect dynamics in photoexcited semi-insulating epitaxial GaN layers*, Journal of Applied Physics, vol. **96**, no. 8, pp. 4326-4333, 2004.

[89] S. Havlin and D. Ben-Avraham, *Diffusion in disordered media*, Advances in Physics, vol. **51**, no. 1, pp. 187-292, 2002.

[90] J. C. Phillips, *Stretched exponential relaxation in molecular and electronic glasses*, Reports on Progress in Physics, vol. **59**, no. 9, pp. 1133-1207, 1996.

[91] J. C. Phillips, *Slow dynamics in glasses: A comparison between theory and experiment*, Physical Review B, vol. **73**, issue 10, 104206, 2006.

[92] J. C. Phillips, *Microscopic aspects of Stretched Exponential Relaxation (SER) in homogeneous molecular and network glasses and polymers*, Journal of Non-Crystalline Solids, vol. **357**, issues 22-23, pp. 3853-3865, 2011.

[93] S. Jursenas, G. Kurilcik, A. Zukauskas, Phys. Rev. B **54**, 16706 (1996).

[94] B. Ray, *II-VI Compounds*, Pergamon, Oxford, 1969.

[95] J. F. Ziegler, J. P. Biersack and M. D. Ziegler, *SRIM - The Stopping and Range of Ions in Matter*, SRIM Co., Chester, 2008.

[96] W.-D. Park, Trans. Electr. Electron. Mater. **13**, 196 (2012).

[97] Chapter *Cadmium sulfide (CdS) diffusion of carriers and ions* in book: *II-VI and I-VII Compounds; Semimagnetic Compounds*, edited by O. Madelung, U. Rössler and M. Schulz (Springer Berlin Heidelberg, Berlin, 1999) p. 1. DOI:10.1007/10681719_564

[98] M. Moll, Nucl. Instrum. Meth. Phys. Res. A **565**, 202 (2006).

[99] S. Nakamura, T. Mukai and M. Senoh, Appl. Phys. Lett. **64,** 1687 (1994).

[100] R. Schwarz, R. Cabeça, E. Morgado, M. Niehus, O. Ambacher, C. P. Marques and E. Alves, Diamond & Related Materials **16,** 1437 (2007).

[101] M. Pophristic, F. H. Long, C. Tran, I. T. Ferguson and R. F. Karlicek, J. Appl. Phys. **86,** 1114 (1999).

[102] S. Nagarajan, Y. S. Lee, M. Senthil Kumar, O. H. Cha, C.-H. Hong and E.-K. Suh, J. Phys.D: Appl. Phys. **41,** 012001 **(**2008).

[103] P. J. Sellin and J. Vaitkus, Nucl. Instr. Meth. A **557,** 479 (2006).

[104] E. Gaubas, S. Juršėnas, R. Tomašiūnas, J. Vaitkus, A. Žukauskas, A. Blue, M. Rahman and K. M. Smith, Nucl. Instr. Meth. Phys.Res. A **546,** 247 (2005).

[105] E. Gaubas, K. Kazlauskas, R. Tomašiunas, J. Vaitkus and A. Žukauskas, Appl. Phys. Lett. **84**, 5258 (2004).

[106] J. M. DeLucca, J. Appl. Phys. **88,** 2593 (2000).

[107] V. V. Ursaki, I. M. Tiginyanu, P. C. Ricci, A. Anedda, S. Hubbard and D. Pavlidis, J. Appl. Phys. **94,** 3875 (2003).

[108] E. Arslan, S. Butun, S. B. Lisesivdin, M. Kasap, S. Ozcelic and E. Ozbay, J. Appl. Phys. **103,** 103701 (2004).

[109] D. Li, X. Dong, J. Huang, X. Liu, Zh. Xu, X. Wang, Z. Zhang and Zh. Wang, J. Cryst. Growth **249,** 72 (2003).

[110] M. A. Reshchikov and H. Morkoç, J. Appl. Phys. **97,** 061301 (2005).

[111] M. Birkholz, *Thin film analysis by X-ray scattering*, Wiley-VCH Verlag GmbH&Co. KgaA, Weinheim, 2006.

[112] H. Heinke, V. Kirchner, S. Einfeldt and D. Hommel, Appl. Phys. Lett. **77**, 2145 (2000).

[113] K. L. Luke and L. J. Cheng, J. Appl. Phys. **61 ,** 2282 (1987).

[114] M. Gallart, T. Taliercio, A. Alemu, P. Lefebvre, B. Gil, J. AlleÁgre, H. Mathieu and S. Nakamura, Phys. Stat. Sol. (b) **216**, 365 (1999).

[115] S. F. Chichibu, H. Marchand, M. S. Minsky, S. Keller, P. T. Fini, J. P. Ibbetson, S. B. Fleischer, J. S. Speck, J. E. Bowers, E. Hu, U. K. Mishra and S. P. DenBaars, Appl. Phys. Lett. **74**, 1460 (1999).

[116] G. Pozina, N. V. Edwards, J. P. Bergman, B. Monemar, M. D. Bremser and R. F. Davis, Phys. Stat. Sol. (a) **183**, 151 (2001).

[117] S. Juršėnas, S. Miasojedovas, G. Kurilčik, A. Žukauskas and P. R. Hageman, Phys. Stat. Sol. (a) **201**, 199 (2004).

[118] B. Monemar, P. P. Paskov, J. P. Bergman and G. Pozina, A. A. Toropov, T. V. Shubina and T. Malinauskas, Phys. Rev. B **82**, 235202 (2010).

[119] P. P. Paskova, R. Schifano, T. Paskova, T. Malinauskas, J. P. Bergman, B. Monemar, S. Figge and D. Hommel, Physica B **376–377**, 473 (2006).

[120] B. Monemar, P. P. Paskov, J. P. Bergman, T. Paskova, C. Hemmingsson, T. Malinauskas, K. Jarasiunas, P. Gibart and B. Beaumont, Physica B **376–377**, 482 (2006).

[121] A. Y. Palyakov, A. S. Usikov, B. Theys, N. B. Smirnov, A. V. Govorkov, F. Jomard, N. M. Shmidt and W. V. Lundin, Solid-state Electron. **44**, 1971 (2000).

[122] P. Pittet, G.-N. Lu, J.-M. Galvan, J.-M. Bluet, I. Anas, J.-Y. Giraud and J. Balosso, Optical Materials **31**, 1421 (2009).

[123] http://www.srim.org accessed on December 5, 2014.

[124] S. C. Jain, M. Willander, J. Narayan and R. Van Overstraeten, J. Appl. Phys. **87**, 965 (2000).

[125] S. Nakamura, S. F. Chichibu, *Introduction to Nitride Semiconductor Blue Lasers and Light Emitting Diodes*, Taylor & Francis, London, 2000.

[126] D. V. Lang, L. C. Kimerling and S. Y. Leung, J. Appl. Phys. **47**, 3587 (1976).

[127] L. Lü, Y. Hao, X. F. Zheng, J. C. Zhang, S. R. Xu, Z. Y. Lin, S. Ai and F. N. Meng, Sci. China Tech. Sci. **55**, 2432 (2012).
[128] A. D. Kurtz, S. A. Kulin and B. L. Averbach, Phys. Rev. **101**, 1285 (1956).
[129] M. A. Moram and M. E. Vickers, Rep. Prog. Phys. **72**, 036502 (2009).
[130] N. M. Shmidt, V. V. Sirotkin, A. A. Sitnikova, O. A. Soltanovich, R. V. Zolotareva and E. B. Yakimov, Phys. Stat. Sol. (c) **2**, 1797 (2005).
[131] E. B. Yakimov, J. Phys.: Condens. Matter **14**, 13069 (2002).
[132] K. Yamamoto, H. Ishikawa, T. Egawa, T. Jimbo and M. Umeno, J. Cryst. Growth, **189/190**, 575 (1998).
[133] V. V. Emtsev, V. Yu. Davydov, V. V. Kozlovskii, G. A. Oganesyan, D. S. Poloskin, A. N. Smirnov, E. A. Tropp and Yu. G. Morozov, Physica B: Cond. Mat. **401-402**, 315 (2007).
[134] F. D. Auret, S. A. Goodman, F. K. Koschnick, J.-M. Spaeth, B. Beaumont and P. Gibart, Appl. Phys. Lett. **74**, 407 (1999).
[135] A. I. Titov and S. O. Kucheyev, J. Appl. Phys. **92**, 5740 (2002).
[136] S. J. Pearton, C. R. Abernathy, R. G. Wilson, J. M. Zavada, C. Y. Song, M. G. Weinstein, M. Stavola, J. Han and R. J. Shul, Nucl. Instrum. Meth. Phys. Res. B **147**, 171 (1999).
[137] S. O. Kucheyev, J. S. Williams and C. Jagadish, Vacuum **73**, 93 (2004).

List of abbreviations

ALD – atomic layer deposition (formation technology)

BELIV – barrier evaluation by linearly increasing voltage (pulsed technique)

CERN –European Centre of Nuclear Research

CZ – Czochralski (growth technology)

CMI - confocal microscopy imaging

C-V – capacitance-voltage (measurement technique)

CVD – chemical vapour deposition (growth technology)

ENR - electrically neutral region

EPR - electron paramagnetic resonance (type of spectroscopy)

FZ – float zone (growth and purification technology)

DLTS – Deep Level Transient Spectroscopy

DOFZ –oxygen doped float zone (growth and doping technology)

GIXRD - grazing incidence X-ray diffractometry

Kerma - kinetic energy released per unit mass

LED – light emitting diode (WL-LED white light LED)

MCZ- Czochralski with applied magnetic field (growth technology)

MOCVD – metal-organic chemical vapour deposition (growth technology)

MW-PC (T) –microwave probed photo-conductivity (MW-PC (T) transient)

NIEL - non-ionizing energy loss processes

PECVD –plasma enhanced chemical vapour deposition

PIS – photo-ionization spectroscopy

PL- photo-luminescence

SER – stretched exponential relaxation (model and process of relaxation)

S/HL-LHC – super/hyper luminous large hadron collider (at CERN)

SCP -method scribe–cleave–passivate (formation of sensor slim edge)

TDD - threading dislocation density

TR-L – time resolved luminescence

TSC - thermally stimulated currents (spectroscopy technique)

UV- ultra violate

XRD -X-ray diffractometry

YG-PI-L -yellow-green proton induced luminescence (the same PI-YG-L)

Y-yellow; **B-**blue; **IR**–infra-red; **RIR-** red –infrared (luminescence colour)